UC Berkeley
UC Berkeley Electronic Theses and Dissertations

Title
Nano-Optoelectronic Integration on Silicon

Permalink
https://escholarship.org/uc/item/1q00d26k

Author
Chen, Roger

Publication Date
2012

Peer reviewed|Thesis/dissertation

eScholarship.org Powered by the California Digital Library
University of California

Nano-Optoelectronic Integration on Silicon

by

Roger Chen

A dissertation submitted in partial satisfaction of the

requirements for the degree of

Doctor of Philosophy

in

Engineering – Electrical Engineering and Computer Sciences

in the

Graduate Division

of the

University of California, Berkeley

Committee in charge:

Professor Connie Chang-Hasnain, Chair
Professor Ming C. Wu
Professor Xiang Zhang
Professor Eli Yablonovitch

Fall 2012

Nano-Optoelectronic Integration on Silicon

Copyright © 2012

by

Roger Chen

Abstract

Nano-Optoelectronic Integration on Silicon

by

Roger Chen

Doctor of Philosophy in Engineering – Electrical Engineering and Computer Sciences

University of California, Berkeley

Professor Connie Chang-Hasnain, Chair

Modern silicon technology offers unprecedented spatial and temporal control of electrons with high levels of integrated complexity. Integrating nanophotonic functionality onto silicon should then allow us to extend this level of control to photons. Resulting nano-optoelectronic systems will inevitably create new functionality, which not only enables next-generation technologies like optical interconnects, but also gives rise to yet unforeseen applications.

Directly growing III-V nanomaterials on silicon provides an advantageous pathway towards optoelectronic integration. Conventional wisdom often breaks at the nanoscale, and traditional integration challenges like lattice mismatch are circumvented. In particular, III-V nanoneedles and nanopillars with attractive optical properties grow on silicon under conditions that are compatible with the process constraints of CMOS technology.

This dissertation will present a variety of nano-optoelectronic devices developed using the nanoneedle and nanopillar platform. Nanolasers are demonstrated under optical pumping, and progress towards electrical injection is shown. Under reverse bias, nanopillars enable avalanche photodiodes featuring gain-bandwidth products in excess of 100 GHz. Nanopillar devices also exhibit clear photovoltaic effects and even support nonlinear optical generation. The breadth of functionality shown suggests that a powerful marriage between photons and electrons on silicon is well within reach.

To my parents

Table of Contents

Table of Contents ii

List of Figures iv

List of Tables xvi

Acknowledgements xvii

Chapter 1 Introduction 1

Chapter 2 Nano-optoelectronic integration 4

2.1 Approaches to optoelectronic integration 4

2.1.1 III-V on silicon 4

2.1.2 Group IV photonics 6

2.2 Nanowires 7

2.3 Nanoneedles and nanopillars 8

2.3.1 Growth 8

2.3.2 Photoluminescence 12

2.3.3 Spatially-resolved and polarized emission 14

2.3.4 Time-resolved photoluminescence 19

Chapter 3 Nanophotonic phenomena 23

3.1 Subwavelength light using metal 23

3.2 Helically-propagating modes 24

Chapter 4 Nanolasers on silicon 32

4.1 Introduction 32

4.2 Nanolaser growth 33

4.3 Laser oscillation on silicon 35

4.4 Helically-propagating modes 39

4.5 Wavelength control of laser emission 43

4.6 Waveguide coupling 44

4.7 Laser modeling 45

4.7.1 Gain modeling 45

4.7.2 Rate equation analysis 49

4.7.3 Gain switching 51
4.8 Future challenges 53
Chapter 5 Towards electrically-driven nanolasers on silicon 56
5.1 Device fabrication and electrical testing 56
5.2 Electroluminescence experiments 62
5.3 Electrically-driven amplified spontaneous emission 66
5.4 Quantum well-based devices 70
Chapter 6 Avalanche photodiodes on silicon 73
6.1 Device fabrication 73
6.2 Device testing 77
6.3 Avalanche gain 79
6.4 High-speed operation 82
6.5 Summary and outlook 86
Chapter 7 Photovoltaic effects 87
7.1 Nanotechnology and solar cells 87
7.2 Photovoltaic effects in III-V nanopillars on silicon 87
Chapter 8 Nonlinear optics 91
8.1 Second-harmonic generation 91
8.1.1 Observations of frequency doubling 92
8.1.2 Polarization dependence 94
8.1.3 Second-harmonic Fresnel coefficients 96
8.2 Resonance enhancement of nonlinear processes 98
Chapter 9 Conclusion 102
References 104

List of Figures

Figure 1.1 Electron-photon interaction. Electrons and photons have a long history of interaction. Perhaps electrons can provide the conduit through which complex control of photons can be obtained. 1

Figure 2.1 The various means of integrating III-V onto silicon. a, Monolithic growth **b,** direct wafer bonding **c,** indirect wafer bonding. 5

Figure 2.2 Lattice mismatch constraints. a, Lattice mismatch causes dislocations in epitaxial III-V layers on Si, but **b,** nanowires with small footprints can accommodate it. This figure was adapted from reference [44]. 7

Figure 2.3. SEM images of nanoneedles and nanopillars on silicon. a, An SEM image adapted from ref. [53] shows a GaAs nanoneedle grown on silicon. The nanoneedle tapers down to an atomically sharp tip as highlighted by the inset. **b,** Nanopillars can also grow with truncated tops as shown in this SEM image adapted from ref. [55]. In this case, growth occurred on a polysilicon substrate, showcasing the diversity of the nanoneedle/nanopillar growth mechanism. 9

Figure 2.4. Core-shell growth of nanoneedles. Core-shell growth of nanoneedles enables growth of large III-V single crystals on lattice-mismatched Si by maintaining a minimum interface with the substrate. 10

Figure 2.5. Growth evolution of nanopillar heterostructures. An InGaAs nanoneedle structure first nucleates on silicon. Under the proper conditions, vertical growth is halted such that the nanoneedle is transformed into a nanopillar structure. The InGaAs nanopillar core is then cladded by a GaAs shell to complete the heterostructure, which provides in-situ surface passivation. 11

Figure 2.6. Photoluminescence setup. 12

Figure 2.7. Photoluminescence spectra for various nanoneedle materials. GaAs-based nanoneedle materials can form quantum wells and ternary compounds. PL spectra are shown for a variety of nanoneedle structures including bulk GaAs and AlGaAs as well as GaAs/AlGaAs and InGaAs/GaAs quantum well. 13

Figure 2.8. Indium composition variation for emission wavelength control. Nanopillar spontaneous emission spectra at different indium compositions show the wavelength tunability of nanopillar emission. In this work, the composition is varied from 12% to 20%. The ability to control the emission wavelength offers an important optoelectronic device design parameter. 14

Figure 2.9. Schematic and SEM image of a quantum well nanoneedle a, Schematic showing the structure of core-shell InGaAs/GaAs quantum well

nanoneedles. **b,** 30° tilt-view false-color SEM image of an as-grown core-shell nanoneedle. The inset shows a top-view image that reveals the six facets of the hexagonal nanoneedle. 15

Figure 2.10. Experimental setup for simultaneously measuring orthogonal polarizations while spatially mapping photoluminescence. 16

Figure 2.11. Polarized photoluminescence from nanoneedles. μ-PL from **a,** a single core-shell nanoneedle (NN) and **b,** a single bulk GaAs nanoneedle polarized ⊥c-axis (red) and ∥c-axis (black). Both types of nanoneedles exhibit anisotropy with preference for emission polarized ⊥c-axis, indicating macroscopic spontaneous polarization effects due to the wurtzite crystal structure. 17

Figure 2.12 Polarized photoluminescence from nanopillars. Polarized emission from nanopillars is plotted in **a,** x-y and **b,** polar forms. Photoluminescence is strongly polarized perpendicular to nanopillars' longitudinal c-axis. This polarization arises from the material itself and not from optical antenna effects. 17

Figure 2.13 Contours of spatially resolved PL from a single core-shell nanoneedle. Emission polarizations are **a,** ∥c-axis and **b,** ⊥c-axis. **c,** Contour of the PL peak wavelength. The broken triangles (purple) show the nanoneedle orientation. ... 18

Figure 2.14 Spectral properties of polarized emission. a, Spectral image showing nonuniform nanoneedle PL emission along the white dashed line in Fig. 2.13b. Core-shell quantum well emission intensifies and redshifts towards the tip of the nanoneedle while emission at the base is primarily from the GaAs core and cladding. Polarization dependent PL spectra are shown for positions **b,** near the nanoneedle tip and **c,** by the nanoneedle base as marked by points 1 and 2 in part **a** and Fig. 2.13**b**. 19

Figure 2.15. Experimental setup for time-correlated single photon counting. 20

Figure 2.16. Time-resolved photoluminescence decay. The photoluminescence shown in **a,** was also **b,** resolved in time to reveal insight into nanopillar recombination dynamics. The interesting shape of the decay curve is explained in the main body of text. 21

Figure 2.17. Carrier concentration dependence of carrier lifetime. For some materials, carrier lifetime can be either nonradiative-dominated or radiative-dominated depending on the carrier concentration. 22

Figure 3.1 Plasmonic localization of electric fields. Collective electron oscillations in metal can generate optical electric fields that are tightly confined to metal surfaces. 23

Figure 3.2 Ray model visualization of helically-propagating modes. Helically-propagating modes can strongly reflect from low-index contrast interfaces to tightly confine light within nanopillars integrated on silicon. 25

Figure 3.3 Helically-propagating mode field patterns. a-d, Transverse field patterns for various azimuthal modes and polarizations. **e-f,** Axial field patterns along the length of nanopillars also show standing waves. 26

Figure 3.4 FDTD-simulated spectrum of TM_{6n} nanopillar modes. For each azimuthal mode number, several axial mode orders exist. The n=1-7 axial mode resonances are shown here for the TM_{6n} mode. The axial mode numbers associated with each peak are labeled. This sort of grouping of axial resonances exists for all azimuthal mode orders. 27

Figure 3.5 Resonance dependence on nanopillar radius. Helical modes of all orders and polarizations depend heavily of nanopillar radius as might be expected for whispering gallery-like modes. 28

Figure 3.6 Cavity resonance versus nanopillar height. Simulated dependence of TM_{6n} resonances on nanopillar height. Notably, there is little dependence for the fundamental Fabry-Perot degeneracy (TM_{61}) since it behaves like a whispering gallery mode. Higher order modes show higher dependence on the axial dimension as they become more like Fabry-Perot modes in nature. 29

Figure 3.7 Mode cutoff of helical modes in nanopillars grown slanted on silicon. Helically-propagating modes are supported by nanopillars despite an oblique interface between the InGaAs nanopillar and silicon. As shown, the field profile is not affected despite this oblique junction. The mode is strongly confined within the nanopillar even for slanted nanopillars on silicon. The oblique interface still introduces a mode cutoff that strongly reflects light just like in the case of nanopillars grown vertically from substrates. 29

Figure 3.8 Imaging helically-propagating modes. Helically-propagating modes have been imaged from various nanopillars grown at oblique angles on polysilicon. Corresponding SEM images and optical micrographs are shown. 30

Figure 3.9 Polarization of helical modes. Measurements suggest that both TE and TM modes are excited experimentally, but TE modes are perhaps more dominant 31

Figure 4.1 InGaAs/GaAs heterostructure nanopillar lasers monolithically grown on silicon. a, A schematic is shown for a nanopillar laser monolithically integrated onto silicon, illustrating its InGaAs core and GaAs shell. The higher band gap GaAs shell protects carriers from nonradiative surface recombination, which is critical for room temperature lasing. The inset shows a top-view schematic. **b,** An SEM image reveals the well-faceted geometry of the nanopillar optical cavity. This resonator structure forms naturally during growth, allowing lasers to be directly

grown on silicon without additional processing. Nanopillar dimensions scale with growth time, enabling growth of effectively bulk high-quality III-V material on silicon. No critical dimensions have been observed for this novel lattice-mismatched growth mechanism. **c,** A top-view SEM image highlights the nanopillar's hexagonal wurtzite crystal structure. This hexagonal symmetry results in whispering gallery-like effects that we discuss later. 34

Figure 4.2 On-chip nanopillar laser oscillation. a, Room temperature nanopillar emission is shown below (blue) and above (red) threshold. The spectrum below threshold has been magnified 200x for visibility. The inset shows the L-L curve and linewidth clamping of the laser, revealing a threshold at ~93 μJ/cm^2. **b,** Camera images of nanopillar emission below threshold show only a spot of spontaneous emission. **c,** Upon lasing, strong speckle patterns appear. Speckle results from the high degree of coherent emission and is a classic signature of laser oscillation. 35

Figure 4.3 The role an outer GaAs shell. Thicker GaAs shells serve to confine carriers away from nonradiative states on the surfaces of nanopillars. 36

Figure 4.4 L-I curve of a nanopillar laser. The L-L curve of a nanopillar laser operating at 4 K with a low threshold of ~22 μJ/cm^2 is analyzed to extract estimated values of Q~206 and β~0.01. The inset shows spectra of the nanopillar laser both below (blue, magnified 20x) and above (red) threshold. The laser peak clearly dominates above threshold, achieving a 17 dB background suppression ratio. 37

Figure 4.5 Time-resolved photoluminescence of nanopillar lasers. a, Below threshold, a relatively slow decay exists. Above threshold, radiative recombination accelerates greatly as stimulated emission processes take over. The 49 ps time constant shown is limited by the resolution of the system. The long tail in the above-threshold curve arises from the natural response of the photodetector used. **b,** The spectra corresponding to the decay curves in **a** with arrows marking the center wavelengths detected. 38

Figure 4.6 Subwavelength laser spectra. a, Emission spectra below (blue) and above (red) threshold from a nanopillar that is subwavelength in volume and on all sides. The below threshold curve has been multiplied by 50 for visibility. **b,** The power-dependent evolution of lasing spectra is shown for the same laser on a log scale as a reference. Measurements for this device were performed at T=4 K. This set of spectra corresponds to the laser shown in Fig. 4.7e. 39

Figure 4.7 Helically-propagating modes for optical feedback of on-chip nanolasers. a, A schematic depicts how a helical ray path enables reflection from a low-index contrast interface due to glancing angle incidence, lending physical insight into the mechanism behind strong optical confinement in on-chip nanopillars. **b,** An FDTD-simulated field profile shows a hexagonal WG-like mode pattern (TM_{6n}) in the transverse plane, which arises from strong azimuthal components of helical modes. Such modes have net propagation along the nanopillar axis and build axial

standing wave patterns. The first-order standing wave is shown in **c** while a higher-order one is shown in **d**. **e,** Strong light localization provided by helical modes enables nanolasers that are subwavelength on all sides. An SEM image shows such a subwavelength device. **f-h,** Experimental images of nanopillar emission show standing wave patterns along the nanopillar axes, corroborating helical mode propagation. SEM photos of the nanopillars imaged are shown. 40

Figure 4.8 Effects of nanopillar sidewall taper on optical modes. Vertical field profiles are shown of a nanopillar on Si with 5° taper for **a,** TM_{61}, **b,** TM_{62} and **c,** TM_{63} modes. The profiles here are plotted on log scale for clarity. The transverse field profiles are identical to that in Fig. 4.7b. Sidewall tapering results in increased light leakage, which decreases the quality factors of helical resonances to ~170-300. The smaller radius on the upper part of the pillar also introduces a mode cut-off such that helical modes are confined towards the base of tapered nanopillars. Furthermore, tapering blueshifts helical resonances. **d,** Experimental results confirm the aforementioned effects of tapering on helical modes. 42

Figure 4.9 Cavity resonance versus nanopillar radius. Dependence on nanopillar radius of TE_{41}, TE_{51}, TM_{57} and TM_{63} resonances is shown. Ranges of resonances are displayed to account for the effects of sidewall taper (0-5°) on cavity wavelengths. Gray diamonds denote experimental lasing wavelengths of nanopillars of various radii. The experimental data is well within the range of modes simulated, suggesting that TE_{4n}, TE_{5n}, TM_{5n} and TM_{6n} modes provide optical feedback for our lasers. Ultimately, the laser wavelength range is between 890-930 nm, limited by the InGaAs gain region. 43

Figure 4.10 Wavelength control of nanopillar lasers by composition variation. Nanopillar lasers can be implemented over a broad range of wavelengths by properly tuning indium composition and nanopillar dimensions. Nanopillars are grown to target dimensions designed to achieve resonances at specified wavelengths. Indium composition of the InGaAs core is concurrently adjusted so that nanopillar gain and emission spectrally match the resonant wavelength for laser oscillation. The spectra shown are offset for clarity. In this study, a change in indium composition from approximately 12-20% provides a 50 nm control in the output laser wavelength............ 44

Figure 4.11 Side-view far-field pattern for TM_{61} mode of a nanopillar resonator on silicon. The profile shows the dominance of radial emission for nanopillar lasers, much akin to whispering gallery modes in microdisks and ring resonators. The upwards (blue) and downwards (green) radiation patterns have been magnified 2000x and 10x, respectively. 45

Figure 4.12 Fitting spontaneous emission spectrum. The experimental spontaneous emission spectrum (red circles) below theshold is fitted by the theoretical spectrum (grey line) calculated using τin=40 fs. Only every 30th point of the experimental spectrum is plotted to more clearly show the fit. The fit

overestimates the emission tails, which is a well-known problem with Lorentzian lineshape broadening methods. 47

Figure 4.13 Gain spectra at T=4 K. Calculated gain spectra for different carrier densities based on spontaneous emission data and material parameters from literature. The gain is plotted versus energy from the band edge. The gain has been calculated for a temperature of 4 K since most experiments are performed at cryogenic temperatures in a cryostat 48

Figure 4.14 Gain model. Logarithmic material gain model, which we use with traditional rate equations for further laser analysis. 48

Figure 4.15 Rate equation fitting. a, Different Q's primarily affect threshold values and thus horizontally shift the L-L curve. Able to correlate carrier densities to experimental pump levels, we can therefore estimate Q from rate equation fitting. **b,** Varying β meanwhile allows fitting of the pronunciation of the "knee" in the L-L curve around threshold. 51

Figure 4.16 Modeled nanopillar transient response under ultrafast pulse excitation. a, Femtosecond pulses generate carrier densities far above threshold, which quickly drop below threshold upon the nanopillar emitting a laser pulse as shown in **b**. Spontaneous emission takes over below threshold, though it is much weaker than the pulse of stimulated light. **c,** The femtosecond excitation pulse plotted as a reference. 52

Figure 4.17 Gain switching effects on spontaneous emission. a, The modeled transient photon density response shows a spike of nanopillar laser emission followed by spontaneous recombination after the carrier density drops below threshold as shown in **b**. Higher pump fluences notably cause the initial drop in carrier density to be more drastic, reducing the spontaneous emission above threshold as seen experimentally in **c** and **d**. Here, spontaneous emission reduction rather than clamping can be seen due to gain switching effects. 53

Figure 4.18 Nanolasers grown on MOSFETs. a, Spectral evolution of laser oscillation from nanolasers grown on MOSFETs with the L-L curve in the inset. **b,** SEM image of a nanolaser grown directly on a MOSFET gate. 55

Figure 5.1 Schematics of nanopillar device active material and metal-optic cavity. a, A schematic of the active material used for electrically-controlled nanopillar devices shows its p-i-n double heterojunction. **b,** A metal-optic cavity can clad nanopillars by careful conformal deposition of oxide and metal films. 57

Figure 5.2 Process flow for e-beam lithography of nanopillars. Additional details of the process can be found in the main body of text. 58

Figure 5.3 Leakage paths in nanopillar diodes on silicon. a, The poor junctions in the polycrystalline layers surrounding single crystal nanopillars give rise to shunt paths for current leakage as shown. **b,** This can be modeled by the simple circuit shown. Maximizing R_{shunt} can help maximize current through the useful diode path...... 59

Figure 5.4 Fabrication process flow for electrically-injected nanopillar light-emitting diodes and lasers. Additional details are discussed in the main body of text .. 60

Figure 5.5 Nanopillars at various stages of the laser structure fabrication process. a, Alignment markers allow the relative positions of nanopillars to be defined. A nanopillar is coated by **b,** a SiO_2 etch mask before **c,** undergoing dry etching and **d,** wet etching. **e,** A second oxide deposition isolates p- and n-contacts while also forming the dielectric portion of the metal-optic cavity. **f,** Rotating the sample at an angle during e-beam evaporation coats the nanopillar with metal and thereby completes fabrication of the electrically-injected metal-optic laser structure. 61

Figure 5.6 Electrical characteristics of nanopillar devices. a, Dozens of I-V curves show clear and consistent diode behavior, testifying to the robustness of the fabrication process flow. **b,** Devices can exhibit diode ideality factors of nearly 2, a nearly ideal value for GaAs-based diodes. 62

Figure 5.7 Electrical connections inside a cryostat used for electroluminescence. A device sample is first mounted on a leadless chip carrier, which then mounts onto the cold finger of the cryostat. Devices are wire bonded to the chip carrier, and a plug electrically connects the chip carrier to an external pinout using the cryostat's built-in feedthrough pins.. 63

Figure 5.8 Continuous wave LED electroluminescence at 4 K. Nanopillar LEDs emit bright electroluminescence under continuous wave operation. Under stronger bias levels, emission redshifts and decreases due to thermal effects. 64

Figure 5.9 Continuous wave LED electroluminescence at room temperature. a, At room temperature, electroluminescence from single nanopillar LEDs is bright and can withstand high continuous wave current densities. **b,** The L-I curve shows a slightly nonlinear increase in light output before the device emission rolls over due to heat. 65

Figure 5.10 Room temperature images of electroluminescence. The device in **a** emits light bright enough to be imaged with a CCD camera as shown in **b**. The light would be visible to the naked eye if it were at visible wavelengths. 65

Figure 5.11 Pulsed LED electroluminescence at 4 K. Strong band filling and emission results from injection of high-voltage pulses. It is unknown how much current couples into devices due to a large impedance mismatch. 66

Figure 5.12 Amplified spontaneous emission from nanopillar devices. a, An SEM image of an electrically-driven single nanopillar laser structure. **b,** These structures exhibit amplified spontaneous emission under pulsed pumping at 4 K, though lasing has not yet been achieved. Prominent band filling effects can be observed when comparing the ASE spectrum to the spontaneous emission one...................................... 67

Figure 5.13 Pump dependence of amplified spontaneous emission. a, ASE featuring many prominent peaks explodes rapidly under higher pumping levels, which can be even more clearly seen from the L-I curve of **b**. 68

Figure 5.14 Temperature dependence of amplified spontaneous emission spectra. a, Electrically-injected emission spectra show several ASE peaks (A-D) superimposed upon a broad spontaneous emission background (X). Temperature dependence studies were done to verify the origin of these peaks. **b,** Spontaneous emission (X) shifts more quickly with temperature than the purported cavity peaks (A-D), which shift in parallel with one another. 69

Figure 5.15 Fitting temperature dependence of amplified spontaneous emission. The observed temperature dependences can be explained by the different temperature dependences of band gap and refractive index, which determine energy shifts of spontaneous emission and cavity resonances, respectively. We find that peak X follows the Varshni model for energy band gaps, while peaks A-D follow a typical GaAs thermo-optic coefficient of $dn/dT=2.67x10^{-4}$. We thereby confirm our attribution of observed spectral peaks to ASE. 69

Figure 5.16 High material gain under electrical injection. a, Experimental ASE curves are fitted by analytical formulae using the proper parameters. This analysis allows us to calculate many relevant metrics including quasi-Fermi level splitting and carrier concentration achieved under electrical injection. **b,** Based on our spectral fit, we can generate a gain spectrum for the measured device, showing that experimental gain >3,400 cm^{-1} can already be achieved. 70

Figure 5.17 Quantum well light-emitting diodes. Schematics of the as-grown quantum well structure and the quantum well LED are shown in **a** and **b**, respectively. Meanwhile, **c** and **d** show SEM images of the as-grown sample and fabricated device. 71

Figure 5.18 Room temperature electroluminescence from quantum well light-emitting diodes. a, PL and EL spectra of the QW LED at room temperature shows. **b,** EL is highly linear versus pump current. 72

Figure 6.1 Nanopillar avalanche photodiodes. a, A schematic of a nanopillar avalanche photodiode is shown. **b,** An SEM image of nanopillar avalanche photodiode.. 74

Figure 6.2 Fabrication process flow for nanopillar avalanche photodiodes. Additional details are discussed in the main body of text. 76

Figure 6.3 Improving diode performance. Etching away the p-shell reduces current leakage more than the poly-layer etch does. From the I-V plots shown, the poly-layer etch clearly results in a larger shunt path. Also, the p-shell etch method more reliably results in devices with ideality factors of 2. 77

Figure 6.4 Nanopillar avalanche photodiode testing. a, An optical micrograph shows typical device contact and pad configuration. Two top-side test pads were used for high-speed testing. Note the n-pad was not yet metallized here. The inset shows an SEM image of a completed device. **b,** Various etching, lithography, and deposition techniques were used to fabricate nanopillar avalanche photodiodes. SiO_2 acts as electrical insulation between the p- and n-type layers. 77

Figure 6.5 Experimental apparatus for testing high-speed avalanche photodiodes. 78

Figure 6.6 Light coupling into nanopillar avalanche photodiodes. a, The illumination beam spot was measured to help estimate light coupling into APDs. **b,** A schematic illustrates how metal inhibits light from coupling into APDs. 79

Figure 6.7 Avalanche gain. a. IV curves from devices with and without incident illumination show clear photocurrent (and also photovoltaic) effects owing to the high-quality radial p-i-n junctions grown. Dark current is low at 1.2 pA and 0.45 nA at 0 V and -1 V, respectively. **b,** Strong gain multiplication is observed with increasing reverse bias. At -4.4 V, a multiplication factor of 33 is reached. 80

Figure 6.8 Avalanche photodiode linearity. The linearity of nanopillar APDs supports that increase in photocurrent is not due to thermally activated diffusion or similar processes. 81

Figure 6.9 S_{21} measurements of nanopillar avalanche photodiodes. S_{21} measurements show that nanopillar APDs can indeed operate at high bandwidths. **a,** The device exhibiting a gain of 33 in Fig. 6.7 also shows a bandwidth of 3.1 GHz. That device thus features >100 GHz in gain-bandwidth product. **b,** Even faster devices have been measured as suggested by the 3.6 GHz response seen here................ 82

Figure 6.10 Avalanche photodiode impulse response. S_{21} bandwidths fall short of expected bandwidths based on device impulse responses because of the presence of a tail as shown. Future improvement in bandwidth will require understanding and eliminating this tail. 83

Figure 6.11 Limitations in avalanche photodiode speed. a, Rise times as fast as 33 ps have been measured, implying >10 GHz operation should be attainable. **b,** The 3

dB bandwidth for devices does not change for higher bias voltages. This is likely a consequence of the gain-bandwidth product being limited by a diffusion tail. 83

Figure 6.12 Avalanche photodiode rise times. a, While the S_{21} bandwidth does not change with bias, the rise time of the impulses response does. **b,** This implies that bandwidth does indeed depend on bias, but it is presently limited by the diffusion tail. The bandwidth values plotted are what is expected using equation (6.1). 84

Figure 6.13 Averaged large signal detection. Large-signal modulation of a 850 nm VCSEL can be clearly detected by nanopillar-based APDs. Here, on/off signals with periodicity <0.3 ns are observed. Averaging was used for this measurement. Light coupling and SNR must be improved in the future to demonstrate open eye diagrams. .. 85

Figure 6.14 Unaveraged large signal detection. Practicality requires unaveraged large signal detection, which we show here. For a first-generation device, nanopillar APDs demonstrate respectable performance with a SNR of 15 dB and *Q* of 2.8. The bit stream detected was '1100100' as labeled. 85

Figure 7.1 Using nanopillars as photovoltaic materials. Scanning electron microscope (SEM) images of nanopillars grown on **a,** (111) silicon and **b,** polycrystalline silicon. Nanopillar growth on lattice-mismatched substrates has proven to be a versatile technology, allowing III-V integration on different types of silicon, GaAs, and even sapphire substrates. **c,** A schematic of a nanopillar-based photovoltaic device. 88

Figure 7.2 Low ideality and dark current. Photovoltaic devices exhibit a nearly ideal ideality factor as low as 2.1 89

Figure 7.3 Promising photovoltaic effects observed in nanopillars on silicon. Solar energy generation can be clearly seen from IV curves under illumination at (i) 0 μW, (ii) 5 μW, (iii) 10 μW, (iv) 20 μW, (v) 40 μW, (vi) 50 μW and (vii) 100 μW. The fill factor remains fairly constant at 61% for all illumination intensities. 90

Figure 7.4 Photovoltaic performance under concentration. a, The open-circuit voltage, however, increases in a logarithmic fashion and approaches a respectable 0.8 V. The dashed black line is a fit using equation (7.1) for n=3.2, T=300, and V_{oc}=0.223 V. k, q, and X are the Boltzmann constant, electron charge, and concentration (unit 1 kW/m^2), respectively. **b,** The short-circuit current versus illumination follows a linear slope as expected. 90

Figure 8.1. GaAs nanoneedles for second harmonic generation. Scanning electron microscope images of a wurtzite GaAs nanoneedle **a,** from surface normal planar view and **b,** 30°-tilt view. The crystal c-axis lies along the longitudinal growth direction of the nanoneedle. The a-axis is in the transverse direction. **c,** Schematic detailing measurement conditions. The nanoneedle rests horizontally on a double-

side polished sapphire substrate. θ is the angle between the laser's polarization and the nanoneedle c-axis. 92

Figure 8.2 Experimental setup for characterizing second-harmonic generation. 93

Figure 8.3 Laser and SHG spectra. Both fundamental and second-harmonic fields are polarized along the nanoneedle's c-axis. The bandwidth of the SHG spectra represents the bandwidth of the 120 fs pulses at 806 nm used for excitation. Nonlinear optical coefficients are estimated for WZ-GaAs by comparing the intensity of SHG from a single nanoneedle to SHG from reference CdSe and CdS wafers. 94

Figure 8.4. Power dependence second-harmonic generation. The data plotted on a log-log scale fits a slope of 2 and thereby follows a quadratic power dependence, confirming the second-order nature of the emitted light. 94

Figure 8.5. Polarization dependence of second-harmonic generation. Blue circles and red diamonds show experimental excitation polarization dependence data for SHG polarized ‖c-axis and ⊥c-axis, respectively. Solid lines show the respective theoretical fits. Relative intensity scales are arbitrary. **a,** Fundamental field polarization dependence of second-harmonic generation polarized along a single nanoneedle's c-axis. $\chi^{(2)}_{ccc}$ and $\chi^{(2)}_{caa}$ contribute to this second-harmonic polarization. Maxima occur at 0°, 180°, and 360°, revealing that $\chi^{(2)}_{ccc}$ is the stronger tensor element. The ratio between the maximum and minimum second-harmonic intensity is typically about 20:1. **b,** Fundamental field polarization dependence of second-harmonic generation polarized along a single nanoneedle's a-axis. For second-harmonic light polarized transverse to the nanoneedle, the only nonzero tensor element is $\chi^{(2)}_{aca}$. Thus, maxima are expected at 45°, 135°, 225°, and 315° as shown by the experimental data. From these measurements, the ratios of the tensor elements are estimated to be $\chi^{(2)}_{ccc} : \chi^{(2)}_{aca} : \chi^{(2)}_{caa} \sim 4.4 : 2 : 1$. 96

Figure 8.6 Backward-generated SHG. A schematic illustrates the backward generation of second-harmonic light from an air-dielectric boundary. Such SHG must satisfy what amounts to second harmonic Fresnel coefficients. 97

Figure 8.7 Resonance-enhanced second-harmonic generation. Imaging SHG from single nanoneedles reveals local enhancement effects that are highly reminiscent of helically-propagating modes imaged in Section 3.2. It is likely that helically-propagating resonances enhance SHG in smaller nanoneedle structures by enhancing the first harmonic pump light. Enhancement from an **a,** n=2 and a **b,** n=3 mode are shown. 99

Figure 8.8 Two-photon photoluminescence from Au-coated nanoneedles. a, PL spectra show a broad two-photon photoluminescence signature. **b,** The TPPL has a quadratic power dependence as expected for second-order nonlinear effect. 100

Figure 8.9 Surface-enhanced Raman scattering from Rhodamine 6G molecules on a roughened gold film. Clear SERS signals are recorded from R6G molecules on roughened gold film. The SERS spectrum matches others reported in literature........... 101

Figure 9.1 Nano-optoelectronic integration with silicon electronics. A vision for the future 103

List of Tables

Table 4.1 Material parameters for gain modeling. 47

Table 4.2 Parameters for rate equation analysis. 50

Acknowledgements

First and foremost, I thank my dissertation committee members, Prof. Connie Chang-Hasnain, Prof. Ming C. Wu, Prof. Xiang Zhang, and Prof. Eli Yablonovitch. Each has greatly influenced my intellectual growth and development over these last few years. I especially want to thank my advisor, Prof. Connie Chang-Hasnain, for her support throughout my graduate school career. She not only gave me an opportunity to succeed, but always challenged me to be at my best. For that, I am forever grateful.

I made my journey over the last few years with a group of remarkable researchers. These individuals have taught me far more than any single textbook or class ever can. In particular, I owe much to Dr. Forrest Sedgwick, Dr. Erwin Lau, and Dr. Linus Chuang for the wisdom they shared as my elder statesmen. I thank Dr. Michael Moewe, Dr. Shanna Crankshaw, Dr. Chris Chase, Dr. Matthias Kuntz, and Dr. Devang Parekh for the guidance and training they granted me over the years. I also thank Vadim Karagodsky, who started, but woefully could not finish, graduate school with me in Prof. Chang-Hasnain's group. I would like to pay particular homage to my colleague Kar Wei (Billy) Ng. Without his "light bulbs" and his selflessness, I could never have achieved what I have achieved. At the same time, it has been my pleasure to work with Wilson Ko, Thai Tran, Fanglu Lu, Linda Li, April Sun, Frank Rao, and Dr. Stephon Ren. Our discussions catalyzed much of the progress made over recent years. Finally, I thank the rest of the optoelectronic group members and the entire EECS community at Berkeley. It has been a privilege to intellectually engage everyone over the years.

Additionally, my gratitude extends across the globe to my former collaborators in Wurzburg, Germany. I thank Prof. Dr. Alfred Forchel and Prof. Dr. Stephan Reitzenstein for hosting me during my three month exchange in their group. While short, my time in Germany was formative for me, both intellectually and personally. I also thank Christian Schneider for folding me into the culture and community in Wurzburg.

I could not have surmounted the challenges of a Ph.D. education without the friendship and support I accumulated both during and before my time at Berkeley. I made many friends in various graduate student offices, but I would like to particularly thank Amit Lakhani, Jeff Chou, James Ferrara, Owen Miller, Nikhil Kumar, Sapan Agarwal, Matteo Staffaroni, Alex Hegyi, Michael Eggleston, and Peter Matheu. Outside of graduate school, many have provided me the emotional support, comic relief, food and fantastic 'neatballs' that I relied on. While there are too many to list here, they certainly belong, and I thank them all.

I thank the Marvell Nanolab staff for their support and for putting up with me as I worked feverishly in their labs. I am sure that there were at least a few instances when I made a mess or error that they would help clean up. In particular, I thank Dr. Bill Founders, Kim ChanJoe Donnelly, Jay Morford, Sia Parsa, Evan Stateler, Brian McNeil, David Lo, Bob Hamilton, and Eric Chu.

For financially supporting me during my graduate studies, I thank the NDSEG Fellowship, MARCO IFC, and DARPA NACHOS.

Last but certainly not least, I must thank my family, which has shown tremendous patience, love, and support throughout my life. I especially thank my parents, who have sacrificed much for me. Though I do not always express myself, I feel utterly indebted to you. I also especially thank my grandparents, who raised and molded me as a young child. I thank my aunts, uncles, and cousins for always looking out for my best interests.

Chapter 1

Introduction

Discovery and utility often reside at the intersection between known objects. Children studying basic algebra learn that the solution for a system of equations exists at the equations' point of intersection. In competitive markets, pricing tends to shift towards equilibrium at the intersection between supply and demand. Semiconductor junctions meanwhile empower modern computing and information technology, and in medicine, interactions between body tissue and magnetic fields enable magnetic resonance imaging (MRI) [1], [2]. In some instances, overlap of normally unrelated disciplines can even create entirely new fields of research such as neuroscience.

This dissertation explores the intersection between photons and electrons. Human command of both elementary particles has had profound impact on society, but the ability to manipulate photons falls far short of our authority over electrons. While simple incandescent light still pervades everyday life [3], silicon technology can massively integrate precise spatial and temporal control of electrons on a single chip [4], [5]. Perhaps integrating nanophotonic functionality onto silicon will extend this level of control to photons. From the photoelectric effect to light-emitting diodes (LEDs) [6], [7], history has repeatedly shown that photons and electrons closely interact as illustrated in Fig. 1.1. If we can leverage the integrated complexity of nanoscale electronics to harness this interaction, then we can achieve integrated optoelectronic complexity far beyond what is possible today.

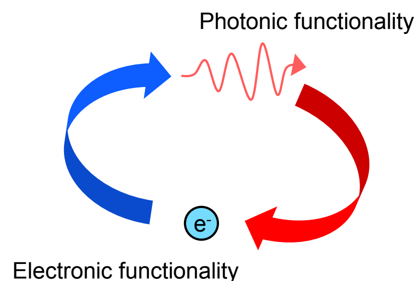

Figure 1.1 Electron-photon interaction. Electrons and photons have a long history of interaction. Perhaps electrons can provide the conduit through which complex control of photons can be obtained.

However, integrating photonic functionality onto silicon is no trivial task. For all of its wonders as an electronic material, silicon is quite limited in the photonic domain. Due to its indirect band gap, it emits light with exceedingly low efficiency, making it unsuitable for the critical optoelectronic function of generating photons. Exploring how to surmount this challenge is thus a major thrust of this dissertation, and Chapter 2 begins by discussing popular approaches towards this endeavor. Some researchers explore ways to integrate optically-bright III-V films onto silicon, while others attempt to engineer the indirect band gap of Group IV elements.

This thesis proposes a third approach – bottom-up integration of III-V nanomaterials. Specifically, we leverage growth of III-V nanoneedles and nanopillars to realize a multitude of nano-optoelectronic devices on silicon. Like traditional III-V compounds, nanoneedles and nanopillars exhibit exceptional optical properties. Unlike traditional III-V films, these nanomaterials overcome issues with lattice mismatch and are synthesized via a process that is compatible with complementary metal-oxide-semiconductor (CMOS) technology.

Manipulating light within nanostructures requires nuanced understanding of nanophotonic phenomena. Thus, Chapter 3 studies the behavior of light within wavelength-scale and subwavelength structures. Interestingly, nanoneedles and nanopillars support optical modes that can be effectively described as helically-propagating. By leveraging these modes to achieve strong optical feedback, we demonstrate that nanolasers can be directly grown on silicon in Chapter 4. True optoelectronic integration requires electrical control of photonic functions, so in Chapter 5, we summarize efforts towards electrically-driven nanolasers on silicon.

The ability to convert photons to electrons is just as important as the reverse process, and III-V nanomaterials can do this in bunches. Chapter 6 details the realization of III-V avalanche photodiodes on silicon with tiny footprints using single nanopillars. Without bias, these devices also exhibit a clear photovoltaic effect, which we briefly touch on in Chapter 7. Able to generate light, detect light, and convert light into electrical power, III-V nanopillars incorporate all primary optoelectronic functions onto a silicon substrate. While this alone is compelling, we demonstrate how III-V nanomaterials on silicon can even manipulate light in the frequency domain. Chapter 8 studies second-harmonic generation from nanoneedles and touches on their potential for enhancing other nonlinear processes. Coupling plasmonic effects with the atomically sharp tips of nanoneedles could greatly facilitate two-photon photoluminescence and surface-enhanced Raman scattering.

So what is the impact of all this? We began this dissertation by claiming that discovery and utility result when two forces like photons and electrons intersect. What new knowledge and functionality will we find? Idealistically, there are no bounds if we can truly control photons to our heart's content. Consider the history of electronics. Many of today's electronic technologies fall far beyond the realm of most people's imaginations from only a few decades ago. In a few more decades, what will we achieve with photonics? Will we be able to slow down and accelerate light [8], [9]? Will we entangle

photons on demand for covert communications [10], [11]? Light directly interacts with everything around us from biological processes to chemical reactions to energy generation. If we master light, what more doors, or intersections, can we find then? We thus reaffirm that there are no bounds, and even if there are, we should not think so.

But, to show that the future of nano-optoelectronics is more than just an idealistic dream, let us now briefly discuss some rather concrete applications emerging from the horizon. Optical interconnects are a prime example. As computing capacity continues to scale, data transport on and between microprocessor chips becomes increasingly difficult. This interconnect bottleneck severely threatens growth in the semiconductors industry, but perhaps optical interconnects will solve this challenge by offering low-energy, high-bandwidth density connections [12]–[14]. Meanwhile, LEDs are rapidly enabling new classes of lighting and displays [15], [16]. At the same time, researchers and new companies have begun exploring the possibility of using optoelectronics for retinal prosthesis [17]. Myriad other applications exist, and they all stand to benefit from optoelectronic integration, which this dissertation advocates can be done using III-V nanomaterials on silicon.

Chapter 2

Nano-optoelectronic integration

Given that optoelectronic integration on silicon is a major theme of this dissertation, it is dutiful to first summarize the major efforts that have gone towards this goal. Chapter 2 opens by discussing the different methods that have been explored for silicon-based optoelectronics. It then offers some background on III-V nanomaterials since they are the other major theme of this thesis. Finally, we introduce III-V nanoneedles and nanopillars on silicon, a specific class of nanomaterials developed only recently. Going forward, the nano-optoelectronic devices presented in this dissertation are by and large based on these nanomaterials.

2.1 Approaches to optoelectronic integration

The two main approaches towards optoelectronic integration on silicon (Si) have been integrating III-V photonic materials onto Si and using group IV elements like Si itself for optical functions. Both methods have witnessed some success, yet faced even greater challenge. Their challenges differ drastically, and it remains to be seen which, if either, method will ultimately become a solution.

2.1.1 III-V on silicon

The value proposition for combining III-V materials with silicon is clear. III-V materials have traditionally been the best material for active optoelectronic devices like lasers, while Si of course has been the foundation of electronics. It therefore seems sensible to merge both materials and simultaneously leverage the unique capabilities of each. However, this optimistic view neglects many realities. Si has become the backbone for modern electronics partly because of the investment that has gone towards it. As a consequence, proposing to integrate any foreign material with silicon requires that the foreign material be fully compatible with silicon processes. In particular, it must be compatible with modern complementary metal-oxide-semiconductor (CMOS) technology. Unfortunately, III-V compounds typically are not. It is instructive to review existing III-V on silicon integration approaches to understand why. Figure 2.1 summarizes the three

main approaches: (a) monolithic growth, (b) direct wafer bonding, and (c) indirect wafer bonding.

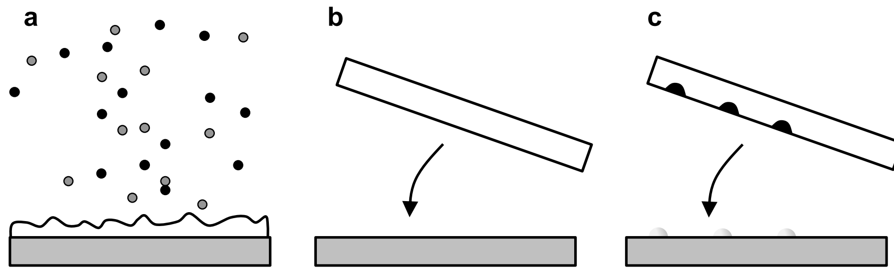

Figure 2.1 The various means of integrating III-V onto silicon. a, Monolithic growth **b,** direct wafer bonding **c,** indirect wafer bonding.

The most obvious means of merging III-V semiconductors with Si is directly growing III-V materials on Si substrates. While lasers have in fact been demonstrated in this manner [18], the large lattice mismatch between III-V and Si results in unacceptably poor III-V film quality and device performance [19]. Nanomaterials have meanwhile found some success in overcoming lattice mismatch limitations, suggesting that they may be key to integrating optoelectronics onto Si [20], [21]. However, growth temperatures for III-V systems are far higher than the thermal budget allows for silicon electronics [22]. Additionally, vapor-liquid-solid (VLS) growth commonly used for nanowires utilizes gold (Au) catalysts that are poisonous to modern CMOS devices. Clearly then, monolithic growth faces major challenges despite the reasonable logic behind it.

Another school of thought believes that a more viable integration approach would be directly bonding III-V and Si wafers per the schematic in Figure 2.1 [23]–[26]. In this case, issues related to both lattice mismatch and growth temperatures are largely mitigated. However, direct wafer fusion invariably requires pristine material and surface conditions [26], [27]. In other words, wafer scale bonding is tremendously difficult if CMOS electronics have already been fabricated because CMOS terrain is highly complex. At the same time, CMOS foundries do not tolerate foreign III-V materials so bonding III-V wafers with Si before electronics fabrication is also impractical. The alternative then is to bond smaller III-V die onto manufactured CMOS wafers. In this case, scalability presents a major challenge, and the complexity of CMOS terrain still makes it difficult even for small III-V chips to be bonded.

The last major method of integration is indirect wafer bonding. In this scenario, an intermediate layer consisting of metal, epoxy, solder balls or other material fills the voids between Si and III-V to hold them together [28]–[32]. A major benefit of this method is its ability to tolerate surface imperfections, but the added necessity of an interlayer introduces complexity and can be expensive. The patterning and alignment required greatly constrains fabrication process flows in an intolerable manner. Furthermore, the same challenge exists for wafer-level bonding onto CMOS terrain. Thus, scalability is again an issue for indirect bonding.

Clearly, making optoelectronic integration compatible with CMOS presents a daunting challenge with many obstacles. Should integration occur at the front-end-of-line (FEOL) or back-end-of-line (BEOL)? What temperatures are tolerable for integration processes? What materials are acceptable for integration? These dilemmas are difficult, and for that reason, some prefer to implement silicon optoelectronics by use traditional electronic materials like germanium (Ge) or Si itself. This will be the topic of the next section.

2.1.2 Group IV photonics

Silicon possesses many wonderful properties that make it an excellent medium for manipulating electrons and holes to create logic functions. If Si could control photons in a similar fashion, it truly would be the perfect optoelectronic material. This line of thinking has motivated many to pursue the implementation of optoelectronics on Si using Si for both photonics and electronics. Germanium (Ge), another group IV element, has also received similar attention because of its inherent compatibility with Si. While it certainly is not Si, it does not nearly face the integration challenges that a III-V material like gallium arsenide (GaAs) faces. In fact, Ge is more and more becoming part of conventional CMOS technology.

The indirect band gap of group IV elements has proven to be the biggest roadblock for purely Si-based optoelectronics. While Si and Ge are good absorbers, their indirect band gap makes them exceedingly poor light emitters [33]. Momentum conservation for radiative recombination is extremely difficult and only occurs on the rare occasion when sufficient phonon assistance is offered.

Still, creative engineering efforts have resulted in impressive improvements in group IV emission. For Si, nanostructures and texturing have been key to achieving optical gain [34]–[36]. Even silicon light-emitting diodes with over 1% efficiency have been fabricated [37]. However, further progress has been greatly limited since these milestone achievements, which subsequently compelled researchers to explore another group IV material in Ge. For Ge, the ability to engineer strain and doping has provided a powerful means of improving light emission [38]–[42]. Recently, even an electrically-injected Ge laser on silicon was demonstrated [39]. Despite all this progress, Ge-based lasers likely face a long road before they can offer sufficient performance for optical interconnects and other applications. Energy efficiency is a critical metric for lasers [14], [13], and it is difficult to imagine efficient radiation from semiconductors without dominantly direct band gaps. Nonetheless, new developments may continue to surprise, and optoelectronics based purely group IV semiconductors would certainly a "holy grail."

In many respects, the debate between choosing III-V compounds versus group IV materials for optoelectronics can be summarized by the following question: Is it easier to engineer through major integration obstacles or fight the physics of indirect band gaps? This dissertation takes the position that the former offers a more viable solution for optoelectronic integration on silicon. It is difficult to change silicon infrastructure unless

the economics behind it deems it necessary to adopt III-V materials, but it is likely more difficult to defy the physical laws that govern the radiative properties of silicon and germanium. Certainly though, it is possible that both III-V and group IV materials will be needed. After all, group IV photodiodes already represent the state of the art for integrated photodetectors on Si.

2.2 Nanowires

This dissertation advocates for III-V nanomaterials as a vehicle for building optoelectronics on silicon. It is therefore appropriate to briefly review nanomaterials, particularly nanowires. III-V nanowires have often been touted for their ability to overcome lattice mismatch and grow on a variety of substrates including silicon [43]. As shown in Fig. 2.2, epitaxy on lattice-mismatched substrates often results in severe dislocations, while the smaller footprints of nanowires can somewhat accommodate strain and allow dislocation-free heterogeneous material integration.

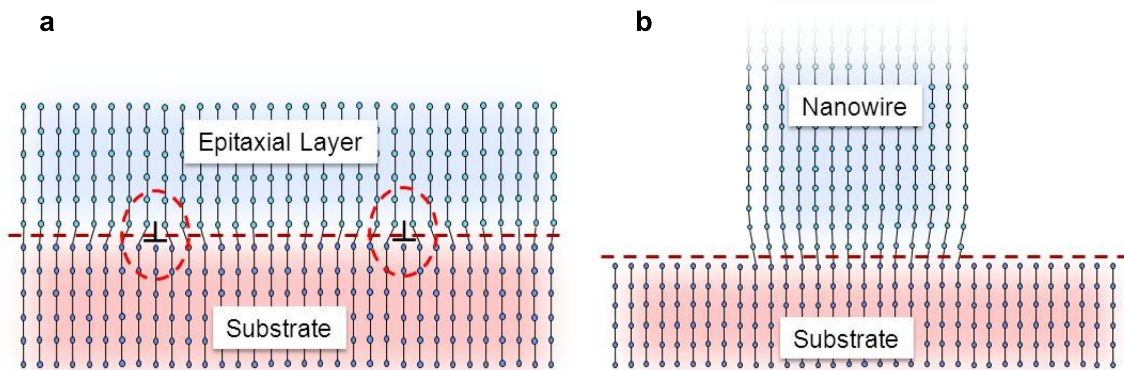

Figure 2.2 Lattice mismatch constraints. a, Lattice mismatch causes dislocations in epitaxial III-V layers on Si, but **b,** nanowires with small footprints can accommodate it. This figure was adapted from reference [44].

Even so, nanowires still face a critical diameter beyond which they cannot usually grow with high quality [45]. If limited to tens or even few hundreds of nanometers in diameter, nanowires prove difficult to use for optoelectronics. While electrons are spatially localized within a few nanometers, it is difficult to squeeze light below the length scale of its wavelength. It is therefore difficult to squeeze and manipulate light in conventional nanowires, physical objects significantly smaller than optical wavelengths. If we consider a wavelength of 1.55 µm and a material refractive index of 3.5, then a 440 nm diameter structure can fit just about a single wavelength inside. Furthermore, conventional nanowire growth often requires either gold catalysts or high temperatures or both, all factors that are highly detrimental for CMOS compatibility [20], [46].

Thus, conventional nanowire systems are promising, yet quite limited for the purposes of optoelectronic integration onto Si. The ultimate system for III-V integration with CMOS should feature: (1) even greater lattice mismatch accommodation to grow larger III-V single crystals on Si, (2) low temperature growth to meet CMOS thermal budget restrictions, and (3) Au-free growth to prevent harm to Si devices. With these challenges highlighted, we must nonetheless recognize that high-aspect ratio structures like nanowires have gained considerable traction recently even in the realm of electronics. FinFETs have emerged as the primary technology for the upcoming 14 nm node, and III-V nanowire channels have increasingly attracted interest from industry [47]–[51]. These trends make III-V nanomaterial integration onto Si all the more urgent.

In the next section, we therefore introduce a relatively new class of nanomaterials that exhibit the desirable properties highlighted above. These nanoneedles and nanopillars on silicon form the basis of the nano-optoelectronic devices presented throughout the rest of this dissertation. We first summarize the unique growth mechanism of nanoneedles and nanopillars and their optical properties before experimentally proving their worth as III-V optoelectronic device materials in later chapters.

2.3 Nanoneedles and nanopillars

Owing to both physics and the tremendous effort that has gone into their development, Si and III-V compounds have become the principal materials for electronics and photonics, respectively. Naturally then, the integration of these two materials appears to be a pathway towards optoelectronic functionality. However, as described in Section 2.1.1, severe mismatch in lattice constants and thermal expansion coefficients has greatly inhibited progress. Section 2.2 meanwhile introduced semiconductor nanomaterials and touched on how they might aid in overcoming these obstacles. This section discusses a particularly relevant and recently developed class of such nanomaterials: nanoneedles and nanopillars on silicon. As will be shown, these materials possess many unique properties that make them particularly attractive for optoelectronic integration. For this reason, nanoneedles and nanopillars on silicon are at the heart of the optoelectronic devices presented throughout the rest of this dissertation. The history and growth of these nanostructures is briefly summarized here before presenting their basic optical properties.

2.3.1 Growth

The discovery of nanoneedles and nanopillars on Si was serendipitous, but their development was fervently pursued after immediately recognizing their potential for optoelectronic devices [44], [52]. Figure 2.3a shows a scanning electron microscope (SEM) image of a GaAs nanoneedle, while Fig. 2.3b shows one of InGaAs nanopillars. Nanoneedles and nanopillars share the same growth mechanism, but their geometries differ and are controlled by subtle variations in growth parameters such as temperature and material composition. As shown in the inset of Fig. 2.3a, nanoneedles possess

extremely sharp tips that can taper down to just a few atoms in width [53]. Nanopillars can meanwhile be categorized as a subset of nanoneedles exhibiting truncated and flat tops. Notably, these materials can grow on a variety of substrates beyond just crystalline silicon. As an example, the nanopillars shown in Fig. 2.3b were grown on polysilicon. Past experiments have meanwhile demonstrated growth on GaAs substrates and even insulators such as sapphire [53], [54].

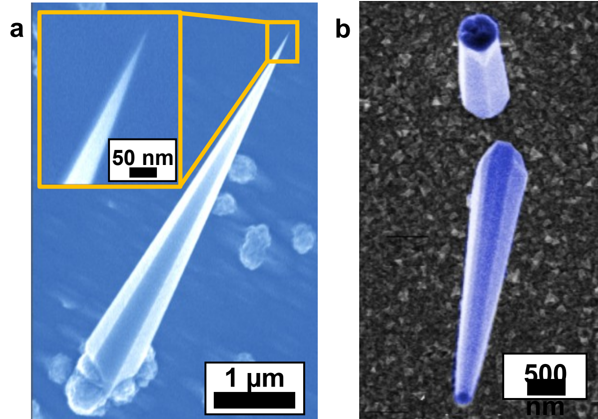

Figure 2.3. SEM images of nanoneedles and nanopillars on silicon. a, An SEM image adapted from ref. [53] shows a GaAs nanoneedle grown on silicon. The nanoneedle tapers down to an atomically sharp tip as highlighted by the inset. **b,** Nanopillars can also grow with truncated tops as shown in this SEM image adapted from ref. [55]. In this case, growth occurred on a polysilicon substrate, showcasing the diversity of the nanoneedle/nanopillar growth mechanism.

Like nanowires, nanoneedles and nanopillars can grow monolithically on lattice-mismatched substrates. However, they have three decided advantages over conventional nanowire growth methods when it comes to optoelectronic integration on Si. Unlike many nanowires grown via VLS, nanoneedle-based growth does not require Au catalysts, which would otherwise be poisonous to Si devices. Additionally, nanoneedle dimensions are not limited to a small critical diameter beyond which material quality drastically deteriorates [45]. In fact, nanoneedle and nanopillar growth can form microstructures just as well as it forms nanostructures. Nanoneedles grown shorter than 100 nm to longer than 9 μm all share similar shapes, features, and quality [54]. Being able to scale the dimensions of these III-V materials has important practical implications from a device perspective. Microstructures are often more well-suited for optical devices because they better match the wavelength of light and can better survive the rigors of fabrication processes. Thus, nanoneedles and nanopillars provide III-V active materials with dimensions and robustness that better fit optoelectronic device fabrication. Finally, nanoneedle-based growth occurs at a low temperature of 400 °C, making it compatible with BEOL integration approaches [22]. Conventional nanowire and epitaxial growth temperatures typically well exceed 600 °C, which would damage any pre-existing

electronics on growth substrates. III-V growth onto post-foundry CMOS chips would thus be very challenging.

Briefly discussing the growth mechanism will reveal insight into how nanoneedles and nanopillars can grow to the larger dimensions favorable for device fabrication. Figure 2.4 schematizes the growth process. Nanoneedles form through layer-by-layer material deposition as source molecules flow into the growth chamber. Growth includes both nucleation of a single crystal nanoneedle and the epitaxial deposition of a thin film that becomes polycrystalline due to lattice mismatch with the substrate. Because these two processes occur simultaneously, the root of the nanoneedle assumes an inverse-tapered shape. This ultimately means that only a small footprint exists between the single crystal nanoneedle and the lattice-mismatched substrate even as the nanoneedle dimension scales with growth time. As a result, strain effects due to the Si-nanoneedle interface do not magnify with growth time, and nanoneedles remain high-quality single crystals from the nanoscale to the microscale.

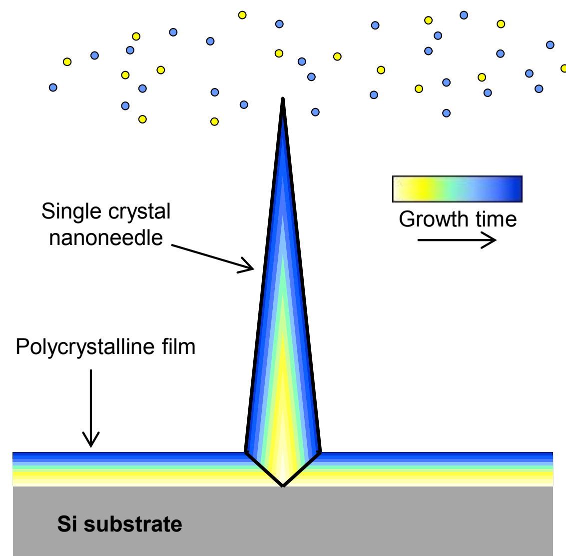

Figure 2.4. Core-shell growth of nanoneedles. Core-shell growth of nanoneedles enables growth of large III-V single crystals on lattice-mismatched Si by maintaining a minimum interface with the substrate.

Another benefit of this core-shell growth behavior is the ability to form sophisticated junctions and lattices by controlling the properties of each layer. As an example, Fig. 2.5 illustrates how ternary compounds and heterostructures can be grown. First, indium, gallium, and arsenic sources are introduced into the MOCVD chamber such that ternary InGaAs nanoneedles and nanopillars nucleate and grow. Subsequently, the indium source is turned off while the gallium and arsenic sources continue to work. An outer GaAs shell then forms around the InGaAs nanopillar core to create a core-shell heterostructure. In this case, the utility of finely controlling each layer's composition is surface passivation of InGaAs with a higher band gap material. Even higher band gap compounds such

AlGaAs can also be grown. Meanwhile, leveraging these various compound compositions and controlling layer thicknesses at the nanometer scale can result in GaAs/AlGaAs as well as InGaAs/GaAs quantum well growth. Finally, as Chapter 5 will show, combining this core-shell capability with doping can result in the formation of radial p-i-n heterojunctions needed for electrically-controlled devices.

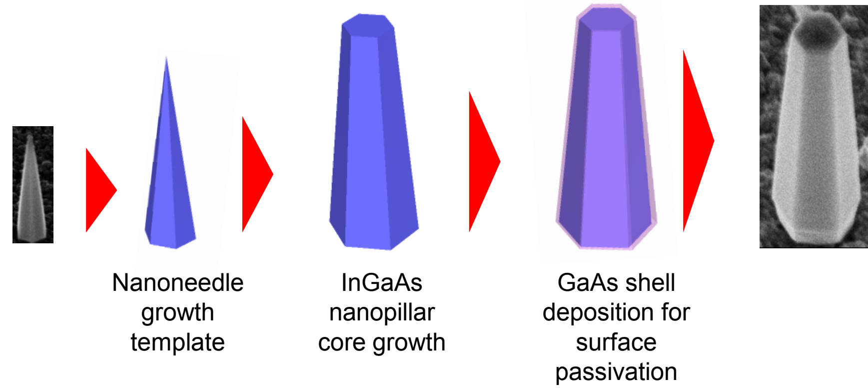

Figure 2.5. Growth evolution of nanopillar heterostructures. An InGaAs nanoneedle structure first nucleates on silicon. Under the proper conditions, vertical growth is halted such that the nanoneedle is transformed into a nanopillar structure. The InGaAs nanopillar core is then cladded by a GaAs shell to complete the heterostructure, which provides in-situ surface passivation.

Here, we briefly describe the technical details of nanopillar growth to offer a sense of methodology. Deeper knowledge of this topic can be accessed through the works of Chuang and Moewe, the pioneers of this growth method [44], [52]. To grow InGaAs nanopillars, a silicon substrate is first cleaned with acetone, methanol, and water for 3 minutes at each step. Afterwards, the substrate is deoxidized by buffered oxide etch for 3 minutes, and the surface is mechanically roughened. Growth is subsequently carried out in an EMCORE D75 MOCVD reactor. Tertiarybutylarsine (TBA) is introduced to the reactor at temperatures higher than 200 °C. Before growth, in-situ annealing at 600 °C is performed for 3 minutes. After annealing, the temperature is reduced to the growth temperature, which is 400 °C in this work, in 3 minutes, followed by 2 minutes of temperature stabilization. Triethylgallium (TEGa) and Trimethylindium (TMIn) are then introduced to the reactor to begin the 60-min InGaAs core growth. TMIn mole fractions are kept constant at 9.86×10^{-7}, 1.38×10^{-6}, and 1.73×10^{-6} for 12%, 15% and 20% indium compositions, respectively. The TEGa mole fraction is held at 1.12×10^{-5}. All sources use a 12 liter/min hydrogen carrier gas flow. The TBA mole fraction is 5.42×10^{-4}; hence, the V/III ratio is ~43. A GaAs shell is then grown around the InGaAs core with the same TEGa and TBA mole fractions used for core growth, with a V/III ratio of 48. Nanopillar growth is vertically aligned to the (111) silicon substrate and anisotropic with faster growth rates along the [0001] wurtzite c-axis. Nanopillar dimensions are linearly scalable with time with no critical dimensions observed.

2.3.2 Photoluminescence

Knowing the optical processes of III-V semiconductors is crucial for understanding how to leverage them for opotoelectronic applications. Characterizing light-matter interaction within materials is therefore paramount, and the photon provides a powerful probe for such investigations. A particularly useful characterization tool is photoluminescence spectroscopy. Part of its utility is in the elegance and simplicity of the concept. First, a photon supplied by an external source, often an excitation laser, impinges upon a material of interest. This photon is absorbed by the material, exciting an electron-hole pair. Various electronic as well as optical processes then influence this electron-hole pair, which may or may not recombine to emit a photon in response. It is this response that offers a wealth of information about the material. The intensity as well as the spectral properties of the emitted photon can reveal the material's band gap, scattering properties, recombination dynamics, and more. As characterization becomes more sophisticated, finer nuances about a material's behavior can be extracted. The rest of this section will summarize some basic optical properties of nanoneedles and nanopillars as revealed by photoluminescence spectroscopy.

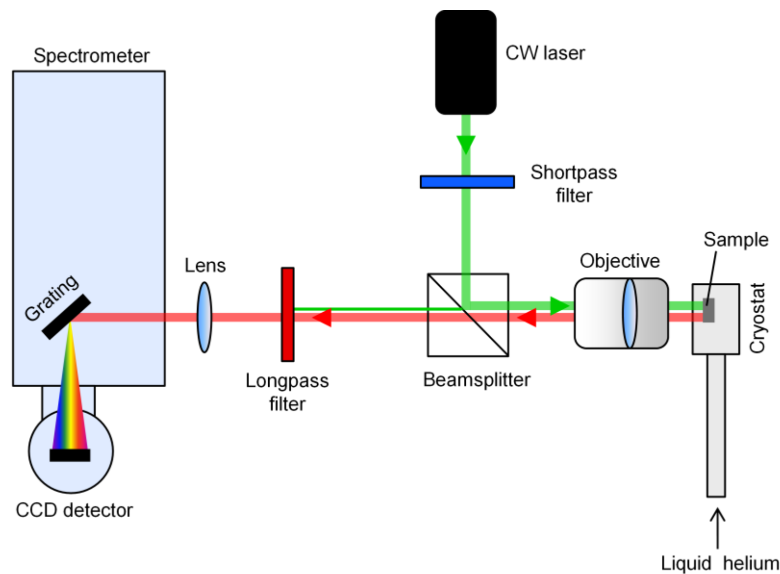

Figure 2.6. Photoluminescence setup.

Figure 2.6 shows a schematic of a simple μ-photoluminescence setup used for characterizing nanoneedles and nanopillars. It is a physical manifestation of the previously described process of photoluminescence spectroscopy. Such setups are often highly flexible. Simple addition, removal, or rearrangement of optical components can implement completely different spectroscopic functions. The setup shown here was used for the simple function of exciting and collecting PL. Figure 2.7 shows various PL spectra collected by this setup for the various nanoneedle structures described in the previous section. Specifically, it co-plots normalized data for GaAs and AlGaAs bulk

nanoneedles as well as GaAs/AlGaAs and InGaAs/GaAs quantum well nanoneedles. Continuous wave (CW) green laser sources were used to excite the emission at 4 K.

As expected, we observe different peak wavelengths for different compounds. For GaAs nanoneedles, the peak wavelength is around 821.5 nm, which is redder than the commonly accepted band gap of 818 nm for GaAs crystals. This could be due to the unique wurtzite (WZ) lattice of nanoneedles. Perhaps the band gap of WZ GaAs is slightly smaller than the band gap for zincblende (ZB) GaAs, the crystal form most commonly seen. However, it is more likely that acceptor and donor states exist, creating near-band edge emission. Past Raman and temperature dependence measurements suggest this to be true [56]. Meanwhile, bulk AlGaAs nanoneedles show two main PL peaks at 4 K. One exists near 680 nm, while the other is around 900 nm. The 680 nm peak is attributed to the band gap E_g of AlGaAs, which suggests an aluminum content x of 22% according to the following equation governing band gap composition dependence at 0 K [57]:

$$E_g = 1.519 + 1.447x - 0.15x^2 \text{ (eV)} \qquad (2.1)$$

The 900 nm peak is meanwhile ascribed to mid-gap states due to defects. It is actually brighter than the AlGaAs peak, which is not surprising as AlGaAs is known to be a poor emitter. Though not shown, AlGaAs emission is orders of magnitude weaker than GaAs emission.

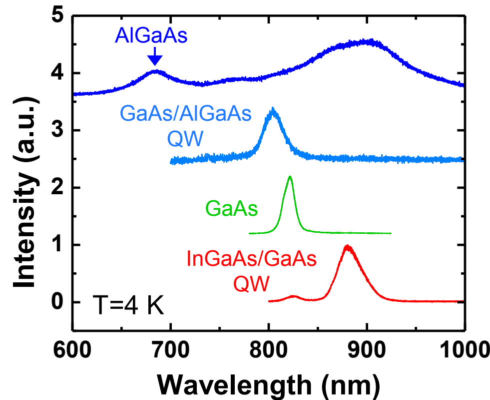

Figure 2.7. Photoluminescence spectra for various nanoneedle materials. GaAs-based nanoneedle materials can form quantum wells and ternary compounds. PL spectra are shown for a variety of nanoneedle structures including bulk GaAs and AlGaAs as well as GaAs/AlGaAs and InGaAs/GaAs quantum well.

Sandwiching a thin layer of GaAs between AlGaAs barriers results in a GaAs/AlGaAs quantum well that emits at bluer wavelengths when compared to bulk GaAs. Quantization is responsible for this effect. In Fig. 2.7, the light blue trace shows the PL spectra of a 10 nm GaAs/AlGaAs QW with emission peaking at 804 nm. For a

different type of QW nanoneedle, namely a 10 nm InGaAs/GaAs one, emission at much redder wavelengths is possible. In this case, the QW emission plotted in red peaks at 880 nm. Notably, a weaker second peak also exists at a wavelength that matches that of bulk GaAs emission. This is due to electrons and holes spilling into and recombining within the GaAs portions of the InGaAs/GaAs quantum well structure.

In Fig. 2.8, the effect of varying material composition has been captured by PL spectra for bulk InGaAs nanopillars of different indium content. As indium content increases, the associated band gap reduces, and thus the peak wavelength of emission increases. For 12%, 15%, and 20% indium content, emission is centered at 918 nm, 947 nm, and 1003 nm, respectively. Spectra tend to also broaden for higher indium content because of nonuniform indium distribution and segregation as suggested in the figure.

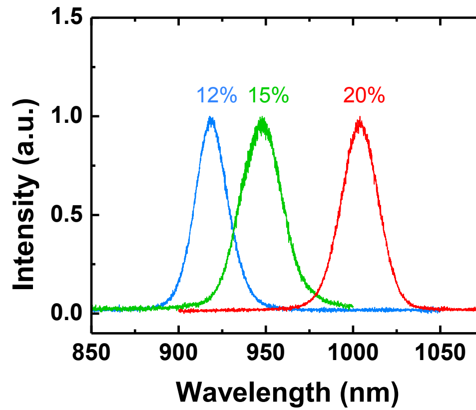

Figure 2.8. Indium composition variation for emission wavelength control. Nanopillar spontaneous emission spectra at different indium compositions show the wavelength tunability of nanopillar emission. In this work, the composition is varied from 12% to 20%. The ability to control the emission wavelength offers an important optoelectronic device design parameter.

2.3.3 Spatially-resolved and polarized emission

Optical transitions are often polarized, which is usually represented by including vectors in the transitions' matrix elements. Naturally, different transitions often have different polarizations. Thus, characterizing the polarization of optical emission often helps one understand the origin of that emission. Quantized materials such as quantum wells are particularly prone to exhibiting polarization effects [57]. Anisotropic crystals are another class of materials that often emit polarized light [58]. Wurtzite (WZ) nanoneedles and nanopillars, the materials studied throughout most of this dissertation, are anisotropic crystals that can also form quantum wells. Strong polarization effects are thus expected. This section reviews their polarization characteristics in an effort to better understand these unique materials. Polarization measurements reveal anisotropy behavior that is reminiscent of GaN and other wurtzite materials.

Both nanoneedles and nanopillars were used for this study. Quantum well nanoneedles were investigated as well. The materials were all grown on either a c-plane sapphire substrate or (111) Si. For the QW nanoneedles, a pure WZ-GaAs core was first grown to a nominal height of 4 μm and a base diameter of 600 nm. The core was then wrapped by an $In_{0.17}$ $Ga_{0.83}As$ shell grown to a nominal thickness of 6 nm, followed by a pure GaAs cladding with a nominal thickness of 50 nm. Figure 2.9 illustrates the quantum well structure and shows typical scanning electron microscope images. To facilitate spatially resolved PL and polarization measurements, core-shell nanoneedles were mechanically wiped onto a clean sapphire substrate. By doing so, polarization could be measured with respect to the nanoneedle's longitudinal c-axis. Otherwise, emission could only be collected from above the tip of a nanoneedle.

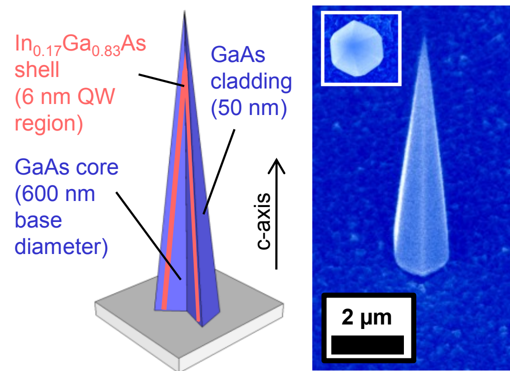

Figure 2.9. Schematic and SEM image of a quantum well nanoneedle a, Schematic showing the structure of core-shell InGaAs/GaAs quantum well nanoneedles. **b,** 30º tilt-view false-color SEM image of an as-grown core-shell nanoneedle. The inset shows a top-view image that reveals the six facets of the hexagonal nanoneedle.

Figure 2.10 shows a schematic of the PL setup used for spatially resolving polarized emission from nanoneedles. Nanoneedle samples were mounted in a cryostat for PL measurements at 4 K. A 100x 0.7 numerical aperture (NA) objective focused excitation light from a 660 nm laser diode to a ~1 μm spot and collected back-generated PL in reflection mode. Filters separated laser light from the collected PL emission, which was subsequently divided into two paths by a beamsplitter. A polarizer in one path passed only PL of a certain polarization while another polarizer in the second path passed only light of the orthogonal polarization. A second beamsplitter then recombined the two orthogonally polarized signals so that they can be coupled to a spectrometer and LN_2-cooled Si CCD. The orthogonal PL emissions were slightly displaced from each other so that they disperse onto different regions of the CCD, allowing simultaneous polarization measurements to ensure that both polarizations arise from the same region of the sample. This mitigated any impact from drift or physical instability during the experiment. A piezo-stage was used to scan the objective in order to spatially resolve

photoluminescence from nanoneedles. The maximum displacement of the objective was 20 µm, which did not significantly impact light coupling into and out of the objective's back aperture.

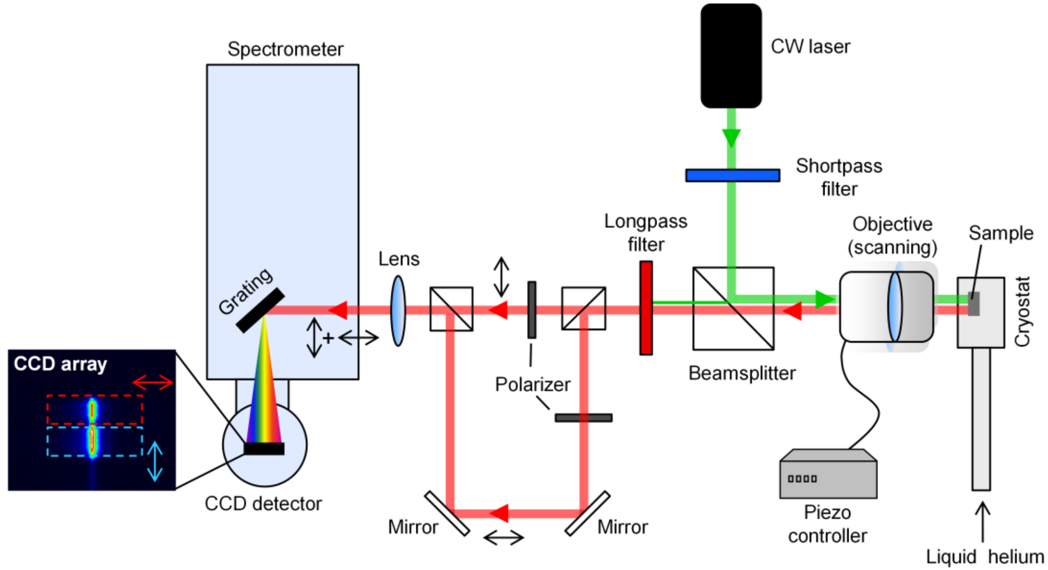

Figure 2.10. Experimental setup for simultaneously measuring orthogonal polarizations while spatially mapping photoluminescence.

Figure 2.11a shows polarization dependent PL spectra from a single InGaAs/GaAs QW nanoneedle. The emission at ~847 nm arises from the InGaAs quantum well, which agrees reasonably well with simple predictions assuming an infinite square well model. The shoulders observed at ~818 nm and ~823 nm are attributed to bulk GaAs recombination and impurities, respectively. Defined as $\rho=(I_{\perp}-I_{\parallel})/(I_{\perp}+I_{\parallel})$, the polarization ratio of the QW nanoneedle emission is approximately 0.4, which is significant for typically isotropic GaAs materials. $I_{\perp}$ and $I_{\parallel}$ are PL intensities polarized across and along the nanoneedle c-axis, respectively. To investigate if polarization anisotropy is due to the QW structure, polarization measurements were also performed on large bulk GaAs nanoneedles about 9 µm long with 1.5 µm bases as shown in Fig. 2.11b. Because bulk GaAs nanoneedles exhibit the same polarization behavior and nanoneedles are large enough to minimize polarization effects seen for very thin nanowires, wurtzite crystal structure is attributed as the origin of the polarization anisotropy [59]. In GaN and II-VI wurtzite materials, macroscopic polarization anisotropy arises because of crystal asymmetry and the highly ionic nature of the atomic bonds [3]. We observe a similar effect for wurtzite GaAs, though its polarization ratio is reduced most likely because of the less ionic nature of GaAs.

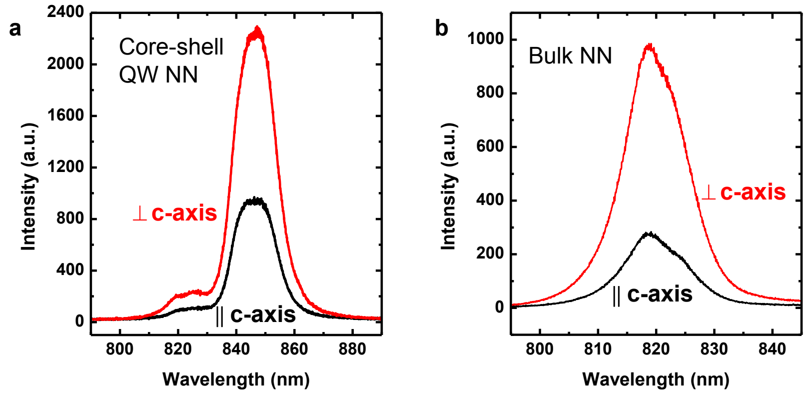

Figure 2.11. Polarized photoluminescence from nanoneedles. μ-PL from **a,** a single core-shell nanoneedle (NN) and **b,** a single bulk GaAs nanoneedle polarized ⊥c-axis (red) and ‖c-axis (black). Both types of nanoneedles exhibit anisotropy with preference for emission polarized ⊥c-axis, indicating macroscopic spontaneous polarization effects due to the wurtzite crystal structure.

Polarization properties of PL from bulk InGaAs/GaAs double heterostructure nanopillars were also measured. Figure 2.12 presents the polarization dependence over π radians. Clear lobes in the polar plot of integrated intensity versus polarization angle clearly show that emission is preferentially polarized perpendicular to the c-axis of InGaAs/GaAs nanopillars. This further supports the previous claim that polarization in PL likely arises from the anisotropic nature of WZ crystals. For nanopillars, the polarization anisotropy is ratio is 0.6, slightly more than that for nanoneedles. The reason for this difference remains unclear, but it may very well be due to the fact that InGaAs and GaAs are significantly distinct materials despite their similarities.

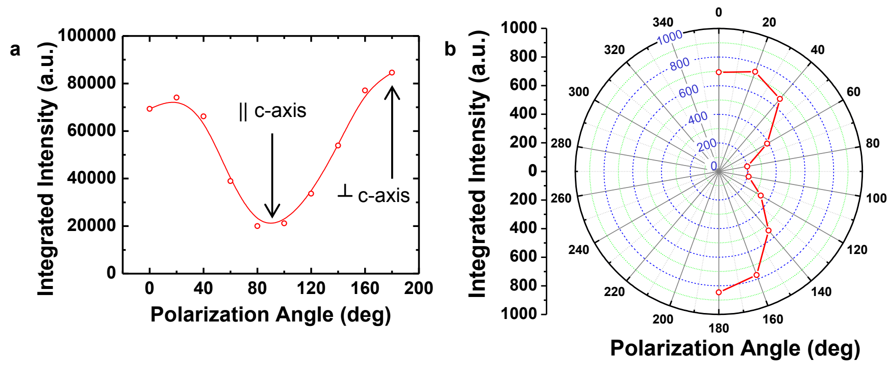

Figure 2.12 Polarized photoluminescence from nanopillars. Polarized emission from nanopillars is plotted in **a,** x-y and **b,** polar forms. Photoluminescence is strongly polarized perpendicular to nanopillars' longitudinal c-axis. This polarization arises from the material itself and not from optical antenna effects.

Spatial PL scans in Fig. 2.13 further elucidate that PL emission favors polarization perpendicular to the c-axis of the nanoneedle. They also reveal that emission from nanoneedles can be quite nonuniform in space. Figure 2.13c shows that the QW emission dominates towards the nanoneedle tip while bulk GaAs emission dominates at the base. The spectral image in Fig. 2.14a illustrates that QW emission intensifies and slightly redshifts towards the tip. Spectra in Fig. 2.14 confirm the nonuniformity of PL and the formation of good quality, bright QWs near the nanoneedle tip. Furthermore, they reveal that polarization anisotropy exists throughout the crystal despite the clear nonuniformity of the QW, reinforcing the idea that it is due to the wurtzite crystal structure. We suggest that indium composition fluctuation or well width variation along the nanoneedle may explicate the redshift observed towards the NN tip.

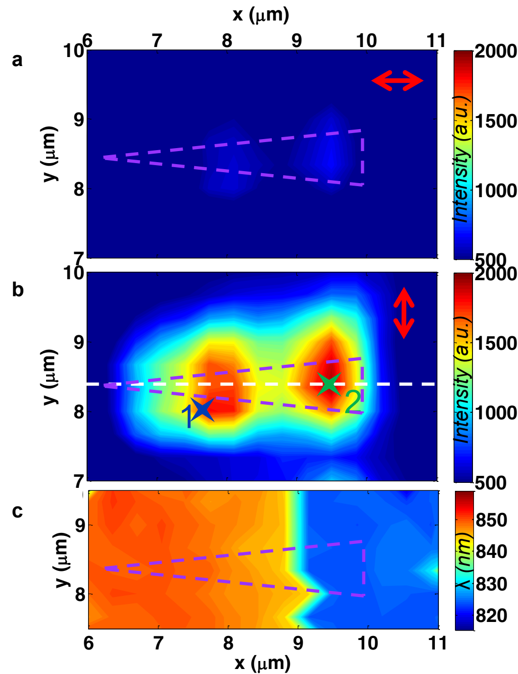

Figure 2.13 Contours of spatially resolved PL from a single core-shell nanoneedle. Emission polarizations are **a,** ∥c-axis and **b,** ⊥c-axis. **c,** Contour of the PL peak wavelength. The broken triangles (purple) show the nanoneedle orientation.

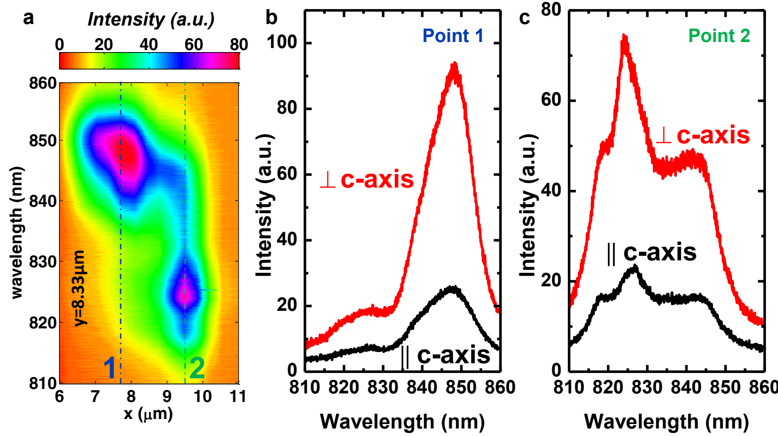

Figure 2.14 Spectral properties of polarized emission. a, Spectral image showing nonuniform nanoneedle PL emission along the white dashed line in Fig. 2.13b. Core-shell quantum well emission intensifies and redshifts towards the tip of the nanoneedle while emission at the base is primarily from the GaAs core and cladding. Polarization dependent PL spectra are shown for positions **b,** near the nanoneedle tip and **c,** by the nanoneedle base as marked by points 1 and 2 in part **a** and Fig. 2.13**b**.

2.3.4 Time-resolved photoluminescence

When characterizing photoluminescence from a material, it is useful to consider not only the spectral domain, but also the time domain. Much insight about physics can be collected by measuring how quickly carriers recombine after a short excitation event [60]–[64]. Because the light output of a semiconductor directly depends on carrier concentration, measuring the time dependence of PL emission indirectly measures carrier recombination rates. Many methods exist for resolving photoluminescence in time, one of which is time-correlated single-photon counting (TCSPC).

Figure 2.15 illustrates the physical implementation of the TCSPC method for time-resolved photoluminescence measurements [65], [66]. The advantage of this method lies in its simplicity and flexibility. Also, highly sensitive and off-the-shelf detectors such as photomultiplier tubes (PMTs) or avalanche photodiodes (APDs) can be easily integrated. A drawback is the lower time resolution of TCSPC compared to other methods. TCSPC systems are often limited by the time resolution of detectors, which is often several tens of ps. For measuring ultrafast phenomena in the few ps or even fs range, this is inadequate. For our purpose of measuring radiative and other lifetimes, which are on the order of hundreds to thousands of ps, it is more than sufficient.

In TCSPC, an excitation pulse from a fs Ti:sapphire laser (or any other ultrafast source) impinges upon a sample at a regular frequency (80 MHz here). This pulse effectively acts as an optical impulse function for stimulating the impulse response of the

material. Over a short timeframe, the incident pulse quickly generates electrons and holes, which begin to recombine via various mechanisms. Because no new electron-hole pairs are generated after the excitation pulse disappears, electron and hole concentrations will deplete. As a result, PL emission decreases with time since its intensity depends on the amount of free electrons and holes in the material. Thus, measuring this decay in PL emission intensity measures how electron and hole concentrations decay, and as such, it characterizes the recombination paths taken by these charge carriers.

Lifetime, the time constant of this decay, is a convenient parameter for characterizing recombination. Short lifetimes imply that a recombination mechanism is strong; longer lifetimes indicate the opposite. TCSPC measures lifetime using a fast electronics timing card that records the time delay (Δt) between an excitation event and an emission event. In other words, the excitation and emission events function as the start and stop points for the timing card, respectively. Timing for the start point is supplied by a periodic electrical output from the fs laser that is synchronized to periodicity of the laser's output optical pulse train. The start point serves as a constant point of reference in time. Meanwhile, an optical detector outputs a TTL pulse that signals the timing card to stop counting upon detecting PL. The difference between these start and stop points is the aforementioned Δt.

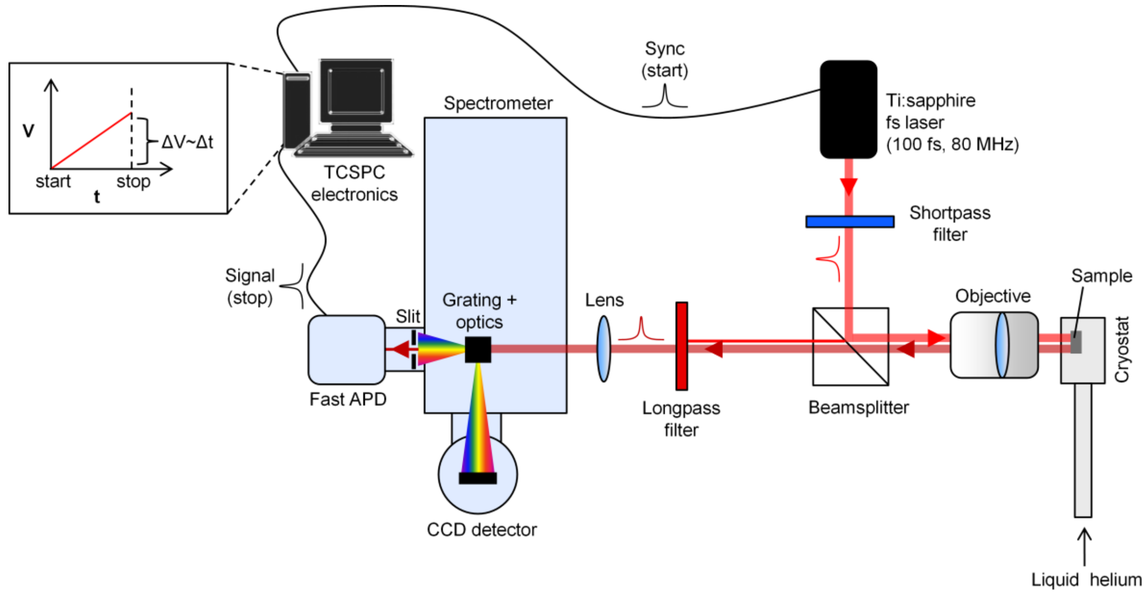

Figure 2.15. Experimental setup for time-correlated single photon counting.

Under certain conditions, the probability of recording a certain Δt value is directly proportional to the probability that electron-hole pairs recombine at that time Δt after excitation. Thus, by repeating this measurement for many periods of excitation pulses, the timing card can measure the probability of photon emission versus time. It does so by binning values for Δt and building up a histogram, which effectively is the PL decay

curve of a material. The time constants of this curve will reflect the recombination lifetimes of the sample.

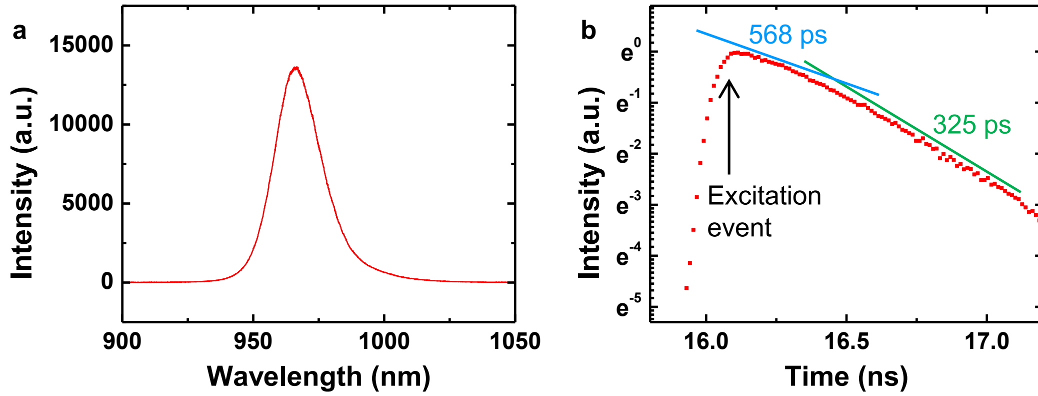

Figure 2.16. Time-resolved photoluminescence decay. The photoluminescence shown in **a,** was also **b,** resolved in time to reveal insight into nanopillar recombination dynamics. The interesting shape of the decay curve is explained in the main body of text.

Figure 2.16 shows an experimentally measured PL decay curve and its associated PL spectrum. For this experiment, measurements were performed on InGaAs/GaAs bulk nanopillars using the TCSPC method described above. Notably, two lifetimes appear to exist. Shortly after excitation, PL decays with a time constant of 568 ps. After some time, this time constant actually accelerates to 325 ps. This effect is somewhat odd and counterintuitive. When multiple time constants exist in an exponentially decaying function, terms associated with the fastest time constants should disappear more quickly. This means that shortly after an excitation event, the fast component of PL emission should decay before the slow component. The slow component meanwhile continues to decay for some longer time.

The results shown in Fig. 2.16b are completely opposite to this logic. This oddity can be explained by considering the impact of carrier concentration on recombination rates, which is illustrated in Fig. 2.17. Carrier lifetimes limited by nonradiative recombination are relatively constant at low carrier concentrations, However, they tend to increase as carrier concentration or excitation grows significantly. This is due to the saturation of nonradiative states as a wealth of carriers fills them. If carrier concentration is increased further, radiation can begin dominating carrier recombination in an otherwise usually nonradiative-limited material. This is because radiative recombination rates grow exponentially with carrier concentration.

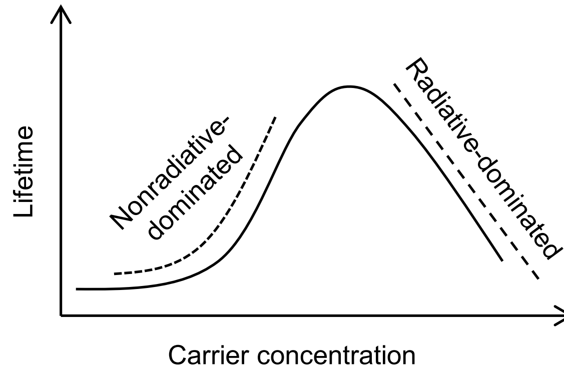

Figure 2.17. Carrier concentration dependence of carrier lifetime. For some materials, carrier lifetime can be either nonradiative-dominated or radiative-dominated depending on the carrier concentration.

Returning to Fig. 2.16b, it therefore makes sense that immediately after a very strong excitation event, carrier concentration can be high enough that recombination is radiative limited, and lifetime is long. Then, as carrier concentration decreases, nonradiative states open up and their fast recombination rates begin to dominate. Thus, slow decay can be followed by fast decay [67]. These results have important implications for optoelectronic devices based on nanoneedles and nanopillars. They reveal that these materials are at present limited by nonradiative recombination. This has less impact on lasers because nonradiative recombination can be suppressed with strong current injection, but it can negatively affect other optoelectronic elements like photodetectors and solar cells. Future work should be devoted to improving material quality such that recombination is dominated by radiative processes even at low carrier concentrations.

Chapter 3

Nanophotonic phenomena

In Chapter 2, we reviewed existing approaches towards optoelectronic integration on silicon, and we ended by suggesting that III-V nanomaterials perhaps provide the most suitable roadmap towards this endeavor. Using nanomaterials inevitably means that nanophotonics will have to play a major role in optoelectronic device design, especially as we seek to reduce the physical dimensions of photonic devices to better match their electronic counterparts. In this chapter, we thus present some thoughts on nanophotonic phenomena, and we show that the nanoneedles and nanopillars mentioned in Chapter 2 feature attractive nanophotonic properties that prove instrumental for device applications.

3.1 Subwavelength light using metal

We begin this chapter by first reviewing the development of subwavelength optical devices, which have rapidly emerged over recent years. To manipulate light at dimensions near or below its wavelength, metal is often leveraged for its unique optical properties. In particular, it has a fascinating inherent ability to reflect, focus, localize, and enhance light [68]–[70]. Some of these capabilities arise from plasmonic effects [71], which are illustrated in Fig. 3.1. Light can excite collective electron oscillations in metal that strongly confine electric fields within small volumes, which can be significantly subwavelength.

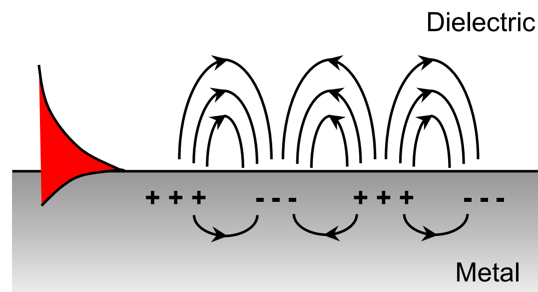

Figure 3.1 Plasmonic localization of electric fields. Collective electron oscillations in metal can generate optical electric fields that are tightly confined to metal surfaces.

This unique ability to localize light has paved the path for many novel devices recently, especially devices involving light emission. Nanolasers have been demonstrated at deep subwavelength scales [72], [73], and devices exhibiting surface plasmon amplification by stimulated emission of radiation or SPASERs have been shown [74]–[76].

Because metal has high optical loss, some researchers have focused on structures that are more optical than plasmonic. In these metal-optic devices, metal functions primarily as a reflector, though plasmonic effects certainly play a role. The benefit of metal-optics versus plasmonics is the ability to achieve subwavelength optical confinement at a distance farther away from lossy metal surfaces. Nanopatch [77] and metallo-dielectric nanolasers [78] have been demonstrated using this approach, which may be promising for not only small, but also efficient emitters. In addition to emitters, plasmon-enhanced photodetectors and even photovoltaics have been shown [79], [80]. And to model this whole new class of photonic devices, circuit analysis methods for metal-optics have been developed [81].

In this dissertation, we primarily leverage metal-optic rather than purely plasmonic effects. Implementing optical interconnects is a primary motivation for the nano-optoelectronic devices we have developed, and high energy efficiency is a primary requirement for optical interconnects [14]. We would therefore prefer avoiding metal loss altogether if possible, though as we show in Chapter 5, incorporating metal-optics is inevitable when attempting to electrically drive nanolasers. The presence of metal contacts is relatively prominent since the active material is small, and it becomes more practical to design for the presence of metal than to design around it. Before we get to Chapter 5 though, we show that purely optical modes are very promising for nano-optoelectronic devices as well. The next section introduces a particularly interesting class of nanophotonic modes that prove instrumental for achieving nanolasers as shown in Chapter 4. Even when metal is incorporated, these modes exist and are simply augmented by metal-optic effects.

3.2 Helically-propagating modes

The laser plays a critical role in the field of optoelectronics, and it relies on coupling optical resonances to optical gain. Chapter 4 discusses lasers in further detail, but here it is worthwhile to devote some discussion to understanding the optical resonances of nanopillars on silicon. After all, as III-V semiconductors, nanopillars already provide strong optical gain. If the nanopillar geometry additionally supports resonances, then both gain and resonances may be leveraged to realize lasers on silicon, which surely would be a boon to optoelectronic integration.

In order to explore potential feedback mechanisms for nanopillars on silicon, calculations were performed using a commercial finite-difference time-domain (FDTD) simulation package (Lumerical). A conscious decision was made to use FDTD because the complexity of the three-dimensional nanopillar geometry makes analytical analysis

unwieldy. Per its name, FDTD is a time-domain calculation. Sources are usually pulsed, and the time decay of the fields in a simulated structure is numerically calculated. Fourier analysis of the time decay then reveals the frequency properties of the structure and thus its resonances. The accuracy of frequency domain data depends greatly on simulation time. After all, exact Fourier analysis requires complete knowledge of time-domain behavior.

Carefully choosing excitation sources is important for effective and accurate FDTD simulations. These sources, whether dipoles, Gaussian beams, or plane waves, excite resonances inside optical structures. Different placement and orientation of different sources will excite different resonances to varying degrees. In our case, most simulations used dipoles to excite resonances inside nanopillars. Dipoles provide a simple light source that can couple to a large diversity of optical modes. They also best simulate the spontaneous emission that III-V semiconductors naturally exhibit. Upon discovery, specific nanopillar modes were sometimes directly injected in simulations to excite that mode alone. In some instances, dipoles simultaneously excite too many modes such that their crosstalk or interplay can make characterizing each individual mode difficult.

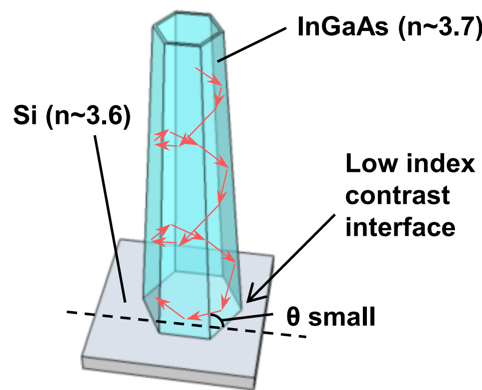

Figure 3.2 Ray model visualization of helically-propagating modes. Helically-propagating modes can strongly reflect from low-index contrast interfaces to tightly confine light within nanopillars integrated on silicon.

For nanopillars on silicon, confining light inside the nanopillar is not an easy proposition. The boundary between silicon substrate and InGaAs nanopillar is expected to be a major source of light leakage, inhibiting resonances and optical feedback for nanopillars. It is therefore an important interface to study, and FDTD provides a powerful tool for this task. For all simulations shown in this section, silicon absorption is included to account for possible absorption losses near the nanopillar-silicon interface.

Because the index of silicon is so similar to that of InGaAs, there is likely insufficient reflection from that interface for pure Fabry-Perot (FP) modes. It is therefore expected that traditional FP modes will not provide strong optical feedback. Though not shown here, FDTD simulations confirm this. Interestingly, a different type of mode with

some FP characteristics does offer reasonable reflection from that interface. Using the ray model concept, this mode can be best described as a helically-propagating mode as schematized in Fig. 3.2. Though the mode travels along the axis of the nanopillar, it contains very strong radial and azimuthal components as embodied by the spiralling path it traverses. When the mode reaches the Si substrate, its shallow incidence on that boundary means even minimal index contrast can offer total internal reflection. This interpretation is incomplete as this section later discusses, but it offers a useful visualization of how helical modes behave. The apparent circulation of light for helical modes is highly reminiscent of whispering gallery (WG) modes. As the rest of this section will show, helically-propagating modes are effectively a hybridization of both FP and WG effects.

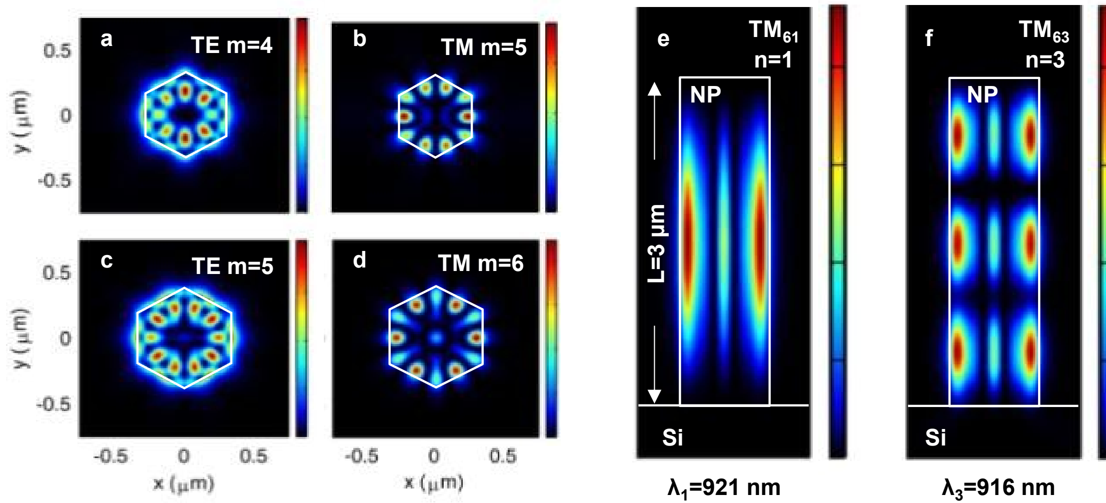

Figure 3.3 Helically-propagating mode field patterns. a-d, Transverse field patterns for various azimuthal modes and polarizations. **e-f,** Axial field patterns along the length of nanopillars also show standing waves.

Examining the transverse field profiles of helically-propagating modes provides an instructive starting point for understanding their behavior. Figure 3.3 shows some of these profiles. The field patterns shown are very similar to WG modes previously reported for hexagonal nanowires, and we therefore use a similar notation and convention here [82], [83]. Transverse magnetic (TM) is defined for when the mode's electric field is polarized along the longitudinal axis of a structure with hexagonal symmetry. In the context of Fig. 3.3a-d, a TM mode is polarized out of the page. Transverse electric (TE) then is the case when electric field is polarized perpendicular to the longitudinal axis.

While the transverse field profiles are suggestive of WG modes, standing wave patterns also exist in the axial direction as shown by Figs. 3.3e,f. This axial behavior reminds one FP modes, but unlike FP modes, helical modes clearly reflect very strongly from the interface with silicon. For the nanopillars on silicon introduced in Section 2.3,

this offers a clear means of trapping light inside a small structure with an otherwise leaky faucet on the substrate side. Exhibiting characteristics of both WG and FP modes, helical modes may appear perplexing at first, but their value is immediately clear, especially for resonator applications like lasers.

Figures 3.3a-d show both TE and TM modes with azimuthal mode orders ranging from 4 to 6, while Figs. 3.3e,f show axial mode orders from 1 to 3. It is clear that both axial and transverse dimensions merit careful consideration for helically-propagating modes. Thus, we here define the full notation specifying a mode as P_{mnr} where P is polarization, and m, n, and r are the azimuthal, axial, and radial mode order numbers, respectively. However, for the rest of this dissertation, we neglect higher-order radial modes as we find that they are harder to access and tend to have weaker properties. Thus, we refer to modes from here on using the notation P_{mn}. We note here that each azimuthal mode features higher-order axial mode degeneracies for which the transverse field pattern is identical, but the longitudinal field pattern changes according to its axial mode number n. For example, the axial modes in Figs. 3.3e,f share the same transverse field profile shown in Fig. 3.3d, but they are respectively the 1st and 3rd axial degeneracy of that 6th order azimuthal mode. In Fig. 3.4, a simulated spectrum of TM_{6n} modes shows that many resonance frequencies exist despite sharing the same transverse field pattern.

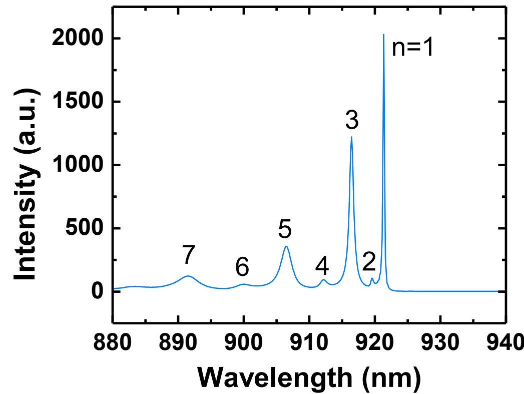

Figure 3.4 FDTD-simulated spectrum of TM_{6n} nanopillar modes. For each azimuthal mode number, several axial mode orders exist. The n=1-7 axial mode resonances are shown here for the TM_{6n} mode. The axial mode numbers associated with each peak are labeled. This sort of grouping of axial resonances exists for all azimuthal mode orders.

Able to confine light in small spaces, helically-propagating modes are well-suited for enabling small optical cavities. For nanopillars on silicon, the fundamental TM_{61} mode has the highest Q factor for TM_{6n} resonances (Q~4,300 for a 3 μm tall nanopillar with 660 nm diameter). Other higher order axial modes have comparable or sometimes higher Q values for TE resonances. TE resonances tend to have slightly lower quality factor (e.g. Q ~2,500 for TE_{51}), but have the advantage of stronger optical confinement. As seen in

Fig. 3.3, the fields of TE modes are confined more tightly within the InGaAs core compared to TM modes. Additionally, TE modes may better serve the goal of creating lasers using the nanopillars characterized in Section 2.3 since they showed stronger PL properties for TE polarized light.

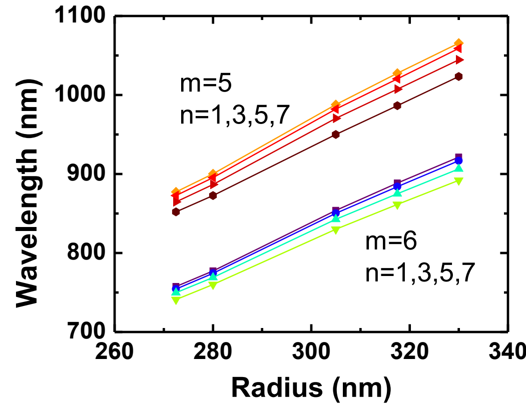

Figure 3.5 Resonance dependence on nanopillar radius. Helical modes of all orders and polarizations depend heavily of nanopillar radius as might be expected for whispering gallery-like modes.

By investigating how resonances depend on the radial dimension of nanopillars, we clearly see the WG aspect of helically-propagating modes. As shown in Fig. 3.5, even small decreases in nanopillar radius result in large shifts in resonant wavelengths. This is true for all helical modes of all polarizations, all azimuthal mode orders, and all axial mode orders. This behavior is also exactly what is expected of WG resonances. However, if we explore how resonances depend on the axial dimension, we gain a finer understanding of the nuances of helical modes. The dependence of resonances on nanopillar height is presented in Fig. 3.6. For the fundamental axial mode TM_{61}, the cavity resonance shifts little with change in nanopillar height. Since this fundamental degeneracy features little axial propagation, it behaves like traditional whispering gallery mode confined in the longitudinal direction. Thus, such behavior is expected. For progressively higher-order modes (n>1), dependence of cavity resonance on nanopillar height becomes progressively stronger. Physically, the helically-propagating modes are becoming more and more characteristic of Fabry-Perot modes. For more FP-like modes, the longitudinal dimension would of course matter more. The additional insight here is that the n=1 subset of helically-propagating modes is effectively what has been traditionally classified as the whispering gallery mode. Thus, WG modes can effectively be understood as a subset of the more general class of helically-propagating modes.

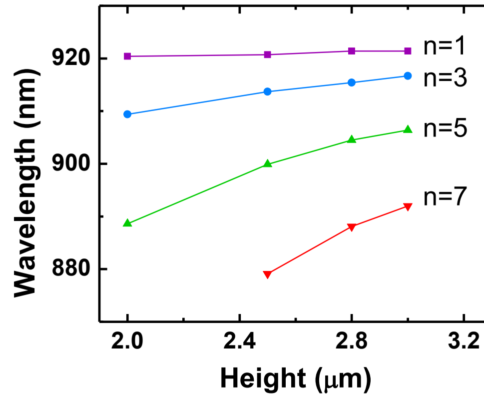

Figure 3.6 Cavity resonance versus nanopillar height. Simulated dependence of TM_{6n} resonances on nanopillar height. Notably, there is little dependence for the fundamental Fabry-Perot degeneracy (TM_{61}) since it behaves like a whispering gallery mode. Higher order modes show higher dependence on the axial dimension as they become more like Fabry-Perot modes in nature.

Here we will briefly expand on our earlier suggestion that the ray model interpretation of helical modes is incomplete. As shown in Fig. 3.7, these helically-propagating modes can be strongly supported even if a nanopillar grows on a substrate at a highly slanted angle. The ray model certainly breaks down in this case because ray incidence would not be shallow at all, yet clearly the modes remain well-confined. The simulation thus suggests that the boundary between silicon and InGaAs introduces a mode cutoff for helically-propagating modes. Full understanding of this cutoff requires additional investigation into its dependence on various factors like dimension, mode order, and frequency. However, it is known from other simulations not shown here that helical modes reflect even for zero refractive index contrast between nanopillar and substrate materials. Of course, also understanding effective and modal indices instead of only material indices will offer more insight.

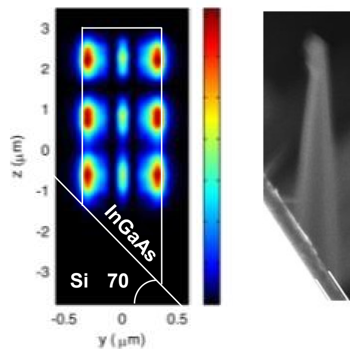

Figure 3.7 Mode cutoff of helical modes in nanopillars grown slanted on silicon. Helically-propagating modes are supported by nanopillars despite an

oblique interface between the InGaAs nanopillar and silicon. As shown, the field profile is not affected despite this oblique junction. The mode is strongly confined within the nanopillar even for slanted nanopillars on silicon. The oblique interface still introduces a mode cutoff that strongly reflects light just like in the case of nanopillars grown vertically from substrates.

Because helically-propagating modes exist even for nanopillars grown at oblique angles, we can experimentally image these modes along the axial dimension. Figure 3.8 shows these experimental results. For these measurements, nanopillars grown on polysilicon were used because its polycrystalline nature allows nanopillars to grow at a variety of angles with respect to the substrate normal. Optical micrographs are shown with and without a pump laser exciting photoluminescence (PL) from the nanopillars. A longpass filter was used to reject excitation light from reaching the imaging charge-coupled device (CCD). From the photoluminescence images, we can see the presence of emission maxima along the longitudinal axes of the imaged nanopillars. This provides experimental corroboration of the mode simulations previously discussed.

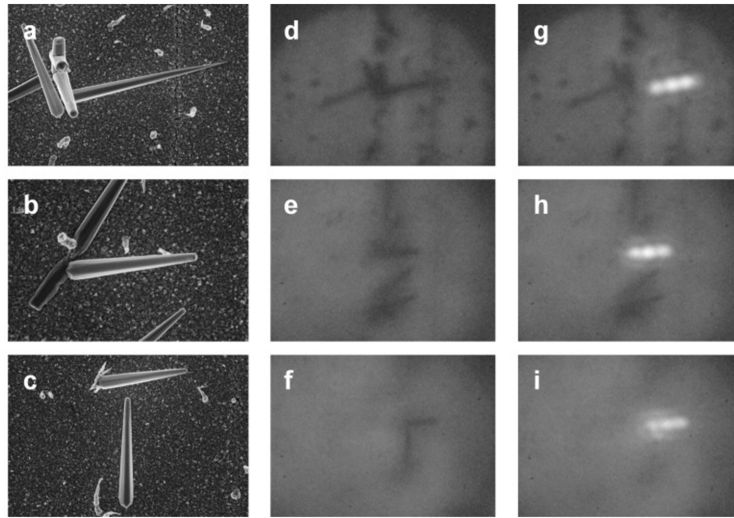

Figure 3.8 Imaging helically-propagating modes. Helically-propagating modes have been imaged from various nanopillars grown at oblique angles on polysilicon. Corresponding SEM images and optical micrographs are shown.

It is worthwhile to experimentally study the polarization properties of helical modes since TE and TM resonances both exist. In Fig. 3.9, a nanopillar's emission is imaged with polarizers passing either only TE or only TM light to the detector. Figure 3.9b shows three prominent maxima with TE polarization, while Fig. 3.9c shows only one TM maximum with comparable intensity to the TE modes. These results suggest that TE modes tend to dominate for nanopillars on silicon, which is sensible considering that

spontaneous emission from nanopillars also prefers that polarization. Thus, it should be far easier to excite TE modes than TM ones.

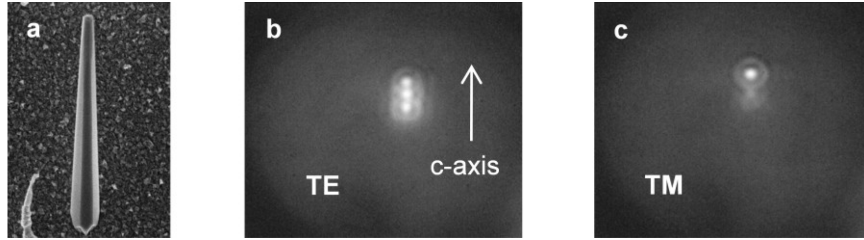

Figure 3.9 Polarization of helical modes. Measurements suggest that both TE and TM modes are excited experimentally, but TE modes are perhaps more dominant.

This section has thus far studied interesting optical modes that give rise to prominent resonances inside small semiconductor nanostructures on substrates. We saw that these modes feature not only longitudinal propagation, but also prominent radial as well as azimuthal behavior akin to WG modes. Physically then, these modes can be understood as helically-propagating. While unconventional, this phenomenon is nothing new. Similar effects have been long observed for skew rays in optical fibers and Mie scattering for nanoparticles [84], [85]. In the end, helically-propagating modes are simply a solution to the full wave equation in cylindrical coordinates, including both transverse and axial components.

Nonetheless, the exploration and application of these effects at the nanoscale level merits further research and will certainly yield novelty. In fact, these modes are perhaps best suited for nanoscale applications. Skew rays are not useful for carrying data signals over long communication links because of their high sidewall loss during propagation. On the other hand, a short nanopillar or nanowire with rotational symmetry integrated onto a substrate leverages the full value of helically-propagating modes. It could take advantage of these modes' ability to reflect from low-index contrast interfaces. At the same time, such nanostructures are often short enough such that helical modes' sidewall loss is acceptable over a full roundtrip. When combined, these two factors mean helical modes are perhaps better suited than any other mode for implementing nanoscale resonators. In the next chapter, we show how helically-propagating modes help enable nanolasers grown on silicon, which is a critical step towards the vision of integrated nano-optoelectronics advocated in this dissertation.

Chapter 4

Nanolasers on silicon

Photon generation is a critical optical function, and lasers are quite possibly better at it than any other device or mechanism. Since silicon (Si) is exceedingly poor at emitting light, integrating lasers onto silicon is one of the biggest goals and greatest challenges facing optoelectronic integration. Chapter 4 presents a promising pathway towards solving this challenge. Leveraging the nanopillars introduced in Chapter 2 and their natural helically-propagating resonances described in Chapter 3, we demonstrate that nanolasers can be grown directly on silicon wafers. With this capability, many applications become possible, and optical interconnects in particular stand to benefit.

Integration of optical interconnects with silicon-based electronics can address the growing limitations facing chip-scale data transport as microprocessors become progressively faster. However, material lattice mismatch and incompatible growth temperatures have fundamentally limited monolithic integration of lasers onto silicon substrates. In this chapter, we show how nanopillar growth overcomes these roadblocks to directly grow InGaAs nanopillar lasers on silicon, demonstrating the potency of bottom-up nano-optoelectronic integration. The helically-propagating cavity modes described in Chapter 3 are leveraged to strongly confine light within subwavelength nanopillars despite low refractive index contrast between InGaAs and silicon. These modes thereby provide an avenue for engineering on-chip nanophotonic devices such as lasers. Nanopillar lasers are as-grown on silicon, offer tiny footprints and scalability, and are thereby particularly suited to high-density optoelectronics. They may ultimately form the basis of the missing monolithic light sources needed to bridge the existing gap between photonic and electronic circuits.

4.1 Introduction

Since the first laser demonstrated that stimulated emission processes in an optical medium can implement a powerful, coherent light source [86], the field of photonics has witnessed an explosion of applications in telecommunications, lighting, displays, medicine and optical physics amongst others. Integration of photonic and electronic devices to leverage the advantages of both has subsequently attracted great interest. In particular, integration of optical interconnects onto silicon (Si) chips has become critical

as ongoing miniaturization of Si logic elements has incurred a bottleneck in inter- and intra-chip communications [13], [87]. Efforts towards creating on-chip light sources for optical interconnects have included engineering silicon and germanium for optical gain [34], [35], [38] and stimulated Raman scattering [88]–[90]. Concurrently, III-V lasers have been heterogeneously bonded onto silicon substrates [91]–[93]. However, numerous challenges face these approaches. Wafer bonding has low yield because of a stringent surface flatness requirement down to the atomic scale, while group IV emitters must overcome an indirect band gap that offers exceedingly inefficient radiation. Monolithic growth of high-performance III-V lasers on silicon thereby remains a "holy grail" for cost-effective, massively scalable, and streamlined fabrication of on-chip light sources.

The fundamental roadblock facing monolithic integration up to now has been a large mismatch of lattice constants and thermal expansion coefficients between III-V materials and silicon. While laser materials have previously been grown on silicon substrates, the high growth temperatures used would be detrimental to existing silicon electronic devices [18], [94]–[96]. In order to overcome these barriers, we recently demonstrated growth of single crystal GaAs nanoneedles on silicon at 400 °C under conditions compatible with complementary metal-oxide-semiconductor (CMOS) technology [53], [97]. Based on this template, we have now developed InGaAs/GaAs heterostructure nanopillar lasers that are monolithically integrated onto Si after a single growth step. Compatible with silicon technology, nanopillar lasers can potentially leverage the capabilities of today's massive silicon infrastructure to facilitate an ongoing paradigm shift in modern computing architecture towards optoelectronic circuitry. In addition, we show that the helically-propagating mode of Section 3.2 provides the unique feedback mechanism to enable on-chip laser oscillation. Whereas traditional Fabry-Perot (FP) modes are inhibited by the interface between InGaAs and Si, helical modes can strongly localize light within nanopillars of even subwavelength dimensions without lossy plasmonic or metal-optic effects. These modes thereby exemplify how novel optical phenomena in nanostructures can be used for future on-chip nanophotonic devices.

4.2 Nanolaser growth

The nanopillar-based laser is schematically depicted in Fig. 4.1a. Its cross-section reveals inner core-shell layers, while the inset offers a top view of the laser. The core contains the InGaAs active region while the GaAs shell provides surface passivation. Most nanopillars have a slight 5° taper between opposite sidewall facets. The height and diameter of the nanopillars scale easily and controllably with growth time despite the large lattice mismatch. Typical nanopillars possess tiny footprints of only ~0.34 μm^2, enabling them to realize high-density silicon-based optoelectronics. Nanopillars display extremely well-faceted geometry as shown by the scanning electron microscope (SEM) image in Fig. 4.1b. The top-view SEM image in Fig. 4.1c meanwhile shows the hexagonal cross-section of the nanopillar, which results from its unique single crystal wurtzite structure [98]. As we will later show, the as-grown nanopillar structure provides a natural optical cavity supporting the helically-propagating modes studied in Chapter 3. As such,

nanopillars do not require additional top-down processing to form on-chip optical cavities. Instead, they provide a viable bottom-up approach towards integrating light sources and resonators onto a silicon chip.

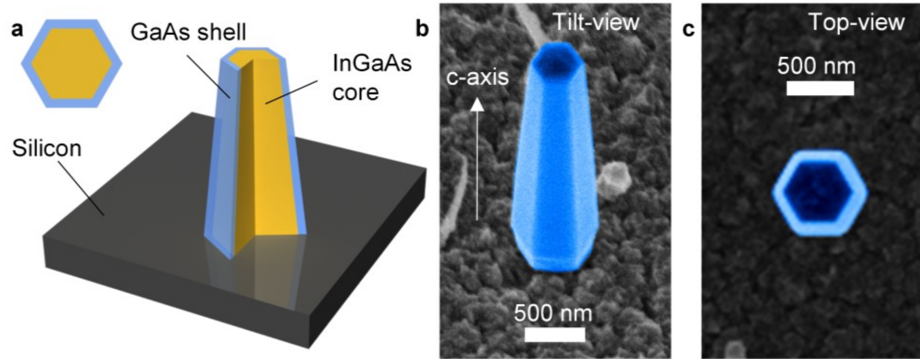

Figure 4.1 InGaAs/GaAs heterostructure nanopillar lasers monolithically grown on silicon. a, A schematic is shown for a nanopillar laser monolithically integrated onto silicon, illustrating its InGaAs core and GaAs shell. The higher band gap GaAs shell protects carriers from nonradiative surface recombination, which is critical for room temperature lasing. The inset shows a top-view schematic. **b,** An SEM image reveals the well-faceted geometry of the nanopillar optical cavity. This resonator structure forms naturally during growth, allowing lasers to be directly grown on silicon without additional processing. Nanopillar dimensions scale with growth time, enabling growth of effectively bulk high-quality III-V material on silicon. No critical dimensions have been observed for this novel lattice-mismatched growth mechanism. **c,** A top-view SEM image highlights the nanopillar's hexagonal wurtzite crystal structure. This hexagonal symmetry results in whispering gallery-like effects that we discuss later.

Importantly, nanopillars possess several critical advantages for optoelectronic integration onto silicon. They grow at a low temperature of 400 °C, which is drastically lower than typical III-V growth temperatures by 200-300 °C and is compatible with CMOS devices. Heterostructure nanopillar growth occurs spontaneously on a silicon substrate by metal-organic chemical vapor deposition (MOCVD) and is catalyst-free; thus, we avoid incorporating metal particles that are poisonous to Si CMOS devices. Additionally, core-shell layering allows nanopillar laser diode structures to be grown on silicon [99]. Detailed procedures are described in Section 2.3. Low temperature and catalyst-free growth allows nanopillars to be monolithically integrated with silicon electronics without compromising highly-developed Si transistor technology and CMOS process flows.

4.3 Laser oscillation on silicon

Room-temperature laser oscillation was achieved by optical excitation using a modelocked Ti:sapphire laser. 120 fs pump pulses from a modelocked Ti:sapphire laser (Coherent Mira, λ_{pump}=750 nm, repetition rate 76 MHz) were delivered by a 100x 0.7 numerical aperture objective (Mitutoyo NIR HR) to the sample at a temperature held between 4 K and 293 K by a continuous-flow liquid helium cryostat (Oxford Instruments Hi-Res II). The pump spot size was slightly defocused to ~6 μm in diameter. Nanopillar emission was collected by the same objective and relayed to a spectrometer and LN_2-cooled silicon charge-coupled device (Princeton Instruments SP2750 and Spec-10). Filters were used in all experiments to prevent pump light from reaching any detectors or cameras.

At low pump levels, nanopillars emit broad spontaneous emission. With increasing excitation intensity, a cavity mode emerges and ultimately laser oscillation is seen at ~950 nm, as shown in Fig. 4.2a. The inset shows the nanolaser light output power and emission spectral linewidth as functions of excitation (the former is referred to as the 'light-light' or 'L-L curve'). Clear threshold behavior is observed in the L-L curve along with prominent clamping of the laser linewidth. We observe another classic signature of lasing from near-field images of nanopillar lasers. When pumped below threshold, a nanopillar only outputs a spot of spontaneous emission as shown in Fig. 4.2b. Above threshold, clear speckle patterns due to interference of highly-coherent light become visible in Fig. 4.2c. Most lasers characterized show single mode operation, though as many as three lasing modes have been seen from a single nanopillar. Lasing on silicon at room temperature is a critical achievement demonstrating the potential of nanopillar lasers for implementing practical optoelectronics beyond the research lab.

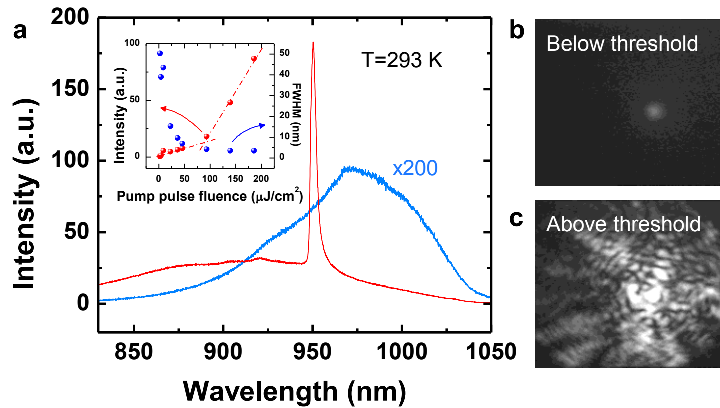

Figure 4.2 On-chip nanopillar laser oscillation. a, Room temperature nanopillar emission is shown below (blue) and above (red) threshold. The spectrum below threshold has been magnified 200x for visibility. The inset shows the L-L curve and linewidth clamping of the laser, revealing a threshold at ~93 μJ/cm^2. **b,** Camera images of nanopillar emission below threshold show only a spot of spontaneous emission. **c,** Upon lasing, strong speckle patterns

appear. Speckle results from the high degree of coherent emission and is a classic signature of laser oscillation.

We note that growing a sufficiently thick GaAs cap (~90 nm) is key for suppressing surface recombination to enable room temperature operation. Figure 4.3 highlights the dramatic impact of the GaAs shell for a InGaAs/GaAs heterostructure. Photoluminescence (PL) intensity from nanopillars increases drastically for thicker GaAs shells, though the benefit eventually saturates beyond a certain thickness. With a higher band gap, GaAs confines carriers within the InGaAs core and away from the nanopillar's surface, where many nonradiative states reside. Hence, the GaAs shell mitigates the impact of nonradiative recombination.

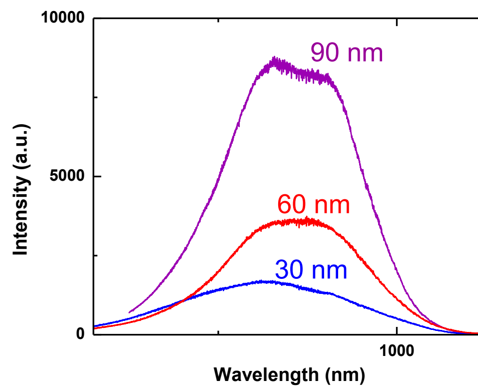

Figure 4.3 The role an outer GaAs shell. Thicker GaAs shells serve to confine carriers away from nonradiative states on the surfaces of nanopillars.

We perform additional experimental studies at 4 K to further characterize the nanopillar laser and extract various laser parameters. Figure 4.4 shows the L-L curve and the corresponding spectra below and above lasing threshold for a typical laser: a clear threshold is seen at a very low excitation intensity of ~22 μJ/cm^2. By constructing an analytical gain model using material parameters from literature [57], we analyze the nanopillar's spontaneous emission spectrum and establish a correlation between experimental pump levels and carrier density. Applying the gain model with classical rate equation analysis [100], [101], we fit the L-L curve in Fig. 4.4 to reveal a threshold gain and carrier density of ~1,400 cm^{-1} and ~1x10^{18} cm^{-3}, respectively. We thereby estimate a cavity quality (Q) factor of ~206 and a spontaneous emission factor of β~0.01, where β measures the fraction of spontaneous emission coupled into the cavity mode of interest. This value is reasonable considering the laser's small volume of 6x10^{-13} cm^3 [102]. We additionally measure a strong background suppression ratio of ~17-20 dB from typical lasing spectra. Nanopillar laser output peak powers have meanwhile been estimated to be as high as ~40 mW, though more analysis is needed given uncertainty about experimental

coupling losses and pulse transients. Additional details about laser analysis and relevant methodologies will be discussed in Section 4.6.

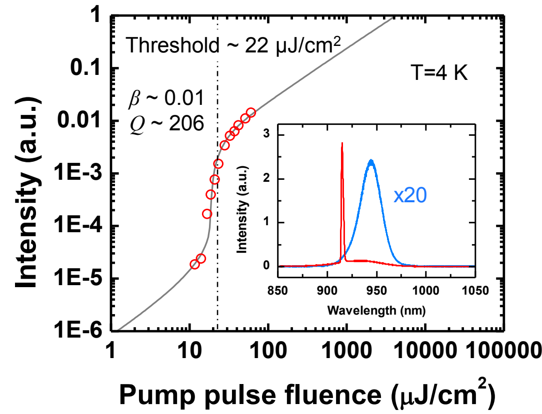

Figure 4.4 L-I curve of a nanopillar laser. The L-L curve of a nanopillar laser operating at 4 K with a low threshold of ~22 μJ/cm^2 is analyzed to extract estimated values of Q~206 and β~0.01. The inset shows spectra of the nanopillar laser both below (blue, magnified 20x) and above (red) threshold. The laser peak clearly dominates above threshold, achieving a 17 dB background suppression ratio.

In characterizing lasers, it is useful to look beyond the spectral domain and observe how they behave in the time domain. Claims of laser oscillation are often dubious if L-L curves provide the only evidence because threshold behavior is observed for many natural phenomena. Even linewidth narrowing and dominant spectral peaks may not always supply sufficient proof, especially for high Q lasers where linewidths are narrow even well below threshold. In Fig. 4.5, we show normalized time-resolved PL curves from a nanopillar laser below and above threshold. Figure 4.5a clearly shows that lasing nanopillars emit light at a highly enhanced rate in comparison to nanopillars below threshold. After all, stimulated emission processes are faster than spontaneous emission processes. In fact, the 49 ps lifetime shown is resolution-limited, and it is expected that the true nanopillar laser emission lifetime is closer to 1 ps. Below threshold, a much slower PL decay time constant of 325 ps is observed. Figure 4.5b shows the spectra corresponding to time-resolved PL curves with arrows denoting the center wavelengths used for time-resolved measurements.

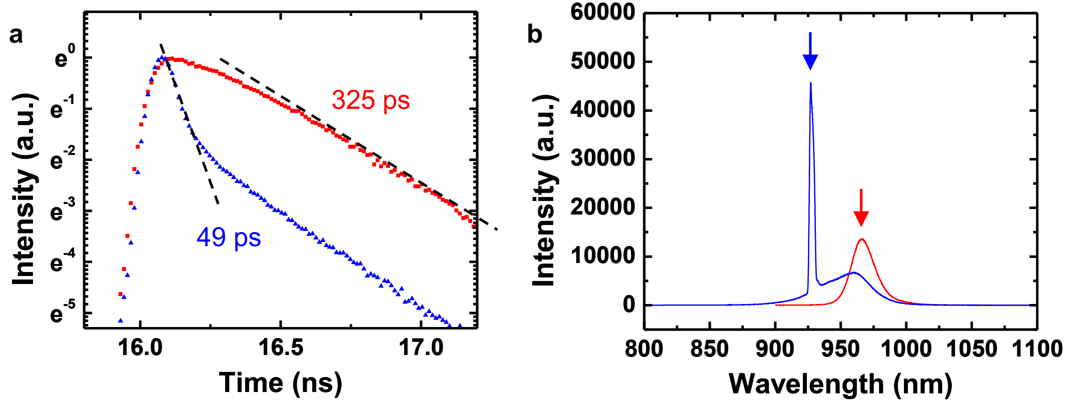

Figure 4.5 Time-resolved photoluminescence of nanopillar lasers. a, Below threshold, a relatively slow decay exists. Above threshold, radiative recombination accelerates greatly as stimulated emission processes take over. The 49 ps time constant shown is limited by the resolution of the system. The long tail in the above-threshold curve arises from the natural response of the photodetector used. **b,** The spectra corresponding to the decay curves in **a** with arrows marking the center wavelengths detected.

While a major thrust of this dissertation is the integration of optoelectronic devices like lasers onto silicon, another is the miniaturization of photonics to better match the nanoscale dimensionality of electronics. Above, we show how a unique growth mechanism allows small lasers to integrate onto silicon in a CMOS-compatible manner. Now we briefly touch on just how small these lasers can be. Figure 4.6 offers some indication. It presents lasing spectra for a nanolaser with subwavelength physical dimensions on all three sides. The physical volume of this laser is only $V \sim 0.2\lambda_o^3$, where λ_o is the lasing wavelength in air. Given that no post-growth processing was required for lasing, this suggests that some sort of natural feedback mechanism within nanopillars bestows them with powerful light trapping abilities. This feedback mechanism is in fact the helically-propagating mode of Section 3.2. In the next section, we revisit these modes in the context of experimental lasing results.

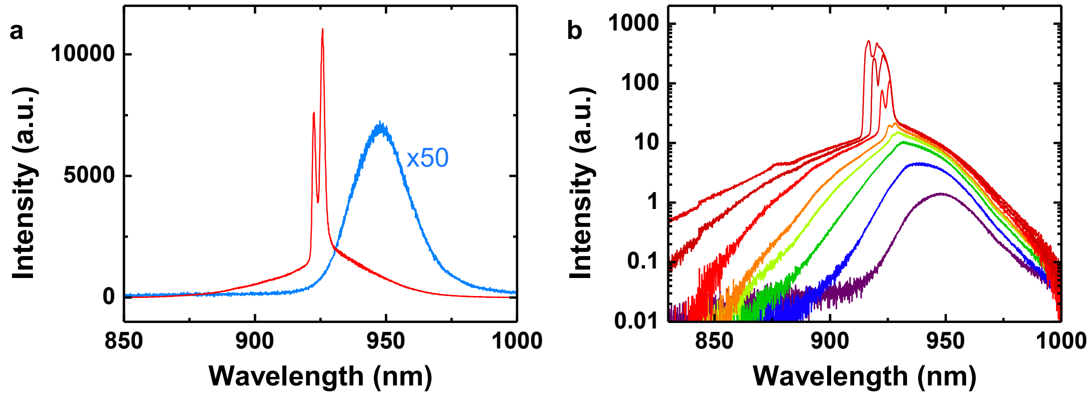

Figure 4.6 Subwavelength laser spectra. a, Emission spectra below (blue) and above (red) threshold from a nanopillar that is subwavelength in volume and on all sides. The below threshold curve has been multiplied by 50 for visibility. **b,** The power-dependent evolution of lasing spectra is shown for the same laser on a log scale as a reference. Measurements for this device were performed at T=4 K. This set of spectra corresponds to the laser shown in Fig. 4.7e.

4.4 Helically-propagating modes

Despite minimal index contrast between the InGaAs nanopillar (n_r~3.7) and the Si substrate it resides on (n_r~3.6), sufficient optical feedback or Q is attained for laser oscillation in nanopillar structures. Even non-negligible absorption by silicon at nanopillar laser wavelengths is overcome. Intuitively, helically-propagating modes can have nearly total internal reflection at the nanopillar-Si interface because their wavevectors strike that boundary with grazing incidence at extremely shallow angles. Figure 4.7a illustrates this concept using a ray optics interpretation. Alternatively, the interface between substrate and nanopillar can be thought of as introducing a strong cutoff for helically-propagating modes. The strong feedback of helical modes is further confirmed by finite-difference time-domain (FDTD) calculations of untapered nanopillars. These helical nanopillar modes possess strong azimuthal components, which result in transverse field profiles similar to those previously reported for hexagonal whispering gallery (WG) modes [82], [103], [104] as shown in Fig. 4.7b. However, unlike traditional WG modes, helical nanopillar resonances have net propagation in the axial direction. This can be seen from the first and third order axial standing wave patterns shown in Figs. 4.7c and 4.7d, respectively.

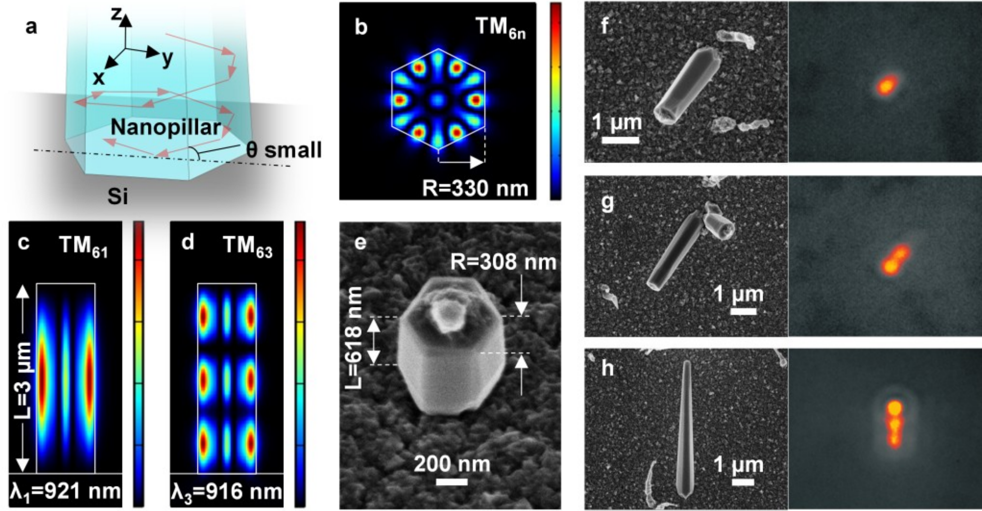

Figure 4.7 Helically-propagating modes for optical feedback of on-chip nanolasers. a, A schematic depicts how a helical ray path enables reflection from a low-index contrast interface due to glancing angle incidence, lending physical insight into the mechanism behind strong optical confinement in on-chip nanopillars. **b,** An FDTD-simulated field profile shows a hexagonal WG-like mode pattern (TM_{6n}) in the transverse plane, which arises from strong azimuthal components of helical modes. Such modes have net propagation along the nanopillar axis and build axial standing wave patterns. The first-order standing wave is shown in **c** while a higher-order one is shown in **d**. **e,** Strong light localization provided by helical modes enables nanolasers that are subwavelength on all sides. An SEM image shows such a subwavelength device. **f-h,** Experimental images of nanopillar emission show standing wave patterns along the nanopillar axes, corroborating helical mode propagation. SEM photos of the nanopillars imaged are shown.

We can therefore define two mode numbers to describe these helically-propagating modes. An azimuthal mode number *m* describes the transverse field pattern just as it does for WG modes, while an axial mode number *n* describes the order of the axial standing wave like for FP resonances. To be complete, a third mode number should account for higher-order radial modes, but we find that the subwavelength transverse dimensions of nanopillars limit access to only the lowest-order radial mode. Both transverse electric (TE) as well as transverse magnetic (TM) polarizations exist. Previous photoluminescence studies indicate that material gain is stronger for electric field polarized perpendicular to the wurtzite nanopillar axis, suggesting TE modes may be preferred for lasing [105]. In this dissertation, we refer to specific resonances as either TE_{mn} or TM_{mn} for consistency. As might be expected, modes with distinct mode numbers resonate at distinct wavelengths (e.g. λ_1=921 nm for TM_{61} and λ_3=916 nm for TM_{63}). Both nanopillar radius and length determine cavity resonances, further substantiating the helical nature of nanopillar cavity modes. Traditional WG resonances are meanwhile

relatively insensitive to the axial dimension. In our description, they can actually be interpreted as the n=1 subset of helically-propagating modes. We find that most nanopillars lase between 890-930 nm when the nanopillar radius is varied between 270 nm to 340 nm. This range corresponds to TM_{5n}, TM_{6n}, TE_{4n} and TE_{5n} resonances, which are among the lowest-order azimuthal modes reported to have achieved laser oscillation. Additional discussion and details of FDTD calculations and results can be found in Section 3.2.

The most important consequence of a helically propagating mode is that it allows high reflectivity at a dielectric interface with low index contrast. From Figs. 4.7c and 4.7d, it is evident that the cavity modes are remarkably well-confined in the active material despite the significant interface with silicon. Such strong confinement enables our resonators to lase without having to fabricate the pedestals that WG microdisk lasers typically require to preserve vertical optical confinement. In fact, the confinement is strong enough that even nanopillars with subwavelength dimensions on all sides achieve laser oscillation. An SEM image of such a subwavelength laser is shown in Fig. 4.7e. The lasing and spontaneous emission spectra for this laser at T=4 K is shown above in Fig. 4.6. Subwavelength lasers have meanwhile been successfully implemented on other substrates by use of plasmonics [72], [106], [107]. In our case, a purely semiconductor cavity mode alone provides enough confinement for subwavelength lasing without metal-optic effects [77], [78]. Avoiding metal losses is a critical advantage that should allow high-efficiency laser operation.

Engineering these helical modes by controlling nanopillar dimensions, we can select the mode number to be used for laser oscillation and control the wavelength of nanopillar laser emission. Since nanopillar cavities scale with growth time from the nanoscale throughout the microscale without critical dimensions, we can easily grow nanopillars to resonate at any wavelength of choice. Experimentally, we verify that nanopillars support n>1 resonances by directly imaging emission from nanopillars of different lengths as presented in Figs. 4.7f-h with corresponding SEM images. For these measurements, we used nanopillars that are grown at oblique angles with respect to the surface normal of the substrate, allowing us to image emission along the nanopillar axes. Axial standing wave patterns can be clearly discerned, confirming net propagation of nanopillar cavity modes along the nanopillar axis. As nanopillar length decreases, higher-order axial modes are cut off such that fewer axial maxima can be observed. Nanopillars are held below threshold for these images to prevent speckle interference from obscuring the mode pattern. Traditional FP modes cannot account for the patterns seen since light leakage through the InGaAs-silicon interface is far too severe for such modes. Instead, we attribute the axial maxima to helically-propagating modes of the nanopillar, which simulations show to be strongly supported despite even oblique junctions of low index contrast between nanopillars and substrate (see Section 3.2).

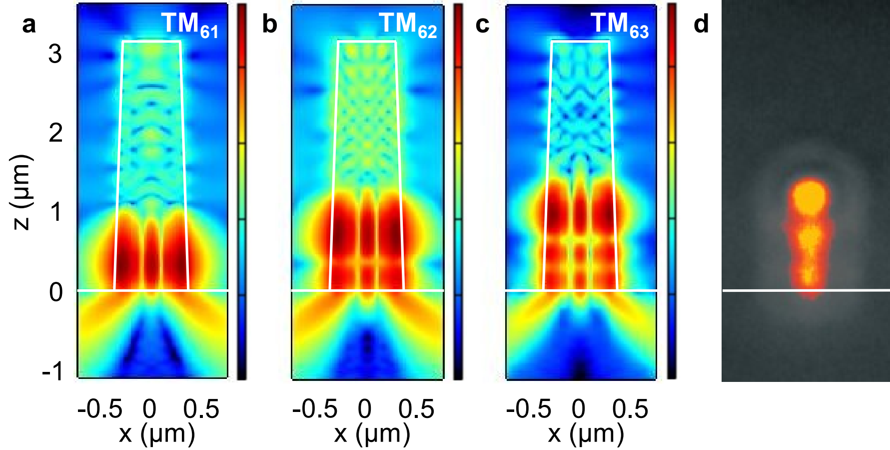

Figure 4.8 Effects of nanopillar sidewall taper on optical modes. Vertical field profiles are shown of a nanopillar on Si with 5° taper for **a,** TM_{61}, **b,** TM_{62} and **c,** TM_{63} modes. The profiles here are plotted on log scale for clarity. The transverse field profiles are identical to that in Fig. 4.7b. Sidewall tapering results in increased light leakage, which decreases the quality factors of helical resonances to ~170-300. The smaller radius on the upper part of the pillar also introduces a mode cut-off such that helical modes are confined towards the base of tapered nanopillars. Furthermore, tapering blueshifts helical resonances. **d,** Experimental results confirm the aforementioned effects of tapering on helical modes.

We remark here that our experimental Q (~206) falls well short of theoretical estimates (e.g. ~4,300 for TM_{61}), likely because tapering in the nanopillar perturbs the mode. To investigate the effects of the sidewall taper, additional FDTD simulations are performed for nanopillars on silicon with 5° angles between opposite sidewalls. It should be noted that while 5° is a well-represented average, the range of taper angles can be from <3° to ~7°. Figure 4.8 shows vertical field profiles for TM_{61}, TM_{62} and TM_{63} modes, revealing the rather pronounced effects of tapering. The modes are noticeably confined towards the base of the nanopillar. At a certain height, the reduced nanopillar radius cuts off the mode in the vertical direction and reflects it downwards. The taper also blueshifts helical resonances, e.g. ~37 nm blueshift for the TM_{61} mode, since the transverse dimensions become effectively smaller. Additionally, the adiabatic reduction of nanopillar radius causes helical modes to become less resonant as they propagate upwards, resulting in increased light leakage through the cavity sidewalls. Figure 4.8d shows experimental data to corroborate these conjectures about the effects of tapering on helical resonances. For TM_{61}, TM_{62} and TM_{63} modes, the Q factors are 319, 235 and 173, respectively. While much smaller than Q's for straight nanopillars, these values agree extremely well with our experimental data, confirming that sidewall taper is the primary loss mechanism for our as-grown cavities. Engineering the taper angle thus offers an avenue to improve future laser performance. We briefly note that higher-order axial modes generally have lower quality factors. Physically, the stronger Fabry-Perot

characteristic of higher-order axial modes means that their effective longitudinal wavevector components become stronger, causing larger penetration and loss into the substrate.

To better understand the characteristics of nanopillar cavity modes, simulations are performed for nanopillars of various dimensions. Figure 4.9 shows the dependence of cavity resonances on nanopillar radius, including the effects of nanopillar sidewall taper. Calculations are presented for TM_{5n}, TM_{6n}, TE_{4n} and TE_{5n} resonances. From Fig. 4.9, we see that resonances shift quite drastically versus nanopillar radius, which attests to the strong azimuthal components of the mode. As shown, simulated TM_{5n}, TM_{6n}, TE_{4n} and TE_{5n} resonances overlap our experimental lasing wavelengths very well. We thereby attribute the lasing peaks we observe to these modes.

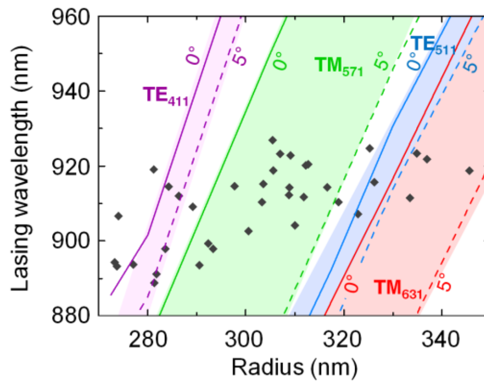

Figure 4.9 Cavity resonance versus nanopillar radius. Dependence on nanopillar radius of TE_{41}, TE_{51}, TM_{57} and TM_{63} resonances is shown. Ranges of resonances are displayed to account for the effects of sidewall taper (0-5°) on cavity wavelengths. Gray diamonds denote experimental lasing wavelengths of nanopillars of various radii. The experimental data is well within the range of modes simulated, suggesting that TE_{4n}, TE_{5n}, TM_{5n} and TM_{6n} modes provide optical feedback for our lasers. Ultimately, the laser wavelength range is between 890-930 nm, limited by the InGaAs gain region.

4.5 Wavelength control of laser emission

By varying the indium composition of nanopillars during growth, we can spectrally match the semiconductor gain to designed cavity resonances to maximize spontaneous emission coupling into the cavity modes (see Section 2.3.2) [108]–[110]. In this current study, we vary indium composition from 12-20% to achieve wavelength control of on-chip nanolasers over a ~50 nm range as shown in Fig. 4.1. The flexibility of wavelength control may allow nanopillars to fulfill a myriad of laser applications throughout the near-infrared. For chip-scale Si photonics applications, Si-transparent laser light may be favorable to avoid absorption loss in Si waveguides, although this is not required if

transparent silica waveguides are used instead [111], [112]. In the latter scenario, low-cost high-performance Si photodetectors may then be used to complete the optical link. Nonetheless, we expect to be able to push nanopillar laser emission beyond silicon transparency, which would also improve cavity Q by removing absorption loss into the substrate. Past nanopillar growth studies have already demonstrated Si-transparent nanopillar photoluminescence, indicating that a fundamental limitation does not exist for longer wavelength lasers [97]. The fact that we grow laser cavities using a bottom-up approach rather than top-down etching processes raises a couple additional points of interest. First, single crystal growth provides facets that are far smoother than etching can allow, thereby minimizing scattering loss. Additionally, the hexagonal structure of nanopillars is dictated by their hexagonal wurtzite crystal lattice. Thus, as-grown nanopillars have unprecedented symmetry, which prevents polarization splitting of degenerate laser modes often seen in microdisks due to ellipticity. Instead, truly single mode laser oscillation can be achieved.

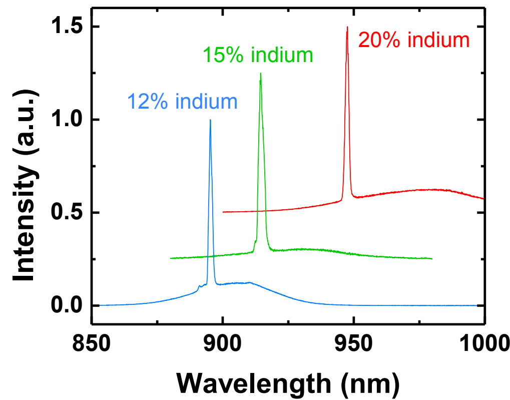

Figure 4.10 Wavelength control of nanopillar lasers by composition variation. Nanopillar lasers can be implemented over a broad range of wavelengths by properly tuning indium composition and nanopillar dimensions. Nanopillars are grown to target dimensions designed to achieve resonances at specified wavelengths. Indium composition of the InGaAs core is concurrently adjusted so that nanopillar gain and emission spectrally match the resonant wavelength for laser oscillation. The spectra shown are offset for clarity. In this study, a change in indium composition from approximately 12-20% provides a 50 nm control in the output laser wavelength.

4.6 Waveguide coupling

Waveguide coupling of nanolasers is important for many applications. Figure 4.11 shows the side-view far-field pattern for the TM_{61} mode of a nanopillar laser on silicon. From the polar profile, the helical mode behavior is evident since radiation occurs from the top (Θ=90°), bottom (Θ =270°), and sides (Θ =0° and 180°) of the pillar. Note that the side emission dominates by far. The vertical emission from the top and bottom facets are

~10,000 and ~30 times weaker, respectively. Thus, the emission characteristics of nanopillar lasers are highly similar to those of microdisks and ring resonators, for which waveguide coupling can be achieved easily with a closely-spaced waveguide [92], [113]. This technique can be leveraged and applied to the nanopillar lasers.

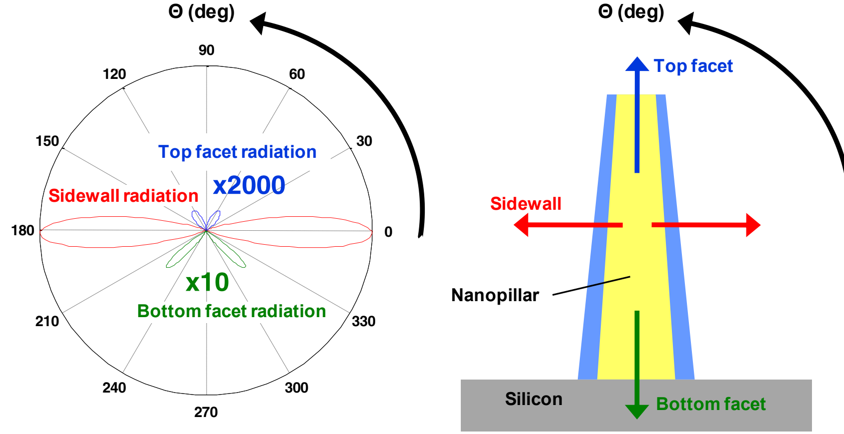

Figure 4.11 Side-view far-field pattern for TM_{61} mode of a nanopillar resonator on silicon. The profile shows the dominance of radial emission for nanopillar lasers, much akin to whispering gallery modes in microdisks and ring resonators. The upwards (blue) and downwards (green) radiation patterns have been magnified 2000x and 10x, respectively.

4.7 Laser modeling

Knowledge comes with not only aggregation of data, but also careful analysis of collected information. Whereas the previous section presented experimental results for nanopillar lasers on silicon, this section will focus on the modeling performed to analyze those results. We start first with modeling the gain provided by InGaAs nanopillars. Rate equation analysis is then done to model how gain and optical cavity interact to create both stimulated and spontaneous emission. Finally, some unexpected experimental data is explained to be the result of gain switching.

4.7.1 Gain modeling

In order to analyze experimental results and estimate the properties of the nanopillar laser, a gain model is first constructed following analytical treatment from ref. [57]. Starting from Fermi's golden rule to model photon generation by electron-hole recombination, a material gain spectrum can be derived as

$$g(\hbar\omega) = \frac{\pi e^2}{n_r c \varepsilon_0 m_0^2 \omega} |M|^2 \int_0^\infty \rho_r (f_c - f_v) \frac{\hbar / \pi\tau_{in}}{(E_g + E - \hbar\omega)^2 + (\hbar / \tau_{in})^2} dE \quad (4.1)$$

where n_r, c, ε_0, m_0, and ω are material refractive index, vacuum speed of light, vacuum permittivity, electron mass, and radial frequency of the electronic transition, respectively. M describes the strength of the transition and is calculated from the momentum matrix element under the long wavelength (dipole) approximation. f_c and f_v are the Fermi distribution functions for electrons and holes, respectively. ρ_r is the reduced density of electronic states in a material. Because nanopillar dimensions are much larger than the de Broglie wavelengths of electrons and holes, quantization effects are not seen, and a 3-dimensional reduced density of states is used:

$$\rho_r = \frac{1}{2\pi^2}\left(\frac{2m_r}{\hbar^2}\right)^{3/2}\sqrt{\hbar\omega - E_g} \tag{4.2}$$

E_g is the band gap of the semiconductor, and $\hbar$ is the reduced Planck constant. m_r is the reduced effective mass, which is directly related to hole and electron effective masses in a semiconductor.

The equation for gain presented above accounts for intraband relaxation (scattering) effects that cannot be ignored in real-world experiments. This is done through convolution of an unbroadened gain spectrum with a Lorentzian lineshape function characterized by τ_{in}. τ_{in} is the intraband scattering lifetime of carriers, which is often treated as a fitting parameter and has a typical value of ~0.1 ps. We estimate τ_{in} in our material and thereby the amount of broadening in the gain model by fitting experimental photoluminescence (PL) spectra as shown in Fig. 4.12. The analytical spontaneous emission spectrum used for fitting is generated by using the gain expression from (4.1) and following traditional Einstein's AB coefficients treatment:

$$r_{sp}(\hbar\omega) = \frac{2n_r e^2\omega}{hc^3\varepsilon_0 m_0^2}|M|^2\int_0^\infty \rho_r f_c(1-f_v)\frac{\hbar/\pi\tau_{in}}{(E_g + E - \hbar\omega)^2 + (\hbar/\tau_{in})^2}dE \tag{4.3}$$

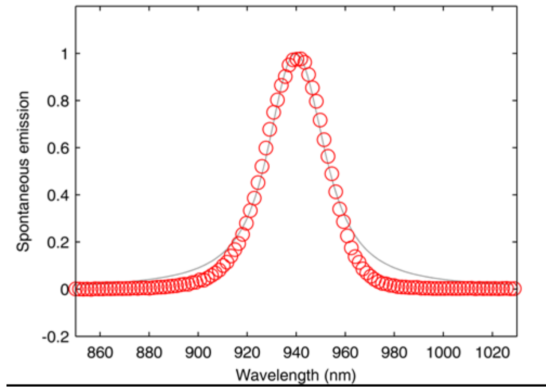

Figure 4.12 Fitting spontaneous emission spectrum. The experimental spontaneous emission spectrum (red circles) below theshold is fitted by the theoretical spectrum (grey line) calculated using τ_{in}=40 fs. Only every 30th point of the experimental spectrum is plotted to more clearly show the fit. The fit overestimates the emission tails, which is a well-known problem with Lorentzian lineshape broadening methods.

Intraband relaxation depends on the type of carrier excitation, so spectra generated by 120 fs Ti-sapphire pulses below threshold are used for fitting. We neglect pump-dependence of the relaxation times here and assume a constant value for τ_{in}. A lifetime of τ_{in}~40 fs is found, which agrees well with values previously reported for GaAs under femtosecond excitation[114]. Using this value and typical material parameters found from literature as tabulated in **Table 4.1**, gain spectra can be generated for various carrier densities as shown in 4.13. The gain spectra shown are similar to typical GaAs material gain spectra, though we note that our spectra show a sharper transition from gain to absorption at higher energies. This results from minimized thermal broadening since our calculations are for T=4 K, the temperature at which our fitting experiments are performed. At this low temperature, the Fermi distribution functions exhibit sharp transitions, explaining this behaviour. The decrease in thermal broadening also results in larger peak gain values for a given carrier density at 4 K versus at room temperature.

Material parameters for $In_{0.15}Ga_{0.85}As$	
m_e^*	$0.062m_0$ kg
m_h^*	$0.5m_0$ kg
m_r^*	$0.055m_0$ kg
E_p $\left(\lvert M\rvert^2 = \frac{m_0 E_p}{6}\right)$	25.18 eV
E_g	1.306 eV
τ_{in}	40 fs
n_r	3.7

Table 4.1 Material parameters for gain modeling.

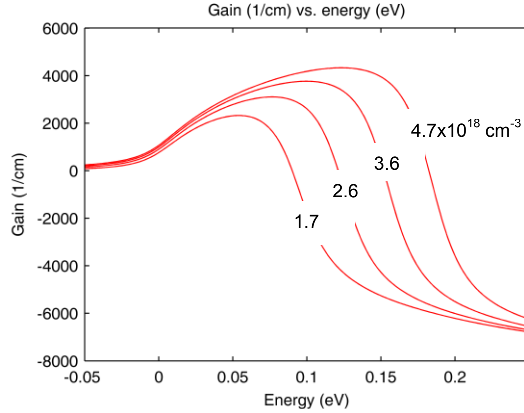

Figure 4.13 Gain spectra at T=4 K. Calculated gain spectra for different carrier densities based on spontaneous emission data and material parameters from literature. The gain is plotted versus energy from the band edge. The gain has been calculated for a temperature of 4 K since most experiments are performed at cryogenic temperatures in a cryostat

Able to generate gain spectra, we thus calculate the maximum gain versus carrier density as shown in Fig. 4.14. Using parameters $N_{tr} = 3 \times 10^{17}$ cm^{-3}, $N_s = 4 \times 10^{17}$ cm^{-3}, and $g_0 = 2{,}200$ cm^{-1}, we fit the curve in Fig. 4.14 to build a logarithmic gain model of the form:

$$g(N) = g_0 \ln\left(\frac{N + N_s}{N_{tr} + N_s}\right) \tag{4.4}$$

This gain model simplifies the numerical rate equation analysis we perform later.

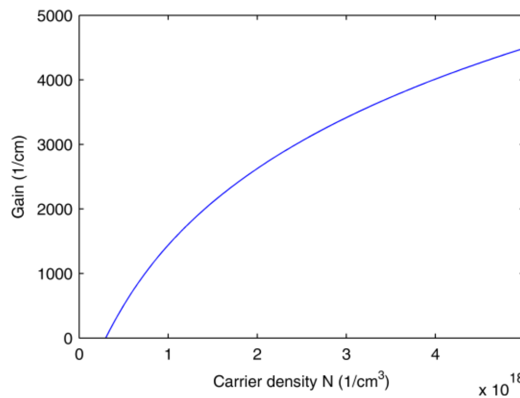

Figure 4.14 Gain model. Logarithmic material gain model, which we use with traditional rate equations for further laser analysis.

Importantly, fitting the spontaneous emission allows us to estimate the carrier density generated by an experimental pump level since shape and peak of PL spectra primarily depend on the amount of carriers filling the energy band. As a result, we are able to fit experimental curves of laser light output versus pump level (L-L curve) by rate equation analysis using absolute values on the horizontal axis (pump level). This then allows us to estimate the cavity loss of the system and thereby the cavity Q factor. We believe other methods such as measuring the cavity linewidth below threshold are more prone to error since the linewidth only represents cold cavity Q exactly at carrier transparency. For high-Q cavities, this is far less of an issue; however, our current Q factors are relatively modest such that absorption loss or gain drastically affects linewidth values. By our calculations from the PL fitting, ~2.5% of the incident pump contributes to generating carriers in the nanopillar. This agrees well with an FDTD-simulated absorption of ~3% of the pump light by the nanopillar.

4.7.2 Rate equation analysis

Following treatment from ref. [100], we apply traditional laser rate equations to further analyze experimental data and extract estimates for Q factor and β, where β is the spontaneous emission coupling factor. Physically, β describes the amount of spontaneous emission that couples into the laser cavity mode. The rate equations have been slightly modified from the reference to take optical pumping rather than electrical injection into account. The rate equations are as follows:

$$\frac{dN}{dt} = \frac{\eta_a P}{h\nu V} - AN - \frac{N}{\tau_{sp}} - CN^3 - \nu_g g S \tag{4.5}$$

$$\frac{dS}{dt} = \left[\Gamma \nu_g g - \frac{1}{\tau_p}\right] S + \Gamma\beta \frac{N}{\tau_{sp}} \tag{4.6}$$

N and S are carrier density and photon density in the cavity mode, respectively. P is the optical pump used for exciting nanopillar laser emission and is time-dependent of the form $P_p sech^2 \ \frac{1.76t}{\Delta t}$. P_p is the peak power of the pulse and Δt is the pulse width, which is 120 fs in this case. η_a is the fraction of the pump light that generates carriers in the nanopillar and is 2.5% per earlier discussion, and V is volume. A, τ_{sp}, and C are the nonradiative recombination coefficient, spontaneous emission lifetime, and Auger recombination coefficient, respectively. $v_g(\frac{c}{n_g})$, τ_p, and Γ are group velocity, photon lifetime, and confinement factor, respectively. Values used are tabulated in **Table 4.2**. Here we assume $\Gamma = 1$ since we have a bulk active region and simulations show strong confinement of the optical mode inside the nanopillar. Using $\Gamma = 1$ also allows us to make our estimate of Q factor a lower bound.

Rate equation parameters	
A	1.43×10^{8} s^{-1}
τ_{sp}	4 ns
C	3.5×10^{-30} cm^{6}-s
n_g	4.2
Γ	1

Table 4.2 Parameters for rate equation analysis.

Numerically solving differential equations (4.5) and (4.6) for the transient behavior of the carrier and photon densities, we can construct L-L curves to fit the experimental data. We note that temporal analysis with the rate equations must be used and steady-state analysis does not apply given the femtosecond pumping used in experiment. This fact is highlighted by gain switching effects seen for strong femtosecond pumping as elaborated in the next section. We treat β and g_{th} (threshold gain) as fitting parameters where $g_{th} = \alpha_i + \alpha_m = \alpha_c$. α_i, α_m, and α_c are internal loss, mirror loss and total cavity loss, respectively. The threshold gain is related to Q factor through

$$Q = \frac{2\pi}{\lambda} \frac{n_g}{\Gamma g_{th}} \tag{4.7}$$

As shown in Fig. 4.15, β and Q are found from fitting since they affect two distinct characteristics of the L-L curve. Q mainly determines the threshold pump level in the case when fitting absolute units rather than arbitrary units for pump level (horizontal axis) can be done. Meanwhile, β determines the increase in cavity photon density from below to above threshold. In other words, a smaller β value results in a more pronounced "knee" in the L-L curve. The possibility of thresholdless lasing based on high β and also the Purcell effect has been of great interest in recent years [102], [115]–[117].

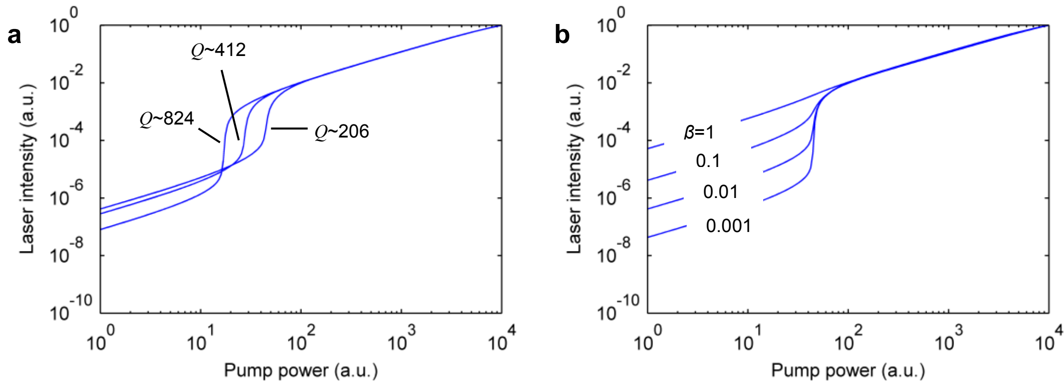

Figure 4.15 Rate equation fitting. a, Different Q's primarily affect threshold values and thus horizontally shift the L-L curve. Able to correlate carrier densities to experimental pump levels, we can therefore estimate Q from rate equation fitting. **b,** Varying β meanwhile allows fitting of the pronunciation of the "knee" in the L-L curve around threshold.

The fitting procedure first involves adjusting g_{th} and therefore Q in the model until the calculated L-L "knee" lines up horizontally with experimental data. The laser intensity (vertical axis) is scaled arbitrarily since it is uncertain how much nanopillar laser emission is actually collected in experiments, but this does not affect Q or β. Then, β is adjusted until the size of the "knee" matches what is seen experimentally. Based on this analysis, a Q~206 and β~0.01 are estimated as presented in Section 4.3. The β value is relatively large, which is expected given the small volume of the nanopillar cavity. Its small size makes its characteristics akin to many other microcavities and nanoscale lasers reported in literature with soft thresholds [72], [101], [106], [118].

4.7.3 Gain switching

By performing temporal analysis using rate equations, we are able to generate the transient responses of carrier and photon densities to a femtosecond pump source. We immediately see from Fig. 4.16 that gain switching occurs because of ultrafast excitation. By generating a large amount of carriers at a very short time scale, femtosecond pump pulses excite carrier densities significantly above threshold, resulting in a strong spike of stimulated emission, which is akin the first spike seen for relaxation oscillation effects. As a result, nanopillar lasers output laser pulses as the carrier density quickly drops below threshold after this initial spike.

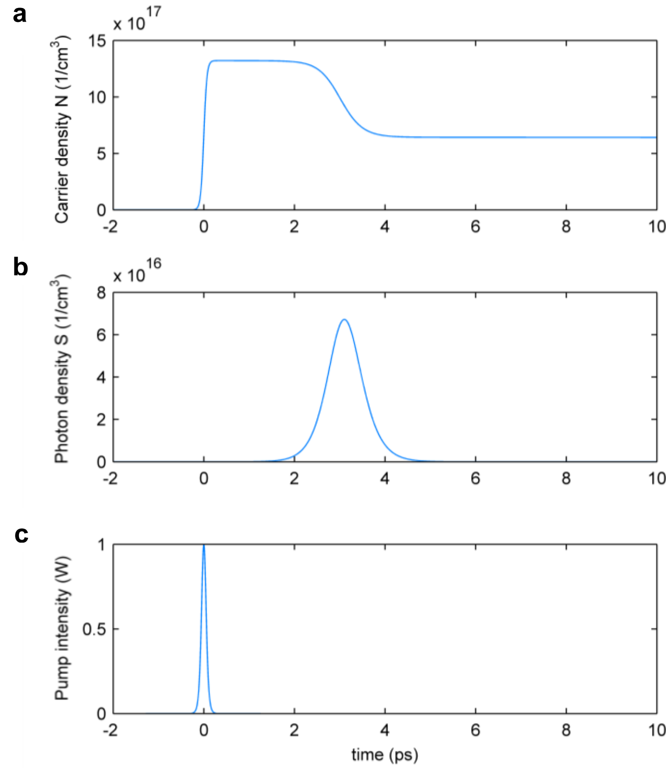

Figure 4.16 Modeled nanopillar transient response under ultrafast pulse excitation. a, Femtosecond pulses generate carrier densities far above threshold, which quickly drop below threshold upon the nanopillar emitting a laser pulse as shown in **b**. Spontaneous emission takes over below threshold, though it is much weaker than the pulse of stimulated light. **c,** The femtosecond excitation pulse plotted as a reference.

Interestingly, under progressively higher pump powers after the onset of lasing, the spontaneous emission tail progressively decreases as shown in Fig. 4.17a. This effect is attributed to the gain switching mechanism previously described. Under higher pump levels, gain switching becomes more pronounced and stimulated emission processes in the nanopillar more drastically drain the carrier density (Fig. 4.17b). Increase in gain switching thereby also results in an increase in the amount that the carrier density drops below threshold after the initial spike of nanopillar laser emission. These lower carrier densities after this initial spike thus correlate to reduced spontaneous emission under higher pump levels, which we experimentally see in Figs. 4.17c,d below. Thus, we sometimes observe spontaneous emission reduction instead of clamping in our lasers.

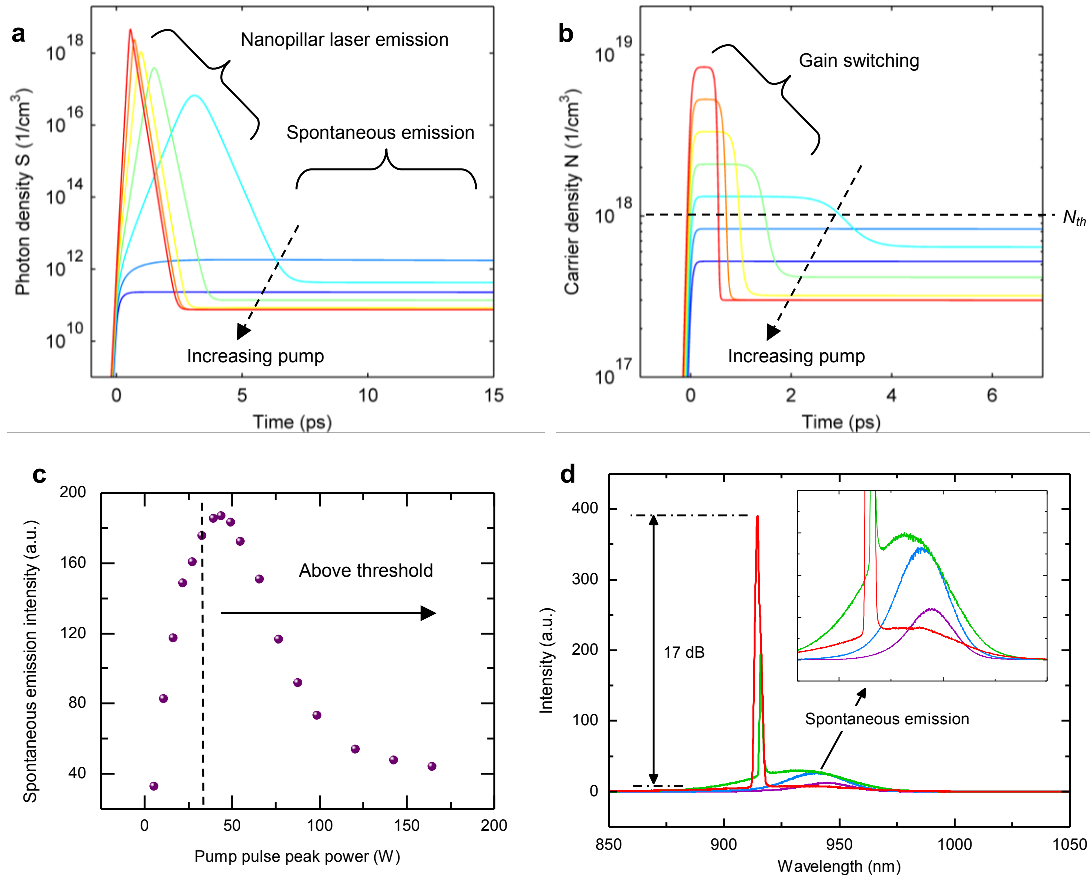

Figure 4.17 Gain switching effects on spontaneous emission. a, The modeled transient photon density response shows a spike of nanopillar laser emission followed by spontaneous recombination after the carrier density drops below threshold as shown in **b**. Higher pump fluences notably cause the initial drop in carrier density to be more drastic, reducing the spontaneous emission above threshold as seen experimentally in **c** and **d**. Here, spontaneous emission reduction rather than clamping can be seen due to gain switching effects.

4.8 Future challenges

This chapter presented results representing significant progress towards nano-optoelectronic integration, but we must conclude it by highlighting the remaining challenges. The path forward towards nano-optoelectronics on silicon is somewhat clearer, but it remains a long and arduous road.

The scheme presented for growing active nanophotonic components on silicon is promising for photonic integration with CMOS circuits. However, electrically pumped lasers are required for such applications. Although nanowire-based light-emitting diodes (LEDs) and lasers have been demonstrated, it remains difficult to fabricate lasers and LEDs using as-grown nanostructures and conventional micro-fabrication techniques. The

nanopillars discussed in this paper present significant advantages. Core-shell layering and doping capabilities greatly facilitate growth of p-i-n heterostructures and quantum wells in nanopillars [97]. Using such structures, electrical injection of as-grown nanopillar LEDs on Si has already been achieved [99]. Notably, these devices were fabricated using standard contact lithography techniques because nanopillars are sizeable and robust. Future electrical contact schemes will account for preservation of nanopillar cavity modes to achieve electrically-injected lasers on Si.

Another critical aspect of silicon optoelectronics is coupling of laser emission into waveguides. From simulations of the helical cavity modes, we find that emission dominates in the in-plane radial direction (see Section 4.6). Nanopillar lasers are thus compatible with the existing coupling schemes used for microdisks and ring resonators [92], [113], [119], [120]. Additionally, various schemes have already been developed to turn in-plane light propagation into surface normal emission and vice versa [121]–[123]. Nanopillar lasers coupled to waveguides are thus promising for optical interconnects or any chip-scale device that requires an integrated light source.

Finally, we note that modern CMOS electronics are fabricated on (100) silicon wafers. Although we presently use (111) silicon substrates to guarantee vertical alignment of nanopillars, this does not prevent nanopillar laser integration onto (100) silicon. (111) facets of a (100) Si substrate can be exposed to grow nanopillars aligned at a 54.7° angle with respect to the surface normal. We have shown that helical laser modes are still strongly supported even for a larger 70° growth angle (see Section 3.2). Of course, scalability of integration onto Si is of utmost importance and requires future work.

Also, a key step forward will be demonstrating the survivability of CMOS circuits after nanolaser growth to verify that this integration method is truly CMOS-compatible. Significant first steps have already been demonstrated by Lu et al [124]. Figure 4.18 shows some other preliminary results. At 4 K, clear evidence of lasing is seen from a nanopillar grown directly on the gate of a metal-oxide-semiconductor field-effect transistor (MOSFET). Of course, growing on MOSFET gates may not be strategy to pursue for integration, but these results show that nanolasers can grown on the irregular terrain that MOS circuits feature. Most importantly, ref. [124] shows that these MOSFET devices do not experience degradation after growth.

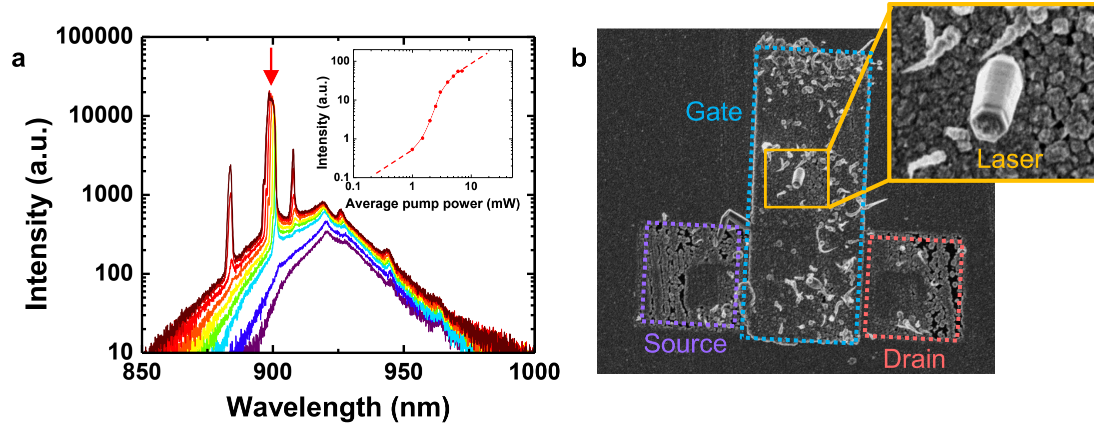

Figure 4.18 Nanolasers grown on MOSFETs. a, Spectral evolution of laser oscillation from nanolasers grown on MOSFETs with the L-L curve in the inset. **b,** SEM image of a nanolaser grown directly on a MOSFET gate.

In this chapter, we demonstrate the first room-temperature III-V nanolaser grown on Si with subwavelength volume. In doing so, we show that lattice mismatch is not a fundamental limit for monolithic integration of III-V photonic devices onto silicon as is generally perceived. A bottom-up approach can provide an effective way of integrating nanophotonics with nanoelectronics. The ability to heavily populate an optically-deficient silicon substrate with efficient III-V lasers has far-reaching implications for silicon photonics, particularly with regard to optical interconnects. With low temperature nanopillar growth, the possibility exists for laser integration after electronics fabrication in CMOS foundries is complete. A new class of helically-propagating modes implement our unique on-chip optical cavities, showing that optical phenomena in all-semiconductor nanostructures can be leveraged for practical on-chip nanophotonic devices. These modes may be leveraged for new designs of optical components such as photodetectors, modulators and solar cells. Future electrical operation of p-i-n nanopillar lasers on silicon meanwhile promises for a powerful marriage between photonic and electronic circuits, and progress towards this goal will be the focus of the next chapter in this dissertation.

Chapter 5

Towards electrically-driven nanolasers on silicon

True optoelectronic functionality requires electrical control of photonic devices. This chapter discusses the fine balance between constraints on electrical injection and optical feedback for nanopillar-based lasers on silicon. When electrically contacting nanopillars, the presence of metal severely perturbs cavity modes in these small structures. Thus, a great deal of care is needed in designing an electrical injection structure that simultaneously supports optical resonances. Here, metal-optics provides an attractive feedback mechanism for small lasers because metal enables small mode volumes while conveniently doubling as electrical contacts.

5.1 Device fabrication and electrical testing

A metal-optic design is chosen for electrically-driven nanopillar laser structures. Metal optics is well-suited for small resonators, and electrically injecting small gain media like nanopillars inevitably requires metal in close proximity to cavity modes. Incorporating nanopillar devices with metal optics presents many fabrication challenges, which will be the focus of this section.

Though we focus on fabrication here, any discussion would be incomplete without at least a brief introduction to the active nanopillar material used for devices. In Section 2.3, we show how nanopillars are grown in a layer-by-layer fashion. We also discuss how the composition of each layer can be finely tuned to create radial core-shell heterojunctions and quantum wells. Per the results of ref. [125], each layer can also be doped to make radial core-shell p-i-n junctions. This is critical for electrically controlling devices since doping enables ohmic contacts, which are required for efficient carrier injection. The schematic in Fig. 5.1a reflects a typical nanopillar structure used for device fabrication. Figure 5.1b meanwhile shows how a metal-optic cavity can be integrated with the active material in Fig. 5.1a. Various nanopillar dimensions were used for device fabrication ranging from 800 nm to 1.6 µm in diameter and 500 nm to 4 µm in height. We found that larger nanopillars showed the most promise in terms of achieving electrically-driven

lasers on silicon, likely because of the higher Q and lower resistance associated with larger devices.

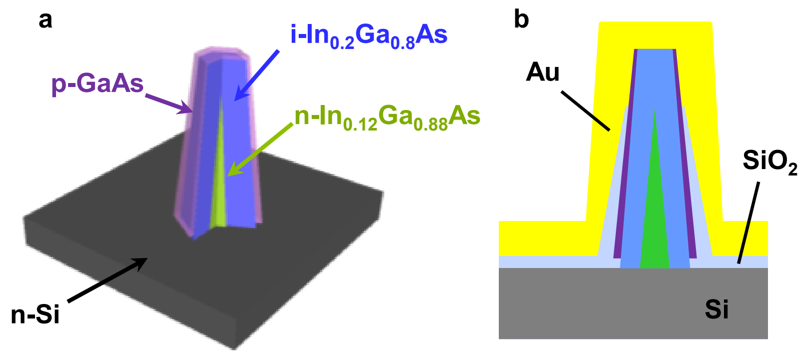

Figure 5.1 Schematics of nanopillar device active material and metal-optic cavity. a, A schematic of the active material used for electrically-controlled nanopillar devices shows its p-i-n double heterojunction. **b,** A metal-optic cavity can clad nanopillars by careful conformal deposition of oxide and metal films.

The first and foremost challenge facing fabrication of nanopillar-based devices is the lack of site control in nanopillar growth. At present, nanopillars grow spontaneously on silicon at randomized locations such that each device sample requires its own unique set of lithography masks. Electron beam (e-beam) lithography is thus a critical technology for nanopillar devices, and considerable effort has gone into developing e-beam processes. E-beam lithography allows users to quickly generate custom mask designs for unique samples, and certainly each nanopillar sample is unique from all others. We leverage e-beam for this reason and not for resolution requirements. Nanopillars are in fact compatible with contact lithography [125], and in the long term, conventional lithography provides a much more practical and scalable solution. Of course, site-controlled growth of nanopillars must be developed first.

Figure 5.2 summarizes a typical e-beam process developed for processing single nanopillar devices. Though many iterations of this process exist, the diagram provides a useful point of reference anytime we mention e-beam processing going forward. Typically, a sample is first patterned with high-precision and local metal alignment markers using e-beam lithography. These alignment markets effectively define a relative x-y coordinate system, which can be used to triangulate and define relative coordinates for a certain nanopillar of interest. Using L-Edit or a similar computer-aided design tool, electron beam masks can then be made based on those coordinates. The e-beam machine can then determine where exactly in real space a nanopillar of interest resides by aligning itself to the alignment markers on the sample. Thus, the e-beam tool can easily write patterns onto nanopillars, whether those patterns are etch masks as in step 5 or electrical contacts as in step 6.

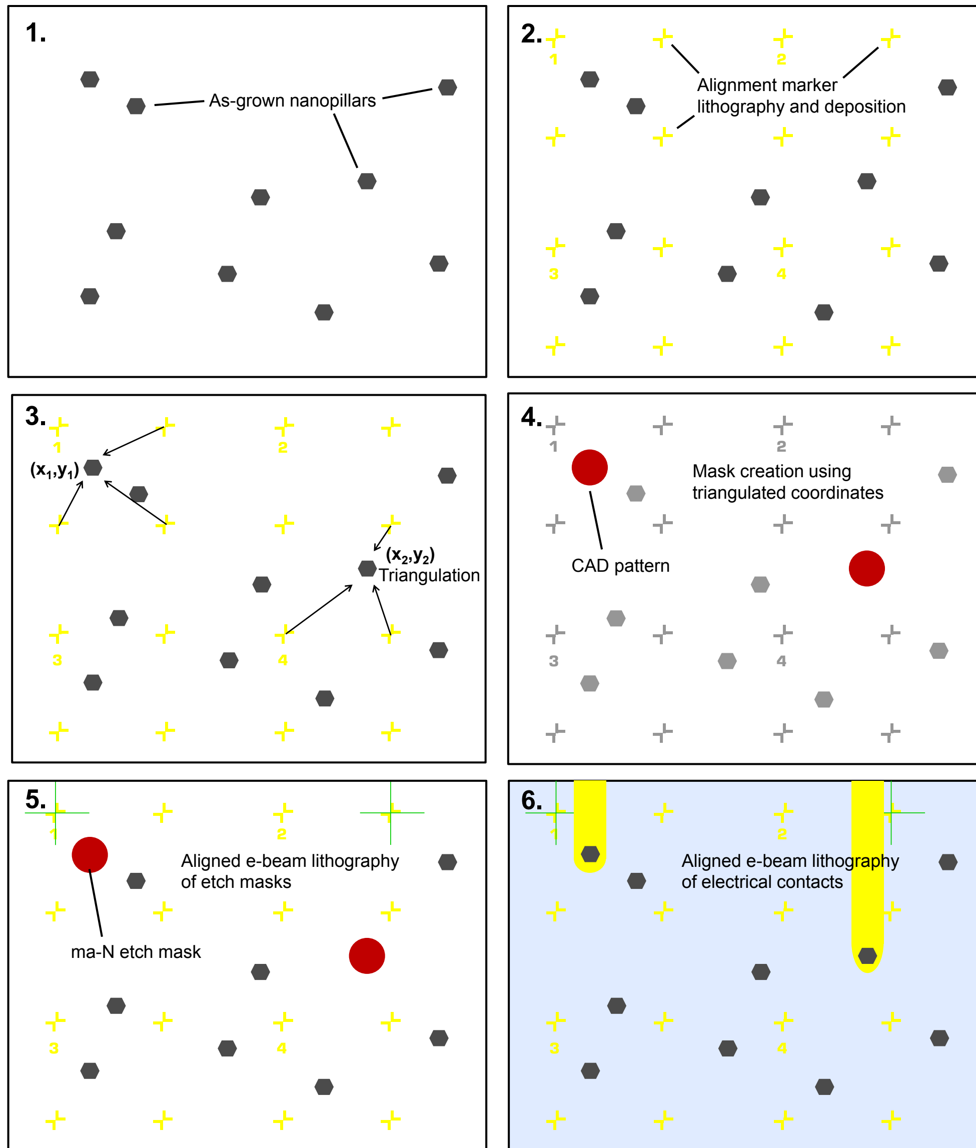

Figure 5.2 Process flow for e-beam lithography of nanopillars. Additional details of the process can be found in the main body of text.

Minimizing current leakage in nanopillar devices is required to maximize device performance. The polycrystalline film (see Section 2.3.1) formed during nanopillar growth is a major source of such leakage as shown in Fig. 5.3. While the single-crystal nanopillar features high-quality junctions, poor interfaces within the polycrystalline film would pass current well below the turn-on voltage of the device. Effectively then, the polycrystalline layer functions as a shunt path for nanopillar devices. Increasing the shunt resistance as high as possible provides a reasonable way of reducing current leakage. Intuitively, leakage should scale with the area of the polycrystalline film lying within a carrier diffusion length of the nanopillar. Thus, removing as much of the leaky

polycrystalline layer as possible will allow more current to pass down the desired path through the p-i-n junction.

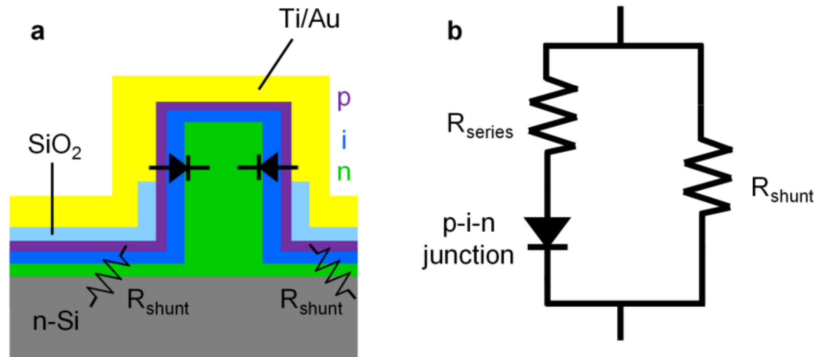

Figure 5.3 Leakage paths in nanopillar diodes on silicon. a, The poor junctions in the polycrystalline layers surrounding single crystal nanopillars give rise to shunt paths for current leakage as shown. **b,** This can be modeled by the simple circuit shown. Maximizing R_{shunt} can help maximize current through the useful diode path.

Figure 5.4 walks through this process and the rest of the steps needed for fabricating nanopillar LED and laser structures. First, an as-grown p-i-n nanopillar is conformally coated with SiO_2 by plasma-enhanced chemical vapor deposition (PECVD). Negative e-beam resist (ma-N 2410) is then spun onto samples, followed by e-beam lithography to define etch mask patterns over select nanopillars. Buffered oxide etch (BOE) 5:1 then etches away the SiO_2 except for what remains protected by ma-N on nanopillars of interest. The ma-N e-beam mask is then removed, leaving behind an SiO_2 hard etch mask. This mask protects nanopillars from the dry etch process used to remove much of the polycrystalline layer as shown in step 7 of Fig. 5.4. Residue remaining from the polycrystalline layer is then cleaned off by wet etching with diluted sulfuric acid.

At this point, most of the leaky film will have been removed. Next, the oxide etch mask is stripped and a second PECVD step again coats the nanopillar with SiO_2. This second oxide layer will serve to electrically isolate the p- and n-layers of nanopillars. Standard photoresist is spun and etched back via oxygen plasma to expose the oxide near the top of nanopillars for etching. Etching the oxide there opens up the p-doped shell of nanopillars for electrical contact. Depending on how the contacts are metallized, either LED or laser structures can be fabricated. For LED structures, only one side of the nanopillar is metallized so that emission couples out from the uncoated side. The laser structure meanwhile features conformal metallic coating to completely embed the electrically-contacted gain medium inside a full metal-optic cavity. Metallization in this case is achieved by off-axis rotation of the sample mounted at an angle during electron beam evaporation.

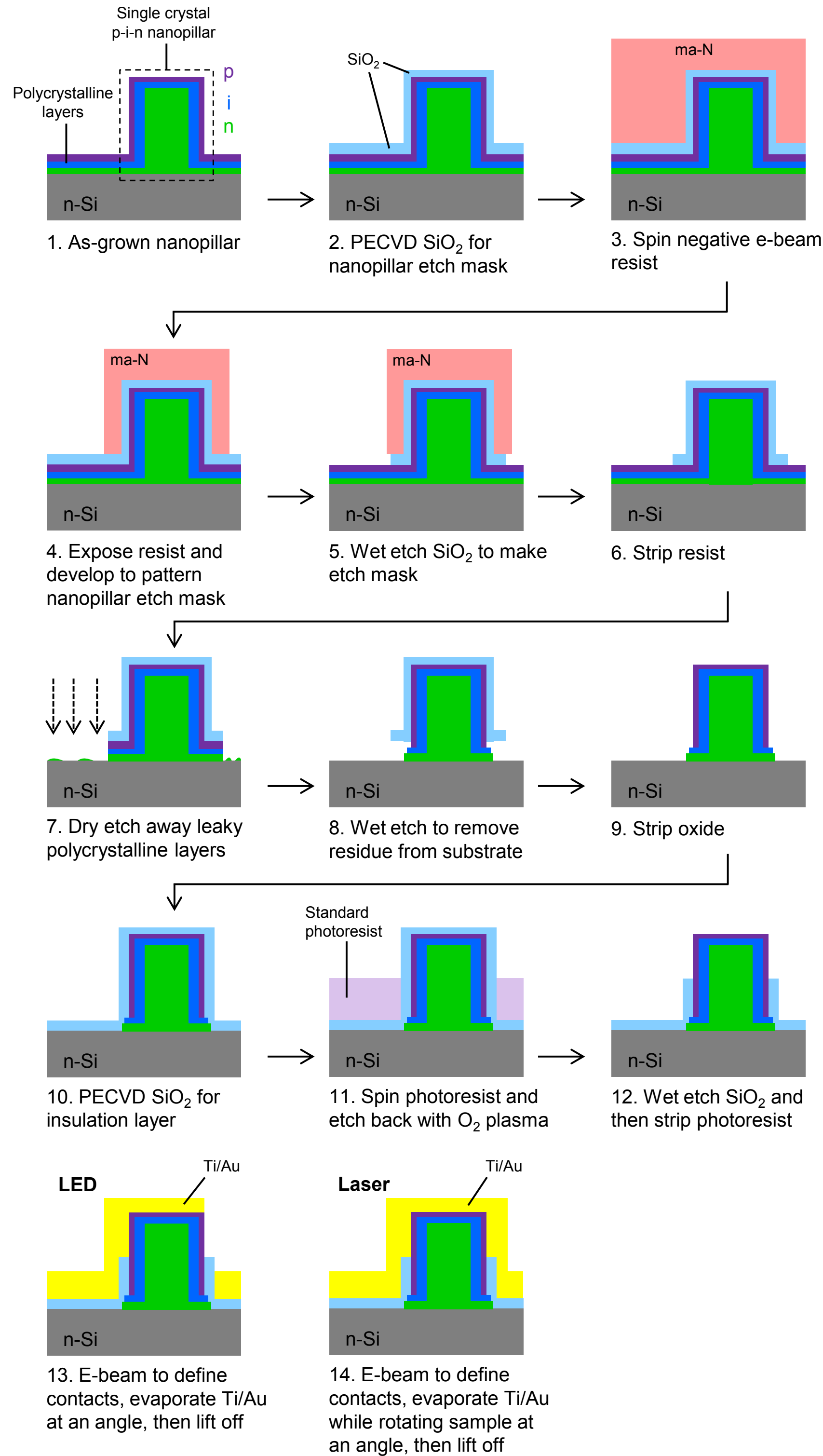

Figure 5.4 Fabrication process flow for electrically-injected nanopillar light-emitting diodes and lasers. Additional details are discussed in the main body of text

Figure 5.5 shows scanning electron microscope (SEM) images of various nanopillars at various stages of the fabrication process. Figure 5.5a offers a glimpse of the e-beam process, particularly step 3 shown in Fig. 5.2.

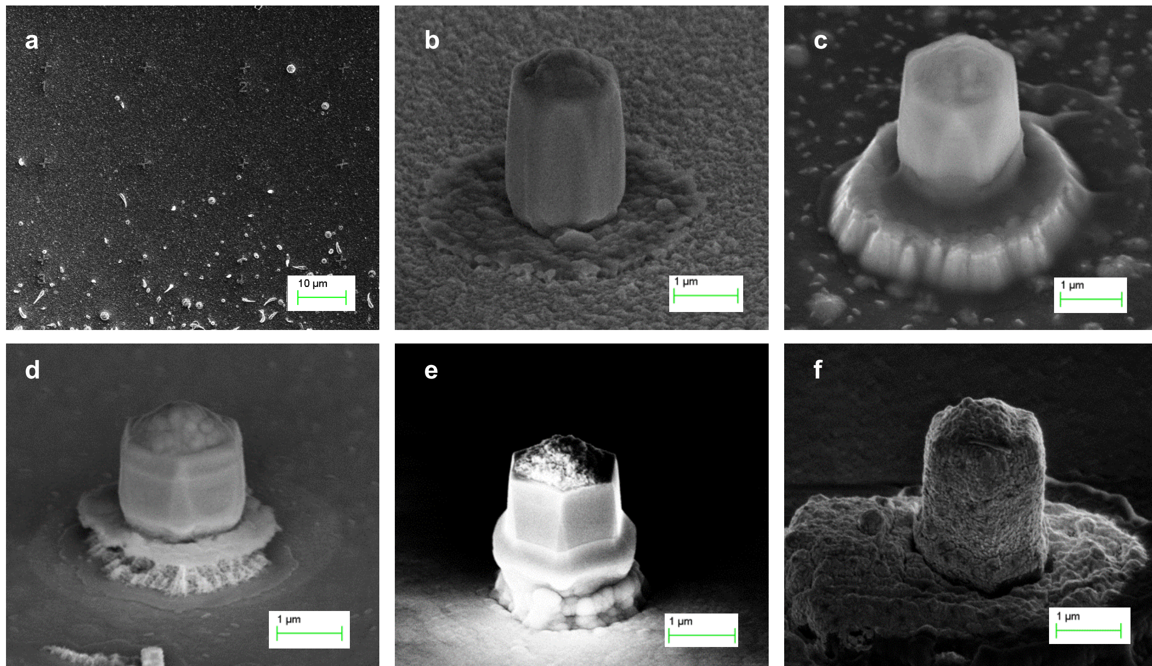

Figure 5.5 Nanopillars at various stages of the laser structure fabrication process. a, Alignment markers allow the relative positions of nanopillars to be defined. A nanopillar is coated by **b,** a SiO_2 etch mask before **c,** undergoing dry etching and **d,** wet etching. **e,** A second oxide deposition isolates p- and n-contacts while also forming the dielectric portion of the metal-optic cavity. **f,** Rotating the sample at an angle during e-beam evaporation coats the nanopillar with metal and thereby completes fabrication of the electrically-injected metal-optic laser structure.

After optimizing contact fabrication processes and nanopillar laser diode heterostructures, we have reproducibly achieved single nanopillar devices with clear and consistent rectification properties as shown in Fig. 5.6a. Figure 5.6a simultaneously plots the current-voltage (I-V) curves of dozens of devices. They all exhibit similar diode behavior, which is notable considering that significant variation intrinsically exists even among nanopillars on the same sample. The turn-on voltage for these devices is typically ~1 V, which is slightly lower than expected for the GaAs-based material system used. This may be due to the impact of the nanopillar geometry and its core-shell nature and requires further investigation. Under reverse bias, nanopillar devices break down between -3 to -4 V. Certainly, a larger breakdown voltage may be desirable, but it is much less relevant for LED and laser devices meant for operation under forward bias. For photodetectors, increasing breakdown voltage is important, and it is entirely possible as discussed in Section 6.1.

Ideality factors for nanopillar devices typically range between 2.3 to 3 as shown in Fig. 5.6b. This nearly-ideal value importantly signifies the quality of nanopillar junctions and that desirable recombination dynamics exist within the structures. Nanopillar diode devices also exhibit low dark currents. When biased at -3 V, some devices show dark currents of only 0.3 nA, which compares favorably to traditional GaAs-based devices. Ideality factor and dark current become particularly important parameters deserving attention for other devices explored in this dissertation, including avalanche photodiodes and photovoltaics.

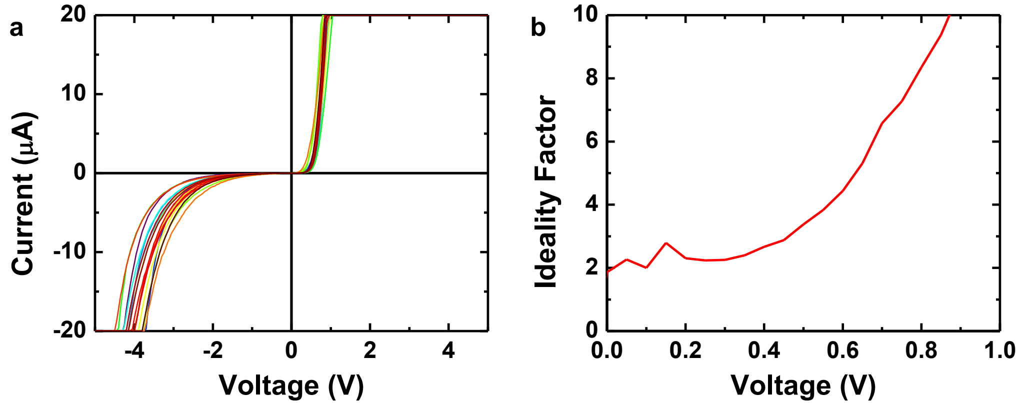

Figure 5.6 Electrical characteristics of nanopillar devices. a, Dozens of I-V curves show clear and consistent diode behavior, testifying to the robustness of the fabrication process flow. **b,** Devices can exhibit diode ideality factors of nearly 2, a nearly ideal value for GaAs-based diodes.

5.2 Electroluminescence experiments

After summarizing the electrical performance of nanopillar devices, let us now turn to their optical properties. Electroluminescence (EL) was measured from nanopillar devices at temperatures ranging from 300 K to 4 K. Room temperature testing was relatively straightforward. An electrical probe biased a nanopillar LED, while the photoluminescence setup described in Section 2.3.2 was used to collect and characterize LED emission. Low temperature experiments required more careful planning and are further discussed here. To achieve low temperatures, liquid helium was flowed into a cryostat (Oxford Microstat Hi-Res II) that contained nanopillar LEDs mounted onto a cold finger. A heater inside the cryostat enabled users to control the temperature of the sample. When the heater was off, the cold finger temperature simply cooled down to that of the liquid helium flowing in, which was typically around 4 K. When maximized, the heater could warm samples up to 500 K.

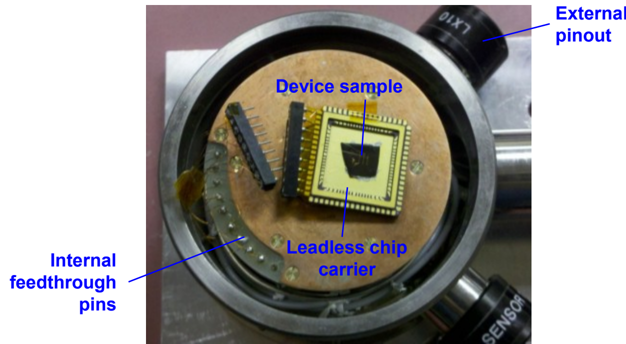

Figure 5.7 Electrical connections inside a cryostat used for electroluminescence. A device sample is first mounted on a leadless chip carrier, which then mounts onto the cold finger of the cryostat. Devices are wire bonded to the chip carrier, and a plug electrically connects the chip carrier to an external pinout using the cryostat's built-in feedthrough pins.

Samples mounted inside the cryostat were biased by using electrical feedthroughs that connected pins inside the cryostat to an external pinout. Bonding feedthrough pins to fragile metal pads on device samples proved impractical. Thus, samples were first mounted onto leadless chip carriers (LCCs) using silver paste. The sample's device pads were then wire bonded to the contact pads of the LCC, which electrically contacted the cryostat's feedthrough pins through soldered wire connections. The external pinout was then connected to a either a direct current (DC) or pulsed source using a customized cable. Figure 5.7 shows an image of these electrical connections. Meanwhile, device emission was collected and characterized through the cryostat's optical window.

We offer a caveat here about the aforementioned sample preparation. Extreme care must be taken in handling devices throughout the process due their susceptibility to electrostatic discharge (ESD). Many devices fell victim to ESD, reminding us of the power that simple static can sometimes possess. A look in literature shows that other small lasers such as vertical-cavity surface-emitting lasers (VCSELs) have dealt with this often overlooked, yet serious issue. We also note here that this section discusses only data from light-emitting diode structures with metal evaporated on a single side of each nanopillar. That is, no optical cavities were formed for any of these devices. The next section will summarize experimental results for electrically-driven emitters embedded in a conformal metal-optic cavity.

For continuous wave (CW) measurements, a parameter analyzer supplied DC voltage and current to nanopillar LEDs. Figure 5.8 presents electroluminescence spectra from a single nanopillar LED under various current levels at 4 K. At first, higher current leads to stronger emission intensity as might be expected. However, with even higher bias, emission begins to reduce. Examining how the spectrum changes in terms of shape and wavelength offers some insight on why this happens. Notably, the spectrum shifts to redder wavelengths at high pump currents. Under 1 mA bias, it is also apparent that the spectrum has significantly broadened. Both broadening and redshifting typically indicate

strong heating effects driven by resistive loss. Reduction of contact resistance in the future will reduce this heating effect such that its onset only comes at even higher currents.

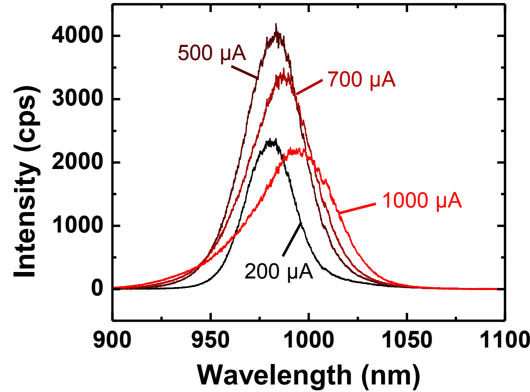

Figure 5.8 Continuous wave LED electroluminescence at 4 K. Nanopillar LEDs emit bright electroluminescence under continuous wave operation. Under stronger bias levels, emission redshifts and decreases due to thermal effects.

Figure 5.9 shows EL from nanopillar LEDs at room temperature. DC current was applied from 100 µA to 700 µA with EL intensity rising steadily before eventually rolling over. The light-current (LI) curve shown in Fig. 5.9b shows this progression a little more clearly. At the lower end of the pumping range, the LI curve is slightly exponential. This often occurs because the internal quantum efficiency of an LED will improve under higher carrier concentrations as nonradiative states become saturated. The LI curve then becomes fairly linear over the middle of the pumping range before rolling over due to thermal effects under the high end of the range. Interesting peaks were observed in the EL spectra for this and other devices, but it is clear from the LI plot that lasing has not been achieved. Likely, the peaks come from exciting different transitions within the material itself. Nonetheless, EL from a single nanopillar LED is extremely bright. Even at room temperature, emission can be easily seen on CCD camera as shown in Fig. 5.10. If its wavelength was visible rather than near infrared (NIR), the light could be seen by naked eye.

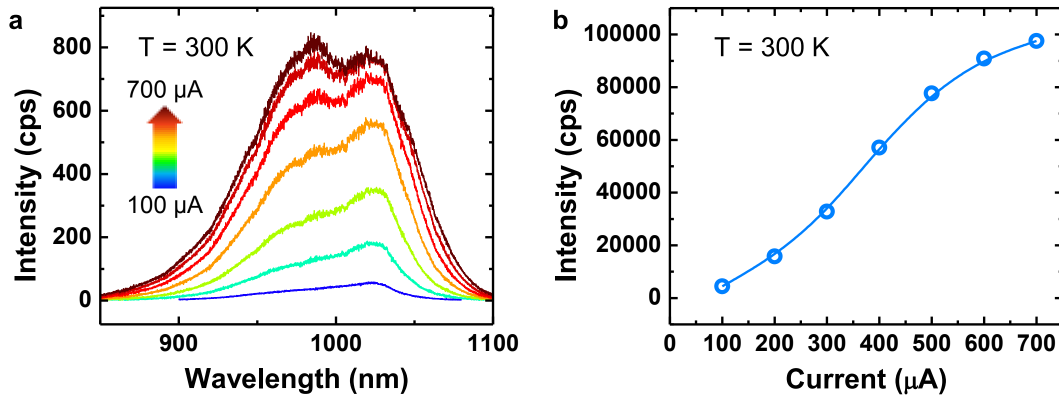

Figure 5.9 Continuous wave LED electroluminescence at room temperature. a, At room temperature, electroluminescence from single nanopillar LEDs is bright and can withstand high continuous wave current densities. **b,** The L-I curve shows a slightly nonlinear increase in light output before the device emission rolls over due to heat.

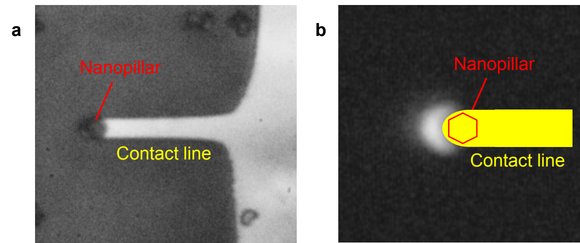

Figure 5.10 Room temperature images of electroluminescence. The device in **a** emits light bright enough to be imaged with a CCD camera as shown in **b**. The light would be visible to the naked eye if it were at visible wavelengths.

Under pulsed excitation, nanopillar LEDs suffer less from heating effects, though they still ultimately impact device performance. In Fig. 5.11, EL spectra show clear band filling and blueshifting before heating begins to set in. Devices were highly stressed by electrical pulses with peak voltages up to 12 V. The pulse width was nominally 20 ns with a 1% duty cycle, though experiments indicated that pulse widths were actually at least 50 ns long due to transient effects. Heating was not noticeable until 5 V pulses were applied. Even then, heating was not severe and EL intensity continued to grow before ultimately the device reached its limit. As expected, it is clear then that pulsed pumping allows the limits of nanopillar devices to be pushed much further. For testing first-generation diode nanolasers like the ones discussed in this dissertation, pulsed pumping thus becomes the weapon of choice.

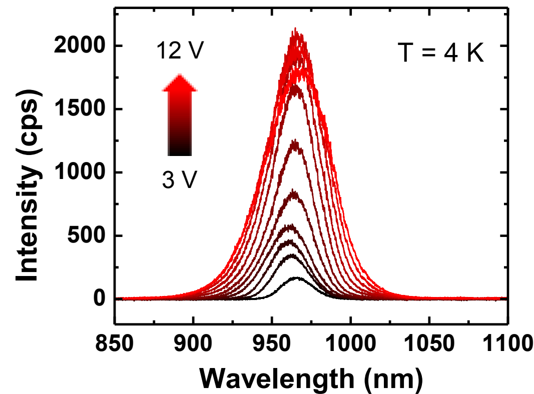

Figure 5.11 Pulsed LED electroluminescence at 4 K. Strong band filling and emission results from injection of high-voltage pulses. It is unknown how much current couples into devices due to a large impedance mismatch.

5.3 Electrically-driven amplified spontaneous emission

By embedding nanopillars in a metal-optic cavity, we achieved amplified spontaneous emission (ASE) under electrical pumping. Figure 5.12a shows an SEM image of such an ASE device. Because these metal-optic resonators had considerable optical loss, relatively high currents were required to achieve enough gain to see ASE. Thus, ASE only arose with the advantage of pulsed pumping. Under CW bias, devices were severely limited by the thermal effects described in the previous section. In Fig. 5.12, we see the tremendous benefit of pulsed pumping. It achieved roughly 75 nm of band filling before cavity peaks appeared due to the high material gain associated with that amount of band filling. By comparison, the EL spectra generated by 200 μA CW current was over 50 times weaker with no evidence of amplification. We note that a peak voltage of over 4 V was required before we could observe ASE, which should correspond to excessively high currents. However, due to large uncertainty with regard to impedance mismatch and transients in the nanopillar device, it is presently unclear how much current is actually injected for these voltage readings. This will be a topic of future study.

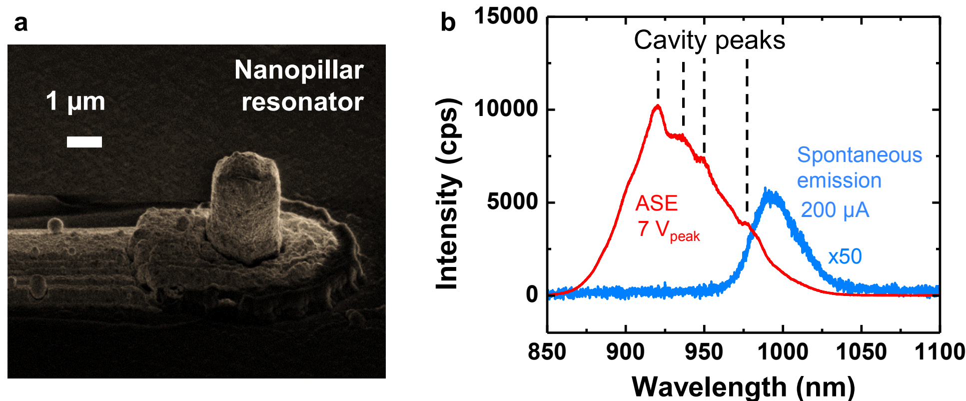

Figure 5.12 Amplified spontaneous emission from nanopillar devices. a, An SEM image of an electrically-driven single nanopillar laser structure. **b,** These structures exhibit amplified spontaneous emission under pulsed pumping at 4 K, though lasing has not yet been achieved. Prominent band filling effects can be observed when comparing the ASE spectrum to the spontaneous emission one.

Various studies were performed to confirm attribution of EL peaks to ASE. Analyzing the pump dependence of devices, which is presented in Fig. 5.13, is one such study. Another is temperature dependence, which this section later discusses. Like lasers, ASE causes a nonlinear increase in total light emission due to amplification. However, the magnitude of amplification pales in comparison to that of a laser, and ASE does not achieve fully coherent light. This means that ASE spectra can grow rapidly in intensity and may even exhibit cavity modes, but never reveal any dominant laser oscillation peaks. As shown in Fig. 5.13a, EL spectra from a nanopillar resonator reflect these very characteristics. As the peak pulse voltages step from 2 V to 7 V, the amount of emission explodes and peaks clearly emerge from the spontaneous emission. For these experiments, nominally 20 ns pulse widths with a 0.2% duty cycle were used. Figure 5.13b more clearly illustrates the impact of ASE on emission intensity. Between 5 V to 6 V, light output grows by nearly an order of magnitude before rolling over and eventual device failure. Though this threshold behavior is suggestive of laser oscillation, we see from corresponding spectra that the emitted light is far from coherent. This fact serves as a lesson that a threshold in an LI curve is far from sufficient proof that lasing has been achieved.

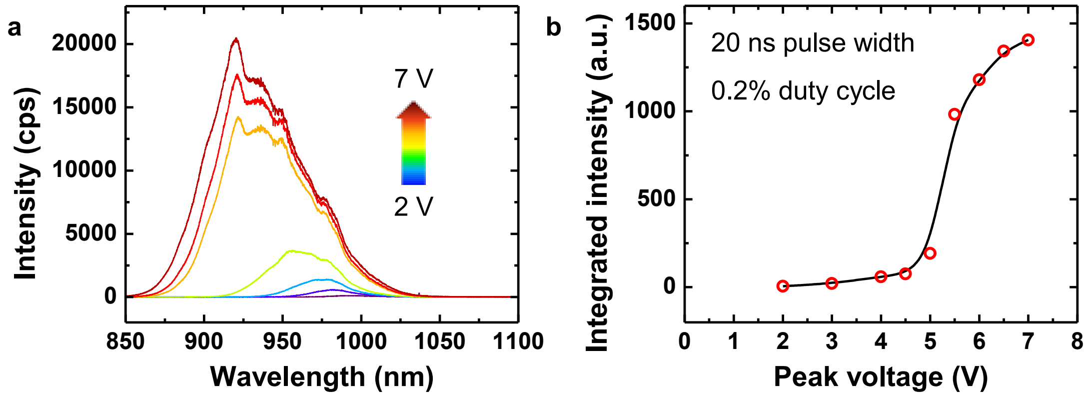

Figure 5.13 Pump dependence of amplified spontaneous emission. a, ASE featuring many prominent peaks explodes rapidly under higher pumping levels, which can be even more clearly seen from the L-I curve of **b**.

Temperature-dependent data provides additional evidence for the claim that nanopillar resonators can achieve ASE under electrical injection. It is known that wavelengths for both semiconductor electroluminescence and optical resonances shift versus temperature [126]–[130]. It is also understood that they do so at different rates and in a different fashion. EL shifts depend on the temperature dependence of a material's band gap, while resonances shift depending on the temperature dependence of a material's refractive index. Thus, examining how temperature affects an overall EL spectrum and its various peaks should shed additional insight on the origin of those peaks.

Figure 5.14 presents the results of such a study on nanopillar resonators. As highlighted in Fig. 5.14a, peaks in the EL spectrum (labeled A-D) redshift more slowly with temperature than the overall EL spectrum's center wavelength (labeled X). Concurrently, the peaks become weaker at higher temperatures, though this can occur whether or not the peaks come from ASE. Figure 5.14b more explicitly plots how the broad EL spectrum appears more sensitive to temperature than the peaks superimposed on it. Whereas peaks A-D shift approximately 10 nm in wavelength, peak X shifts nearly 20 nm over the same temperature range. Notably, peaks A-D all shift in a rather parallel fashion, suggesting that they vary in temperature by the same mechanism.

These observations can be explained by the stronger temperature dependence of band gap compared to refractive index. When plotting the wavelength shifts as percentages as in Fig. 5.15, we can easily compare our results to well-known and existing models. We find that the ASE peaks shift at a rate corresponding to a thermo-optic coefficient of $dn/dT=2.67\times10^{-4}$, thereby substantiating their origin from cavity modes since optical resonances are linearly dependent on refractive index [128], [129]. Meanwhile, peak X follows the Varshni model known for describing the temperature dependence of semiconductor band gaps [126]. We note that there is a deviation from the Varshni model at higher temperatures, which is a topic of future investigation.

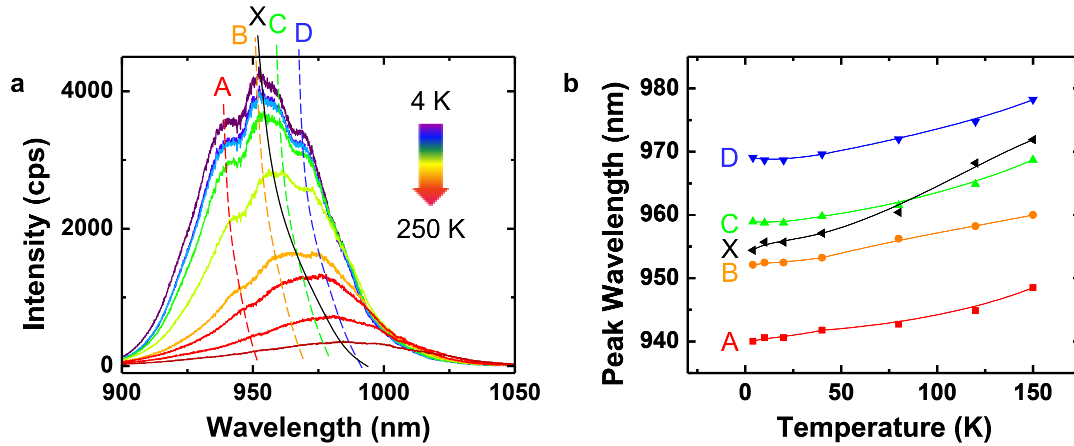

Figure 5.14 Temperature dependence of amplified spontaneous emission spectra. a, Electrically-injected emission spectra show several ASE peaks (A-D) superimposed upon a broad spontaneous emission background (X). Temperature dependence studies were done to verify the origin of these peaks. **b,** Spontaneous emission (X) shifts more quickly with temperature than the purported cavity peaks (A-D), which shift in parallel with one another.

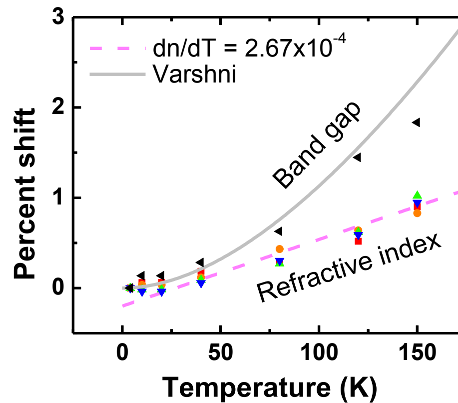

Figure 5.15 Fitting temperature dependence of amplified spontaneous emission. The observed temperature dependences can be explained by the different temperature dependences of band gap and refractive index, which determine energy shifts of spontaneous emission and cavity resonances, respectively. We find that peak X follows the Varshni model for energy band gaps, while peaks A-D follow a typical GaAs thermo-optic coefficient of $dn/dT=2.67\times10^{-4}$. We thereby confirm our attribution of observed spectral peaks to ASE.

Any electrically-driven laser requires that there be: (1) sufficient gain achieved from electrical injection and (2) sufficient optical feedback for full laser oscillation. While we

achieved ASE, it remained unclear which of these two factors prevented lasing from ultimately occurring. Thus, we further modeled our data to calculate how much gain has been experimentally realized thus far. To do this, we fitted experimental electroluminescence curves with analytical formulae following a procedure similar to that described in Section 4.7.1. The result of the fit is shown in Fig. 5.16a. Based on our fitting parameters, we can extract a quasi-Fermi level splitting of 1.384 eV and carrier concentrations of N~P~3.1x10^{18} cm^{-3}. Given the close relationship between spontaneous emission and gain, a gain spectrum can also be calculated for our device as presented in Fig. 5.16b. Our analysis shows that a gain of ~3,400 cm^{-1} has been experimentally achieved at the peak wavelength of the ASE spectrum, and even higher gain can be achieved if resonances exactly match the gain spectrum peak. Gain of 3,400 cm^{-1} is very often more than sufficient to achieve lasing since it only requires that the optical cavity quality factor be greater than 74 (assuming mode confinement factor of 1). The result of our analysis thus motivates more focus on optical cavity design, which clearly appears to be the present roadblock towards full laser oscillation. By improving cavity quality factor, we will fill fulfill the two attributes that any electrically-driven laser requires. The path towards an electrically-driven nanolaser on silicon is clear.

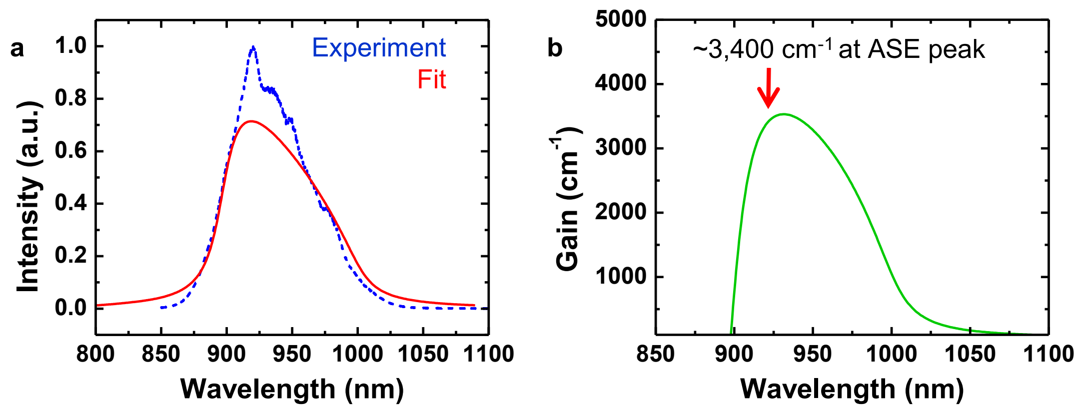

Figure 5.16 High material gain under electrical injection. a, Experimental ASE curves are fitted by analytical formulae using the proper parameters. This analysis allows us to calculate many relevant metrics including quasi-Fermi level splitting and carrier concentration achieved under electrical injection. **b,** Based on our spectral fit, we can generate a gain spectrum for the measured device, showing that experimental gain >3,400 cm^{-1} can already be achieved.

5.4 Quantum well-based devices

Today, most commercial diode lasers use quantum wells (QWs) as the active material. Quantum wells can offer many advantages over bulk gain such as reduced lasing threshold, lower chirp, a larger design parameter space, and potentially higher bandwidth [131]. Whether or not quantum wells actually offer higher speed operation has sometimes been a point of contention. Additionally, the aforementioned advantages were only

achieved after many years of painstaking development and optimization of epitaxial QWs. The first QW lasers performed worse than their bulk counterparts. Carefully grading junction compositions, employing separate confinement heterostructures, and optimizing QW design had to occur to clearly demonstrate the potential of QWs for superior performance [132]–[135]. It is clear then that though QWs within nanopillars may offer advantages, they will not come to fruition until much effort has gone into developing them. Despite this, it is reasonable to expect from history that QW nanopillars may ultimately also offer superior performance. For this reason, we have initiated exploration of QW nanopillar active materials on silicon and discuss results in this section.

The same mechanism used for growing nanopillar heterojunctions was leveraged to grow QW nanopillars, though the QW structure was much more intricate. Because nanopillars grow in a core-shell fashion, QWs form as thin concentric layers wrapping along the hexagonal perimeter of the nanopillar. Figure 5.17a shows a side-view schematic of a QW nanopillar's various layers. An n-type (~$10^{18}/cm^3$ Te-doped) GaAs nanoneedle core is first grown using low-pressure metal-organic chemical vapor deposition (MOCVD) at a CMOS-compatible temperature of 400°C on an n^+-(111) Si substrate. A nominally 8 nm thick intrinsic $In_{0.3}Ga_{0.7}As$ QW is then grown between two ~85 nm i-GaAs barriers. The high indium composition of the QW layer stops vertical growth such that subsequent shell growth transforms the NN structure into a NP with a flat top. A ~125 nm p-type (~$10^{18}/cm^3$ Zn-doped) $Al_{0.2}Ga_{0.8}As$ cladding and a thin p-type GaAs contact layer are then grown to complete the structure. Additional details of the growth can be found in ref. [125].

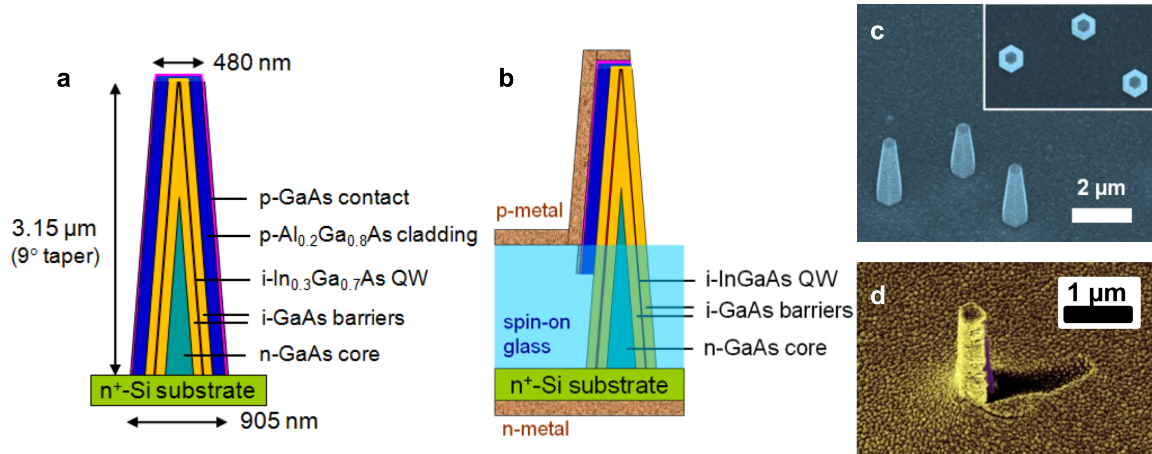

Figure 5.17 Quantum well light-emitting diodes. Schematics of the as-grown quantum well structure and the quantum well LED are shown in **a** and **b**, respectively. Meanwhile, **c** and **d** show SEM images of the as-grown sample and fabricated device.

Using photolithography, angled metal deposition, and various etching processes, we carefully define metal contacts on these p-i-n QW nanopillars as shown schematically in Fig. 5.17b. Whereas e-beam lithography was used to make LEDs from single bulk double

heterostructure nanopillars, only contact lithography was used to produce devices from QW nanopillars. For these initial experiments, a large matrix of 200 μm x 200 μm pads were deposited on sample substrates, and LEDs were characterized when these pads fortuitously contacted randomized nanopillars with success. For working devices, an average of 30 nanopillars were contacted simultaneously, though characterization was always performed on emission from a single nanopillar at a time. Figures 5.17c,d show SEM images of as-grown QW nanopillars and a fabricated QW LED, respectively.

In order to characterize the LEDs, EL is coupled from devices to a 20x 0.4NA objective and relayed to a LN_2-cooled InGaAs CCD. All measurements on QW LEDs were done at room temperature. With a relatively narrow full width at half maximum (FWHM) of 64 nm, the EL spectrum plotted in Fig. 5.18a testifies to the high optical quality of the QW nanopillar structure. For comparison purposes, the PL spectrum of a quantum well nanopillar is co-plotted on the same graph. No doping was added for the samples used for PL because doping adds impurity-related emission when optically pumped. Comparing the PL and EL spectra, we find that they share remarkably similar lineshapes and FWHMs, indicating effective electrical injection and recombination of carriers in the QW layer. Further, their similarity shows the robustness of the NP despite the LED fabrication process. Notably, the EL spectrum is redshifted from the PL spectrum by 67 nm. This is attributed to thermal differences between optical and electrical excitation and possibly the Quantum Confined Stark Effect due to applied electric fields. Further work remains to investigate these issues and to improve device performance such as efficiency. Figure 5.18b shows the LI curve of a QW nanopillar LED, showcasing its linearity.

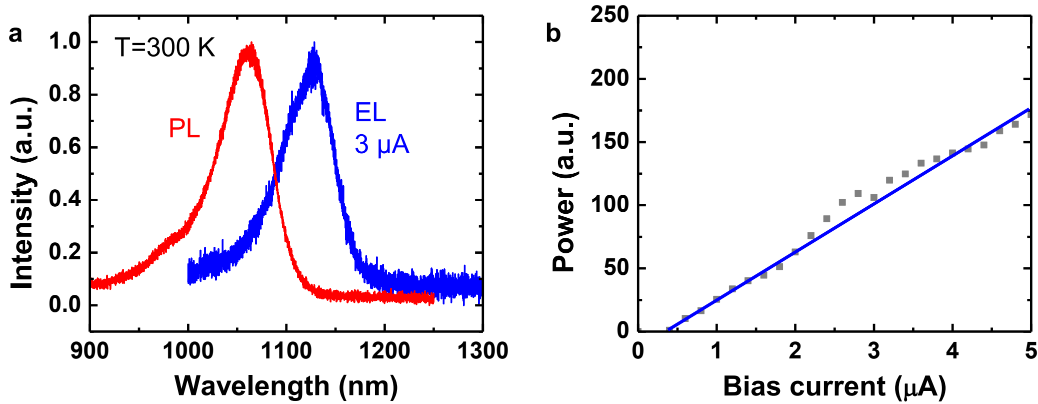

Figure 5.18 Room temperature electroluminescence from quantum well light-emitting diodes. a, PL and EL spectra of the QW LED at room temperature shows. **b,** EL is highly linear versus pump current.

Chapter 6

Avalanche photodiodes on silicon

The ability to harness photons and convert them to electrons is every bit as important as the reverse process focused on in previous chapters. Many applications, including optical interconnects, require photodetectors integrated on silicon (Si). As computing power continues to centralize in the form of data centers, chip-level data transport capacity becomes increasingly critical. Using silicon photonics to implement low-power optical interconnects is a promising approach to solving impending bandwidth limitations [14], [13]. At the receiving end of any optical link is the photodetector. In the past few years, several groups have demonstrated high-performance avalanche photodiodes (APDs) using Ge and Si material systems [136]–[138]. Using III-V active materials nonetheless remains attractive because of their supreme optoelectronic properties. However, the inability to monolithically grow quality III-V films on Si has severely inhibited this approach. In this chapter, we show that single crystal III-V nanostructures directly grown on silicon can implement high-speed and high-gain APDs. In additional to their potential for chip-scale optical interconnects, APDs on silicon may also enable sophisticated imaging and ranging systems integrated onto complementary metal-oxide-semiconductor (CMOS) circuits.

6.1 Device fabrication

Techniques used to produce nanopillar light-emitting diodes (LEDs) were leveraged to fabricate nanopillar-based APDs. Figure 6.1 shows a schematic and scanning electron microscope (SEM) image of a completed device. Like the diode nanolaser, an APD uses a radial p-GaAs/i-$In_{0.2}Ga_{0.8}As$/n-$In_{0.12}Ga_{0.88}As$ nanopillar structure on n-Si as the active material. Devices were fabricated for a range of nanopillar diameters from 800 nm to 1.6 μm. Fabrication included a series of lithography, etching, and deposition steps similar to those outlined in Section 5.1. However, some key modifications were necessary in considering the photodetector. Whereas lasers and LEDs can tolerate some baseline current leakage, even a small amount of dark current can strongly affect photodetector performance. For LEDs, leakage is acceptable as long as it is a small fraction of the useful injected current, which tends to be orders of magnitude larger. For photodetectors, the absolute value of dark current is extremely important since it directly affects the noise and sensitivity limits of the photodiode.

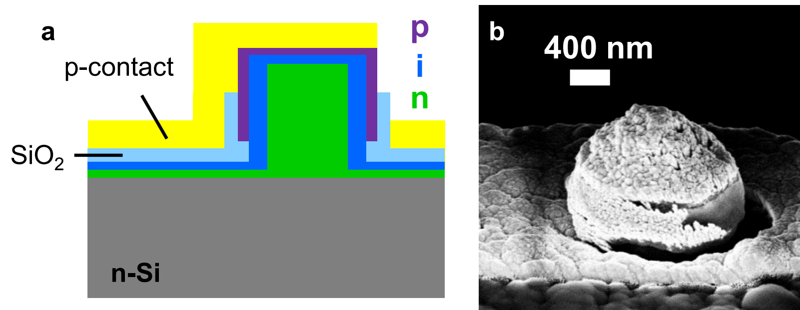

Figure 6.1 Nanopillar avalanche photodiodes. a, A schematic of a nanopillar avalanche photodiode is shown. **b,** An SEM image of nanopillar avalanche photodiode.

A major source of dark current in nanopillar devices is the significant leakage path that exists through the polycrystalline layer formed on the Si substrate. For forward-biased light-emitting diodes, removing most of this layer reduced leakage by a satisfactory amount. Remnants of the poly-layer around the bases of nanopillars can nonetheless result in dark currents ranging from hundreds of nA's to even μA's. Under even low reverse bias voltages, significant leakage paths through the poly-layer can activate. Completely breaking the electrical connection between the p-layer of the nanopillar with the polycrystalline film can greatly improve dark current behavior by minimizing that leakage path. Figure 6.2 outlines this process.

First, SiO_2 is evaporated on a sample of as-grown nanopillars. Due to imperfect evaporation directionality and shadowing effects, clusters of SiO_2 residue formed on nanopillar sidewalls. Oxide on both the sidewalls and tops of nanopillars hurt adhesion of etch masks to be formed later. Thus, oxide was removed from both surfaces before continuing with the process. To do this, standard photoresist (i-line or g-line) was spun onto the sample and etched back using oxygen plasma to expose the SiO_2 on both sidewalls and nanopillar tops. A quick dip in buffered oxide etch (BOE) then removed this SiO_2 while the remaining resist protected the SiO_2 on the sample substrate. The photoresist was then stripped off the chip.

Subsequently, negative tone electron beam resist (ma-N 2410) was spun on the chip, exposed, and developed such that the remaining resist formed etch masks protecting individual nanopillars of interest. Sometimes two layers of ma-N 2410 were spun to ensure that nanopillars did not protrude from the resist, though the second spin often added only a fraction more resist thickness. In general, the e-beam steps used throughout this process flow follow the process detailed in Section 5.1. The sample was then dipped into BOE to remove the SiO_2 on the sample surface, leaving a ring of p-doped shell at the nanopillar base exposed for etching. A 1:1:30 H_2SO_4:H_2O_2:H_2O mixture then etched away the p-shell layer such that it became isolated from the leaky polycrystalline layers on the substrate.

Following this, the same steps taken in Chapter 5 were used to fabricate electrical contacts. A SiO_2 layer coated the nanopillar via plasma-enhanced chemical vapor deposition (PECVD) to electrically isolate the p-contact from the n-contact. Oxide thicknesses used ranged from 100 nm to 300 nm with no appreciable difference in impact on device performance as a detector. E-beam lithography with PMMA 495 A11 then defined nanopillar electrical contacts before evaporation of Ti/Au and subsequent lift-off.

It is evident that several additional steps were taken in fabricating nanopillar APDs when compared to nanopillar LEDs. The reason becomes apparent when comparing current-voltage (IV) characteristics for the two device processes. In Fig. 6.3, the IV curve for a nanopillar LED clearly indicates the presence of a leakage path. It looks like an ideal diode curve superimposed with a shunt resistance line. This shunt resistance is far less obvious for devices fabricated by etching into the p-shell of the nanopillar to break any direct contact between that layer and the polycrystalline film. The breakdown voltage is larger for nanopillar photodetectors versus LEDs, and both breakdown as well as turn-on transitions are sharper.

Electron beam as well as standard microfabrication techniques were used in making these devices. Electron beam lithography was required due to the present inability to control the site of nanopillar nucleation rather than the requirement for high-resolution lithography. In the future, practicality requires integration of APDs onto silicon with scalability and low fabrication cost. Thus, site-controlled growth will be critical for removing any reliance on expensive electron beam processes. Furthermore, site-controlled growth would enable parallel fabrication of arrays of APDs for many diverse applications. Nonetheless, this approach to integrating APDs onto Si opens a powerful path to optoelectronic integration via bottom-up nanomaterials synthesis.

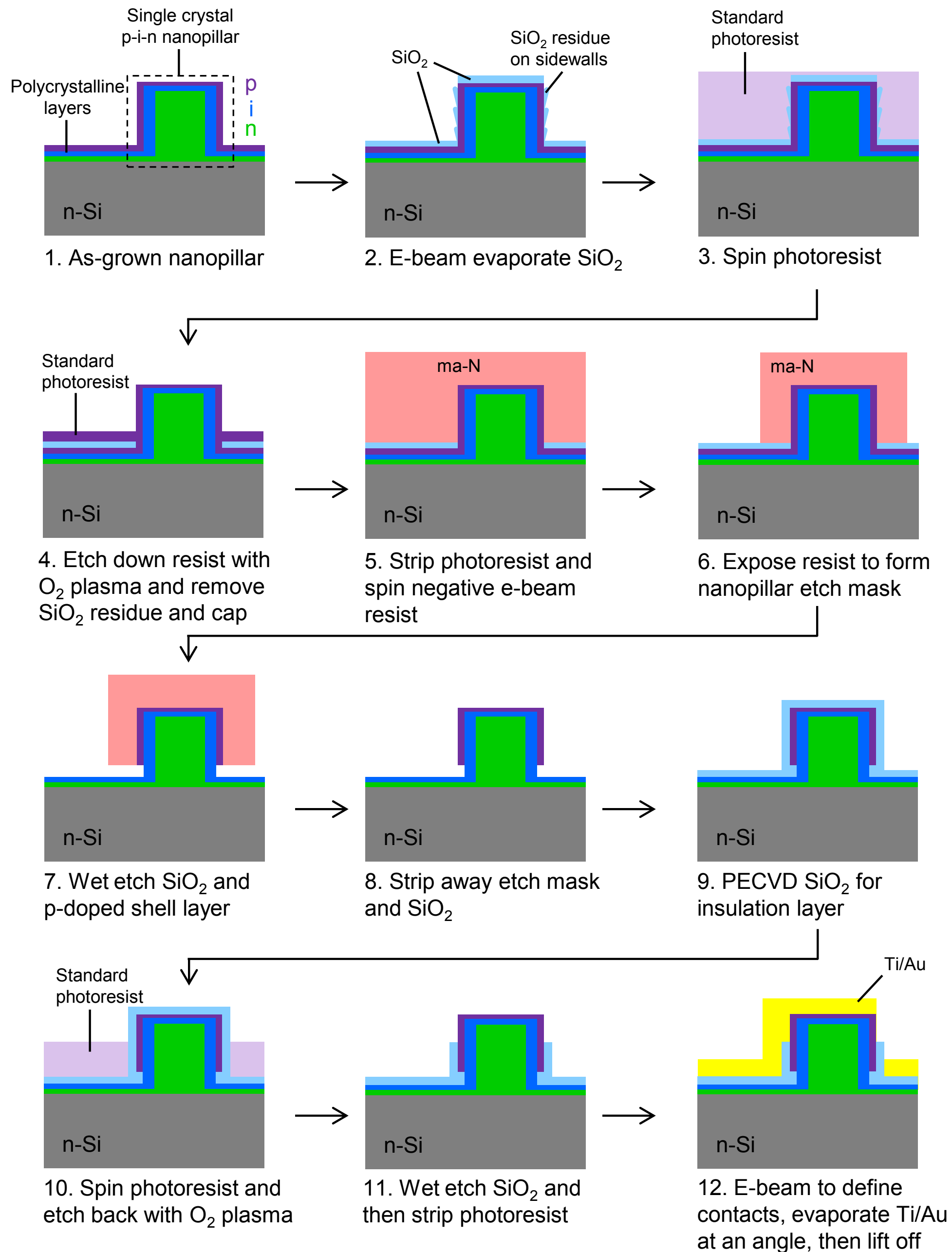

Figure 6.2 Fabrication process flow for nanopillar avalanche photodiodes. Additional details are discussed in the main body of text.

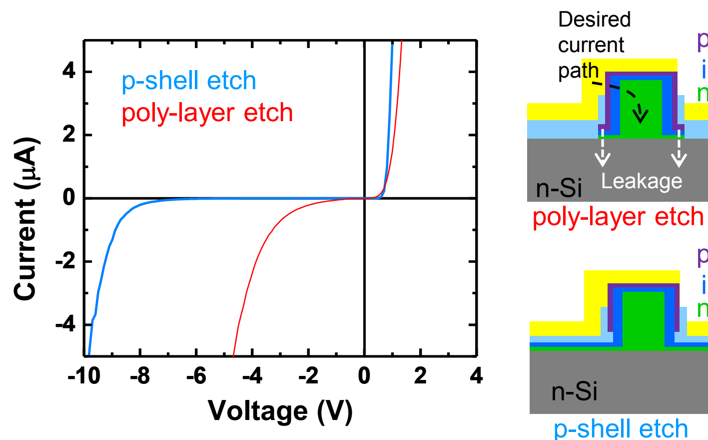

Figure 6.3 Improving diode performance. Etching away the p-shell reduces current leakage more than the poly-layer etch does. From the I-V plots shown, the poly-layer etch clearly results in a larger shunt path. Also, the p-shell etch method more reliably results in devices with ideality factors of 2.

6.2 Device testing

Figure 6.4a shows a top-view optical micrograph of a fabricated device, while its inset shows an SEM image. Both p- and n-type test pads were placed on the top side of the sample for high-speed probing as schematized in Fig. 6.4b. Notably, the negative probing pad must directly contact the n-Si substrate. Metallizing the i- and n-layers of the polycrystalline film to create the n-contact results in non-ohmic behavior, making proper characterization impossible.

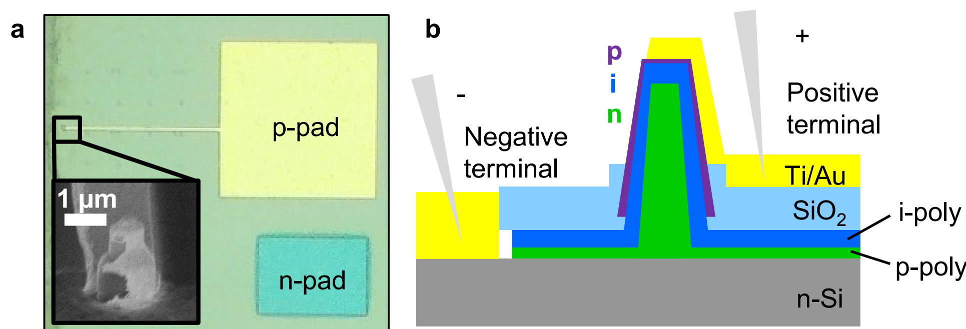

Figure 6.4 Nanopillar avalanche photodiode testing. a, An optical micrograph shows typical device contact and pad configuration. Two top-side test pads were used for high-speed testing. Note the n-pad was not yet metallized here. The inset shows an SEM image of a completed device. **b,** Various etching, lithography, and deposition techniques were used to fabricate nanopillar avalanche photodiodes. SiO_2 acts as electrical insulation between the p- and n-type layers.

Experimental setup

A relatively simple setup was built by using commercial equipment specialized for high-speed electrical testing. Figure 6.5 summarizes the major components of the apparatus. A high-speed probe contacting the device's pads connected the device to both a parameter analyzer and a digital communications analyzer via a bias tee. The parameter analyzer biased the APD and conducted DC characterization, while the DCA measured and analyzed pure RF signals. For large-signal modulation experiments, the DCA was triggered by the output of a pattern generator, which simultaneously drove a 10 GHz vertical-cavity surface-emitting laser (VCSEL). Free space optics guided and focused the laser source onto the normal-incidence APDs for photocurrent excitation. This configuration allowed large-signal response traces to be recorded. To measure device impulse responses, a 100 fs Ti:sapphire laser (850 nm, 80 MHz) replaced the VCSEL, and the fs laser's electronics controller triggered the DCA. For S_{21} measurements, the VCSEL and pattern generator were again used, but the DCA was replaced by a network analyzer. Section 6.4 shows and discusses the results of these experiments.

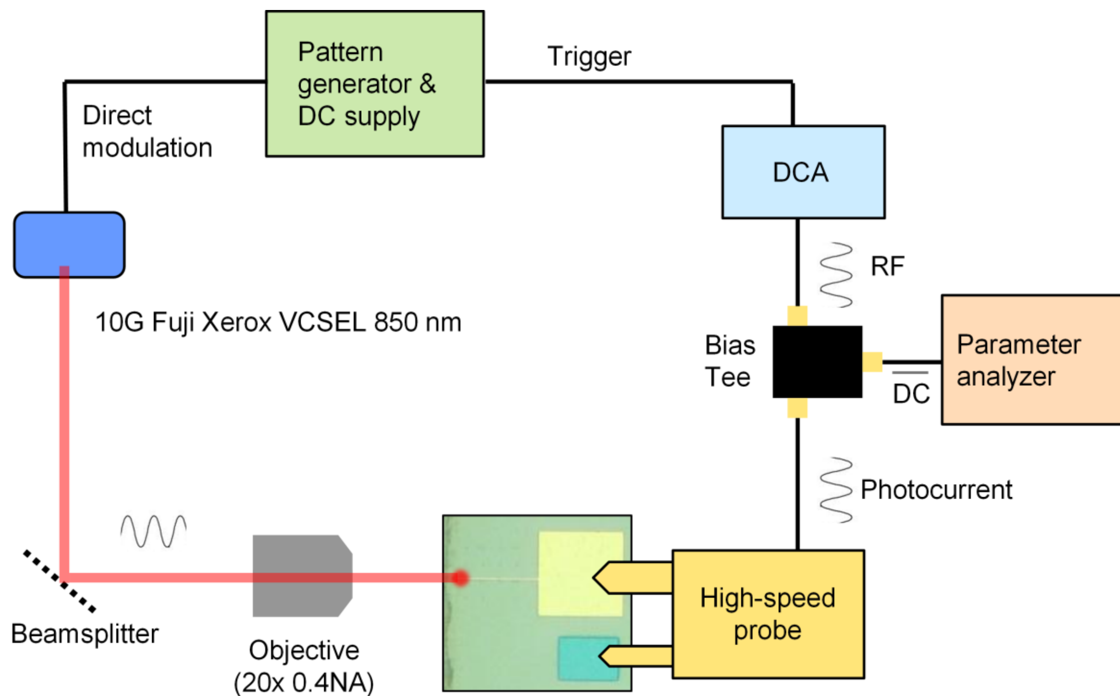

Figure 6.5 Experimental apparatus for testing high-speed avalanche photodiodes.

Light coupling

Because metal encapsulates most of the prototype APDs, coupling light into the device is difficult. However, device performance relies on knowing the amount of light coupled. Thus, proper analysis of performance necessitates proper understanding of light coupling. To do this, experiments were carefully modeled by finite-difference time-domain (FDTD) simulations using commercial software by Lumerical Solutions, Inc. The simulation focused a Gaussian beam onto a device model with a beam spot size equal to the experimental one (see Fig. 6.6). The device model itself had dimensions matching those of actual fabricated devices as measured by SEM. Power monitors in the simulation carefully measured the flow of power into, around, and out of the nanopillar active material. For the specific device shown in Fig. 6.1b, it was found that only 0.73% of incident light was absorbed by the nanopillar material. The vast majority of the light was either reflected by the metal or simply did not overlap with the device. This device showed particularly low light coupling since its optical window was especially small as shown in Fig. 6.1b. In the next section, analysis on avalanche multiplication data from this device takes this coupling factor into consideration. Similar FDTD simulations would have to be run for other devices and their unique dimensions to extract gain performance.

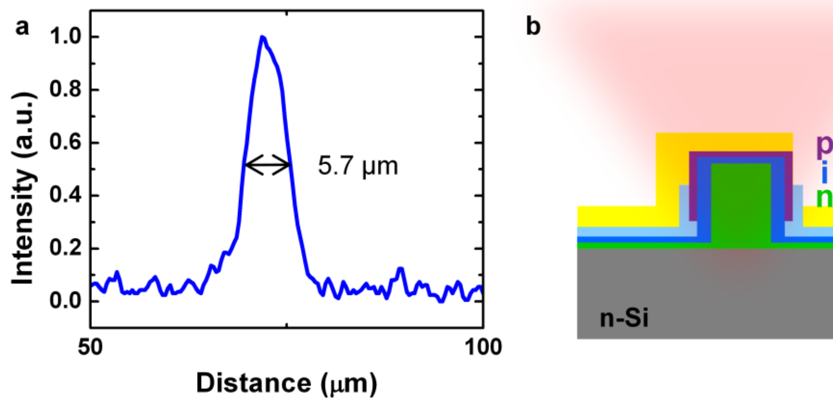

Figure 6.6 Light coupling into nanopillar avalanche photodiodes. a, The illumination beam spot was measured to help estimate light coupling into APDs. **b,** A schematic illustrates how metal inhibits light from coupling into APDs.

6.3 Avalanche gain

Nanopillar APDs possess attractive electrical characteristics. Figure 6.7a shows the IV curve of a device with dark current of only 1.2 pA and 45 nA at 0 V and -1 V, respectively. Some devices exhibit dark current as low as 1 nA at -4 V reverse bias and ideality factors of 2, testifying to the quality of the p-i-n heterojunctions grown inside the nanopillars. This type of diode performance suggests that nanomaterial quality can indeed approach the levels already achieved in epitaxial films after decades of careful

development. Photocurrent can be clearly seen when devices are under illumination as shown by the red curve in Fig. 6.7a. The device IV curve shifts upwards with respect to the dark IV trace. A clear photovoltaic effect is also seen with finite photocurrent apparent at 0 V and even under positive bias. Chapter 7 explores and discusses the photovoltaic behavior in greater detail.

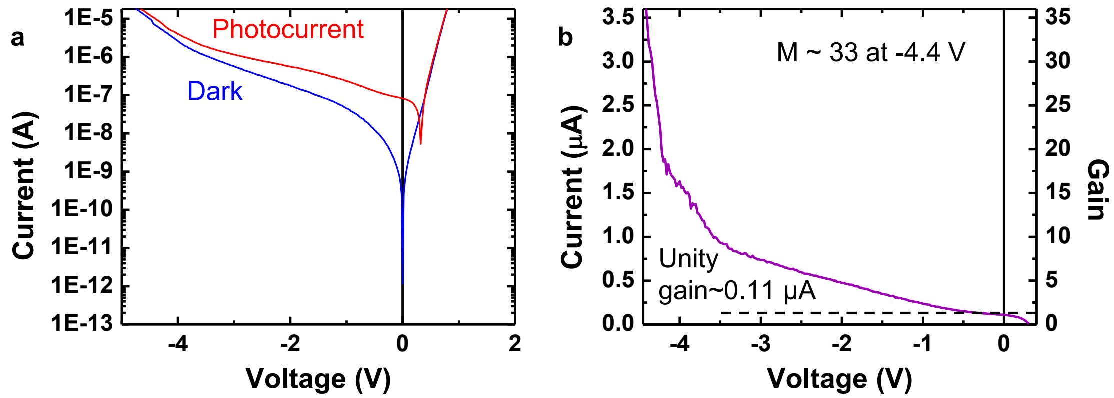

Figure 6.7 Avalanche gain. a. IV curves from devices with and without incident illumination show clear photocurrent (and also photovoltaic) effects owing to the high-quality radial p-i-n junctions grown. Dark current is low at 1.2 pA and 45 nA at 0 V and -1 V, respectively. **b,** Strong gain multiplication is observed with increasing reverse bias. At -4.4 V, a multiplication factor of 33 is reached.

Figure 6.7b shows the device's photocurrent versus bias voltage after subtracting dark current away. As reverse bias increases, photocurrent quickly sees amplification, which we attribute to avalanche gain [139]–[141]. The flat photovoltaic region around 0 V clearly defines a unity gain current of approximately 0.11 µA. Based on this value, multiplication reaches a gain of 33 at -4.4 V. At -4.5 V, the device reaches breakdown and photocurrent becomes erratic. Dark and illuminated IV curves subsequently collapse onto each other. Beyond the breakdown voltage, the APD becomes useless without proper circuitry to enable functionality in Geiger mode [142].

For this particular device, the unity gain responsivity was a modest 0.15 A/W though it reaches 4.9 A/W at -4.4 V. Due to variation between grown nanopillars, unity gain responsivity of our photodetectors ranges from 0.15 A/W to 0.6 A/W. It is worth noting that the wavelengths (850 nm) used in our experiments limits responsivity to a maximum of 0.68 A/W. With improved growth uniformity and long wavelength operation, unity gain responsivity approaching 1 A/W is entirely possible.

Notably, avalanching begins at relatively low voltages. A couple factors may explain this phenomenon. First, it is well known that low bias voltages can create very large electric fields if the junction size is small, and our p-i-n junction's intrinsic region is typically only 200 nm thick. Second, the unique core-shell p-i-n junction configuration

subjects the junction to possible electric field enhancement due to junction curvature effects [143]. For sufficiently small radii of curvature, electric fields bunch together in a manner analogous to the lightning rod effect [144]. Uncertainty still surrounds the latter mechanism behind avalanching at low bias. Future work will focus on studying this effect and exploring the possibility of engineering it to boost APD performance. Regardless of whether enhanced electric fields in our core-shell junction exist, one advantage of the core-shell geometry is clear. It is effectively a planar APD rolled up and integrated onto a silicon substrate with tiny footprints.

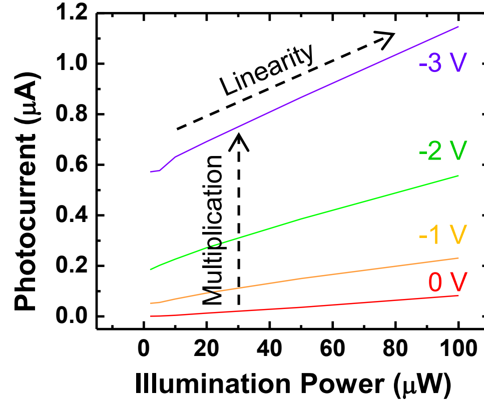

Figure 6.8 Avalanche photodiode linearity. The linearity of nanopillar APDs supports that increase in photocurrent is not due to thermally activated diffusion or similar processes.

It is worthwhile to briefly discuss our attribution of gain to avalanche multiplication. After all, other gain mechanisms exist including photoconductor and phototransistor gain [139]. Reference [52] shows that while these gain mechanisms may contribute slightly at lower bias voltages, avalanche multiplication dominates as bias increases. Also, sometimes what appears to be photocurrent gain is in fact not gain at all. For example, it is possible that increasing reverse bias may lower an existing barrier that limits current flow in a device. As a result, photocurrent increases as barrier height reduces. In this case, increase in photocurrent is actually photocurrent approaching its unity gain value rather than multiplying beyond unity gain. Figure 6.8 shows that nanopillar APDs are extremely linear at all bias levels, suggesting that this effect does not cause the observed amplification. If processes like thermally-activated diffusion dominated, photocurrent should increase versus illumination in a nonlinear fashion. Furthermore, we know that the metal-semiconductor interface for our devices features an ohmic contact and no significant barriers exist there. Otherwise, we would not observe any significant photocurrent under zero bias as shown in Fig. 6.7.

6.4 High-speed operation

It is not only amplification, but also high-speed operation that makes APDs attractive for applications including, but not limited to, communications. For APDs, a tradeoff exists between gain and bandwidth, thereby making gain-bandwidth product the most appropriate figure of merit. In order to measure the bandwidth of nanopillar APDs, S_{21} measurements were performed. A directly modulated 850 nm VCSEL was used as the light source for these experiments. Figure 6.9a shows the S_{21} response curve for the same device whose multiplication data is displayed in Fig. 6.7. The bandwidth for this device is 3.1 GHz, meaning a 102 GHz gain-bandwidth product is achieved at a bias voltage of -4.4 V. Nanopillar APD bandwidths as high as 3.6 GHz have been measured (Fig. 6.9b), but 102 GHz has been the largest gain-bandwidth product achieved thus far.

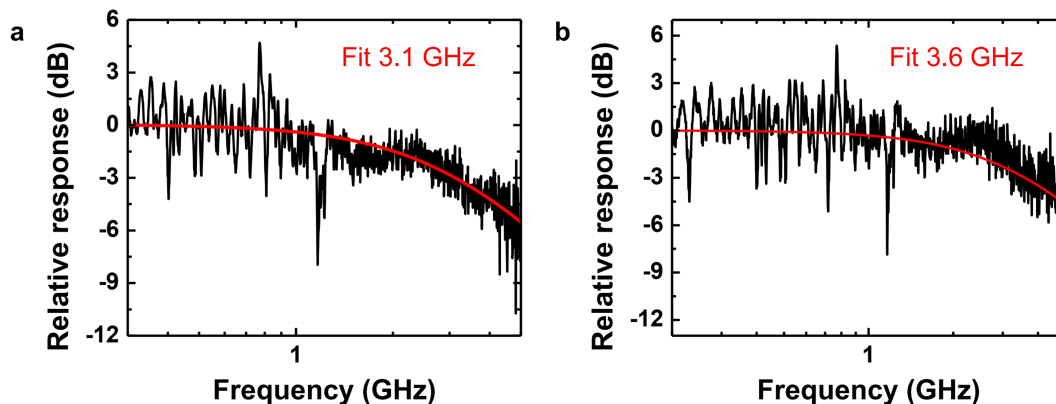

Figure 6.9 S_{21} measurements of nanopillar avalanche photodiodes. S_{21} measurements show that nanopillar APDs can indeed operate at high bandwidths. **a,** The device exhibiting a gain of 33 in Fig. 6.7 also shows a bandwidth of 3.1 GHz. That device thus features >100 GHz in gain-bandwidth product. **b,** Even faster devices have been measured as suggested by the 3.6 GHz response seen here.

For our present APD design, diffusion processes limit device bandwidth. In particular, absorption in the doped layers of nanopillars generates carriers that must first undergo diffusion before reaching the high-field region [145]. Other diffusion capacitance effects might also exist. This can be seen in Fig. 6.10, which shows an APD impulse response featuring a prominent diffusion tail. Rise times as fast as 33 ps (Fig. 6.11a) have been observed for APD impulse responses, implying over 10 GHz operation should be possible if the diffusion tail is minimized. Notably, 3 dB bandwidths measured from S21 curves show no noticeable change versus gain (or bias voltage) as shown in Fig. 6.11b. It is likely that diffusion effects have created a ceiling on the high-speed performance of present nanopillar APDs. Proper optimization of the junction layers and their characteristics such as doping level should greatly reduce this diffusion-related barrier [146]–[148]. Additionally, we have neglected possible parasitics in the contacts

and experimental setup. Identifying and removing any parasitics may increase bandwidth even further. Based on these expectations and already-existing data, gain-bandwidth products around 300 GHz should be well within reach as suggested by Fig. 6.11b.

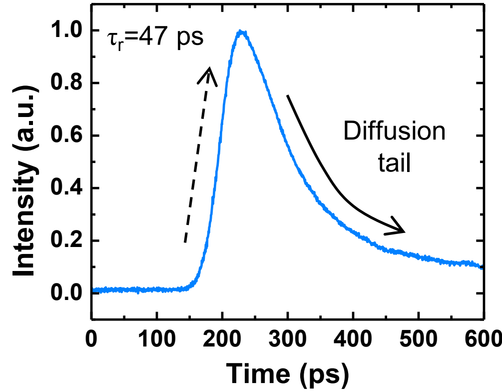

Figure 6.10 Avalanche photodiode impulse response. S_{21} bandwidths fall short of expected bandwidths based on device impulse responses because of the presence of a tail as shown. Future improvement in bandwidth will require understanding and eliminating this tail.

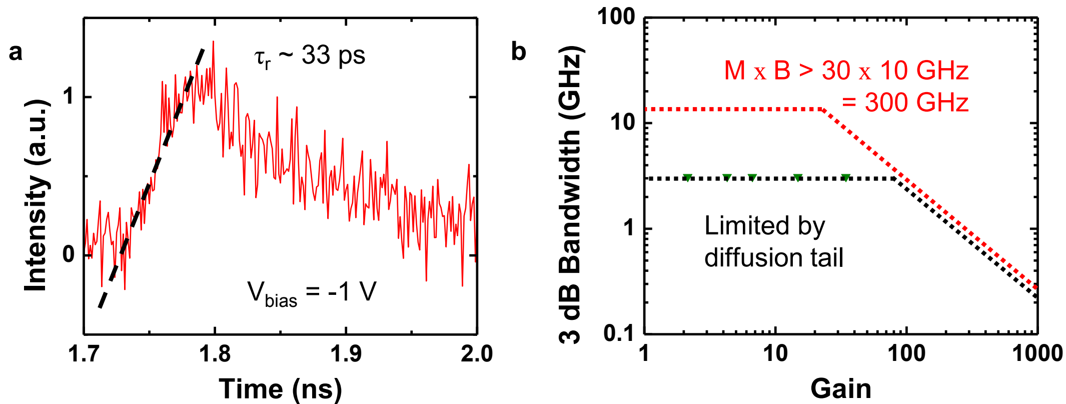

Figure 6.11 Limitations in avalanche photodiode speed. a, Rise times as fast as 33 ps have been measured, implying >10 GHz operation should be attainable. **b,** The 3 dB bandwidth for devices does not change for higher bias voltages. This is likely a consequence of the gain-bandwidth product being limited by a diffusion tail.

In order to substantiate this relatively bold claim, we refer to additional data indicating that diffusion does indeed limit present device performance. Figure 6.12a shows a set of normalized impulse responses for an APD under various bias levels ranging from 0 V to -4 V. It is evident that the rise time τ_r increases slightly with

increasing bias. Employing (6.1), we can plot the expected bias-dependent device bandwidth as in Fig. 6.12b, which clearly increases from 6.2 GHz at 0 V to 7.6 GHz at -3 V before dropping off slightly at -4 V. The reason this is not reflected in the S21 measurements comes from the fact that Equation (6.1) is valid for symmetrical impulse responses. That is, it reflects the 3 dB bandwidth if the fall time τ_f of the impulse response equals the rise time τ_r. Figure 6.12a instead shows that τ_f is much longer than τ_r and does not change with bias. Hence, the true 3 dB bandwidth as measured through S21 experiments remains constant versus bias.

$$f_{3dB} = \frac{0.35}{\tau_r} \tag{6.1}$$

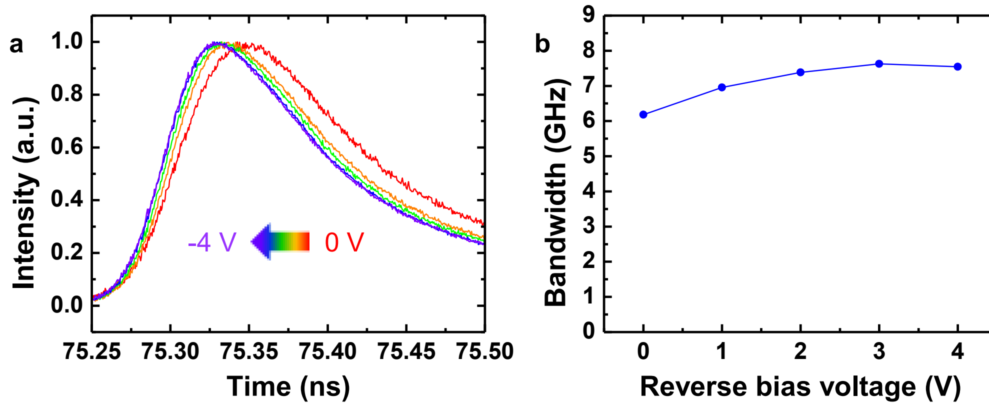

Figure 6.12 Avalanche photodiode rise times. a, While the S_{21} bandwidth does not change with bias, the rise time of the impulses response does. **b,** This implies that bandwidth does indeed depend on bias, but it is presently limited by the diffusion tail. The bandwidth values plotted are what is expected using equation (6.1).

Ultimately, avalanche photodiodes must be able to clearly detect optical signals at a high rate, especially for communications applications. Large-signal modulation experiments were thus performed on the nanopillar APDs. A train of VCSEL laser pulses was delivered with various data rates and patterns, and averaged as well as unaveraged APD response was recorded. Figure 6.13 shows an averaged detector response to a 4.6 GHz on-off signal train. It is evident that the detector can clearly resolve the large signal modulations even at this data rate, which exceeds the device's 3 dB bandwidth.

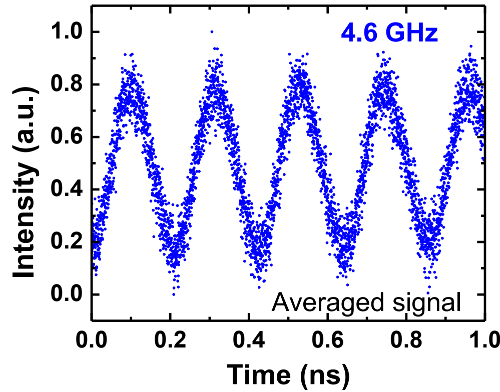

Figure 6.13 Averaged large signal detection. Large-signal modulation of a 850 nm VCSEL can be clearly detected by nanopillar-based APDs. Here, on/off signals with periodicity <0.3 ns are observed. Averaging was used for this measurement. Light coupling and SNR must be improved in the future to demonstrate open eye diagrams.

In most applications, averaging is not practical. Thus, the unaveraged response of the photodetector is even more important to characterize. In Fig. 6.14, the unaveraged response of a nanopillar APD clearly replicates a 1 Gbps incident stream of data with the bit pattern '1100100'. It does so with fairly respectable performance for a first-generation prototype of a new nanomaterial-based APD. The corresponding SNR is 15 dB, and the Q factor is 2.8. Better SNR is presently inhibited by poor light coupling into the device, which can also cause significant heating of the device's local environment. Engineering better detection apertures in the future will improve coupling efficiency into the active material and minimize detrimental thermal effects. The possibility of waveguide coupling may be explored as well for on-chip optical interconnect applications, though many other applications exist beyond interconnects. Certainly, a goal going forward will be successfully demonstrating open eye diagrams with nanopillar-based APDs.

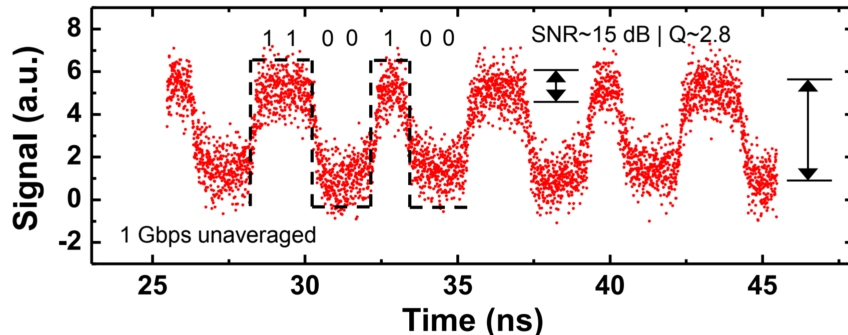

Figure 6.14 Unaveraged large signal detection. Practicality requires unaveraged large signal detection, which we show here. For a first-generation

device, nanopillar APDs demonstrate respectable performance with a SNR of 15 dB and *Q* of 2.8. The bit stream detected was '1100100' as labeled.

6.5 Summary and outlook

In conclusion, we have demonstrated a new way to integrate III-V avalanche photodiodes onto silicon. III-V nanopillar materials are monolithically grown under CMOS-compatible conditions, so these devices are ideal for back-end-of-line integration of optoelectronics. Additionally, this work reflects how bottom-up nanomaterials are closing the performance gap with top-down bulk materials. The performance of nanopillar-based photodetectors already approaches that of present state-of-the-art avalanche photodiodes even without careful device modeling and design. This first generation of nanopillar photodetectors has thus far exhibited bandwidths >3 GHz and multiplication factors reaching 33.

Some remaining challenges face this approach to realizing on-chip photodetectors for silicon photonics. First, waveguide coupling of these devices must be achieved. Additionally, they must operate at Si transparent wavelengths, though prior work in our group suggests that this is already within reach [97]. The physics of avalanche gain in a radial core-shell p-i-n junction should be studied further, and noise properties ought to be characterized. Finally, proper design of devices is needed to remove parasitics and maximize performance, as we expect these nanostructures to achieve hundreds of GHz in gain-bandwidth product upon doing so. Having already enabled several key optoelectronic devices and functionalities, nanopillars are poised to implement full optical links on Si in the future [98], [125], [149]. They may even become useful for more exotic applications such as retinal prosthesis and integrated chip-scale LIDAR [17], [150], [151].

Chapter 7

Photovoltaic effects

The economics of solar power generation is of utmost importance when deciding what approach to take with photovoltaics. However, we save this discussion for another time and focus solely on exploring the physics of the photovoltaic effect in a new nanomaterial. Chapter 7 briefly explores the photovoltaic effect in III-V nanopillars on silicon. As will be shown, photovoltaic effects are clearly observed from nanopillar-based devices, meaning nanopillars can provide the three primary capabilities of optoelectronics: light emission, light photoconductivity, and light-electricity energy conversion.

7.1 Nanotechnology and solar cells

In recent years, the fields of photovoltaics (PV) and nanoscience have undergone rapid growth in a parallel fashion, motivating exploration of potential synergy between the two. Some have studied nanostructured materials for enhanced current extraction and absorption efficiency [152]–[154], while others have sought to combine solar power generation with plasmonic enhancement [80]. Additionally, progress has been achieved towards integrating various nanomaterials for building multi-junction or tandem solar cells [155], [156]. Possible solar cell materials include silicon, III-V compounds, polymers, and even more exotic ones like carbon nanotubes [157]–[159].

7.2 Photovoltaic effects in III-V nanopillars on silicon

Using III-V nanostructures as solar cell materials has attracted much attention because of superior optical properties in III-V systems, potential for improved carrier collection with radial p-n junctions, and cost benefits similar to thin-film approaches. Photovoltaic effects have already been demonstrated in III-V core-shell nanowires (NWs) on Si substrates [160], [161]. However, III-V wafers are expensive, so integrating thin films of III-V nanomaterials onto alternative substrates remains an attractive approach. Motivated by this, we investigated the feasibility of using nanopillars on silicon for photovoltaics. Though this dissertation has thus far focused on devices built on silicon, nanopillar growth can also be extended to other substrates including low-cost polysilicon. Figures 7.1a,b show SEM images of nanopillars grown on silicon and polysilicon, respectively.

Notably, growth on polysilicon yields a highly dense film of nanopillars, which is actually quite fortuitous from a solar cell perspective. The challenge then becomes manufacturing large area solar cells since the randomized orientation and interleaving of nanopillars on polysilicon make electrical contacts difficult to fabricate. Thus, it is useful to first fabricate and characterize a photovoltaic device based on a single nanopillar on Si.

Earlier chapters demonstrated several nanopillar-based optoelectronic devices on silicon including lasers, light-emitting diodes, and avalanche photodetectors, suggesting that nanopillars may also be well-suited for PV applications [125], [149]. The ability to control doping, material composition, and core-shell growth has enabled creation of the superior junctions and heterostructures needed for such devices [97], [125]. These traits are similarly required for high-performance solar cells.

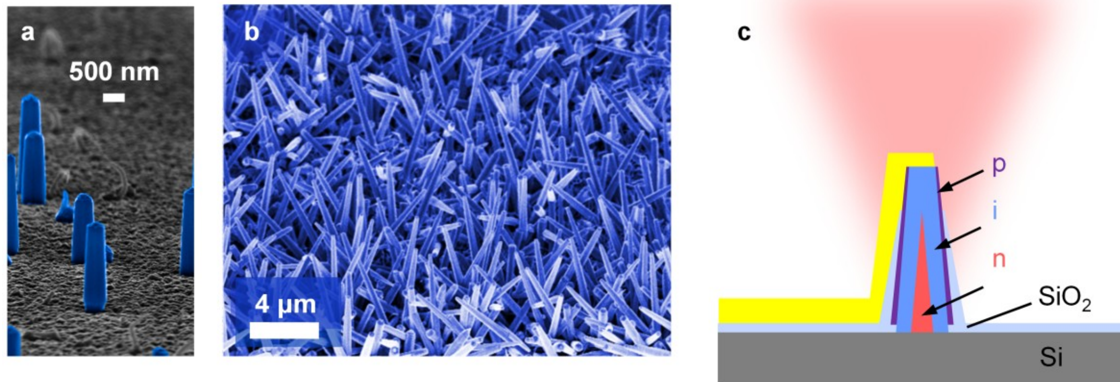

Figure 7.1 Using nanopillars as photovoltaic materials. Scanning electron microscope (SEM) images of nanopillars grown on **a,** (111) silicon and **b,** polycrystalline silicon. Nanopillar growth on lattice-mismatched substrates has proven to be a versatile technology, allowing III-V integration on different types of silicon, GaAs, and even sapphire substrates. **c,** A schematic of a nanopillar-based photovoltaic device.

A schematic in Fig. 7.1c illustrates the device characterized for photovoltaic effects. It is effectively the same device as the avalanche photodiode shown in 0, though small variations exist from sample to sample. Device fabrication steps are similar to those already described for avalanche photodiodes. As shown in Fig. 7.2, textbook IV curves are achieved by nanopillar diodes with low turn-on voltages of approximately 1 V. Under reverse bias, the dark current is only around 0.3 nA at -3 V, which is quite respectable for a GaAs-based diode. In Fig. 7.2, the dark current at 0 V is limited by the noise floor of our instruments. From other experiments as seen in Section 6.3, the dark current is expected to be on the order of a pA or less. Typical nanopillar diodes exhibit ideality factors as low as 2 as highlighted in Fig. 7.2, which is comparable to ideality factors for planar devices, further testifying to the quality of our radial p-n junctions. It should be

noted that for these experiments, as-grown nanopillars on silicon were processed without mechanically removing them from their original silicon substrates.

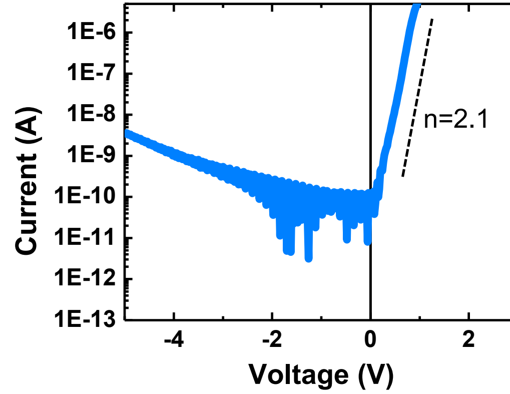

Figure 7.2 Low ideality and dark current. Photovoltaic devices exhibit a nearly ideal ideality factor as low as 2.1

Preliminary solar cell experiments were performed using a 633 nm continuous wave (CW) laser beam focused onto a single nanopillar device using a 100x 0.7 NA objective. Based on solid angle considerations and objective lens insertion loss, we estimate that ~3.7% of incident illumination couples into the nanopillar since it is mostly clad with reflecting metal. In Fig. 7.3, IV curves under different levels of illumination reveal promising PV effects in our nanopillars. The fill factor (FF) remains fairly constant at 61% under various powers, which compares well to the highest reported value of 65% for nanowire systems [160]. From Fig. 7.4a, we observe that the open-circuit voltage increases towards ~0.8 V under concentrated light following:

$$V_{oc}^{'} = V_{oc} + nkT\ln(X)/q \qquad (7.1)$$

This is a promising value for a material with a band gap of 1.24 eV. Meanwhile, the short-circuit current increases linearly with illumination power as shown in Fig. 7.4b. These preliminary results correspond to a power conversion efficiency of ~53% under high concentration, which begins to approach the theoretical limit for 633 nm monochromatic illumination [162]. Thus, III-V nanopillars on silicon offer potential for high efficiency while perhaps also affording cost advantages similar to thin film approaches. Future challenges facing this approach include realization of large-area solar cells with high nanopillar density as well as improvement of material properties for higher open-circuit voltage and efficiency. Going forward, characterization using AM 1.5 illumination at 1 sun will be required.

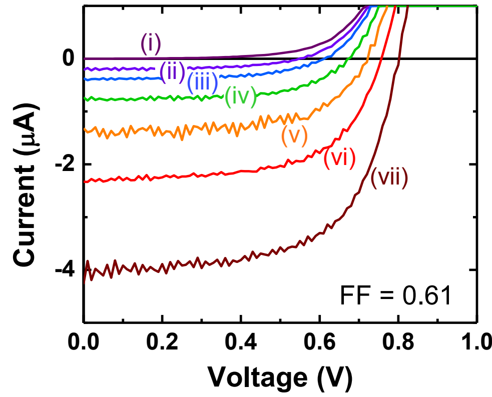

Figure 7.3 Promising photovoltaic effects observed in nanopillars on silicon. Solar energy generation can be clearly seen from IV curves under illumination at (i) 0 μW, (ii) 5 μW, (iii) 10 μW, (iv) 20 μW, (v) 40 μW, (vi) 50 μW and (vii) 100 μW. The fill factor remains fairly constant at 61% for all illumination intensities.

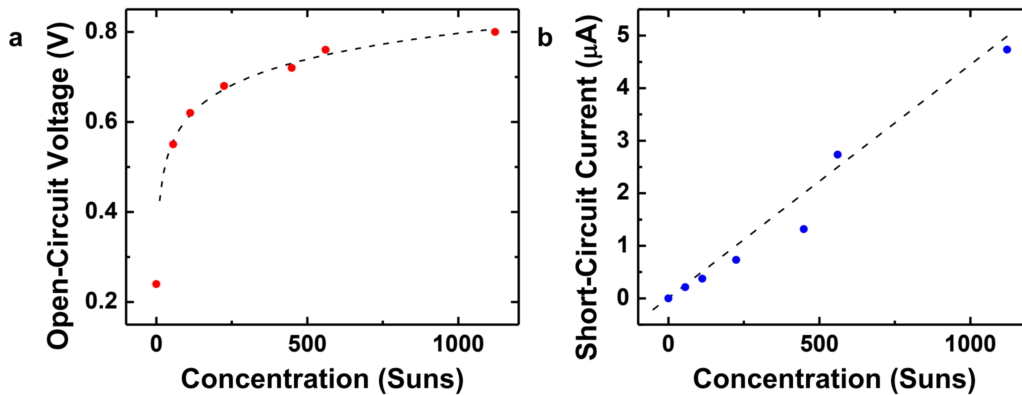

Figure 7.4 Photovoltaic performance under concentration. a, The open-circuit voltage, however, increases in a logarithmic fashion and approaches a respectable 0.8 V. The dashed black line is a fit using equation (7.1) for n=3.2, T=300, and V_{oc}=0.223 V. k, q, and X are the Boltzmann constant, electron charge, and concentration (unit 1 kW/m^2), respectively. **b,** The short-circuit current versus illumination follows a linear slope as expected.

Chapter 8

Nonlinear optics

Thus far, this dissertation has shown how nanoneedles and nanopillars on silicon can implement the entire gamut of optoelectronic devices, including lasers, light-emitting diodes, photodetectors, and even photovoltaic devices. However, another dimension in photonic functionality has yet to be explored. Semiconductor nanomaterials can also feature nonlinear optical generation. In this chapter, we explore the potential of nanoneedle-based materials for the field of nonlinear optics.

8.1 Second-harmonic generation

In this section, we report and characterize second-harmonic generation from a single wurtzite GaAs nanoneedle. The wurtzite crystal structure of the nanoneedle relaxes the strict nonlinear selection rules of normal zincblende GaAs while maintaining its strong nonlinear optical coefficients. The ability to grow GaAs nanoneedles without catalysts on (111) Si makes them particularly attractive as nonlinear optoelectronic media compatible with complementary metal-oxide-semiconductor technology.

Nonlinear optical properties of semiconductor nanostructures are of great interest for basic material research and potential applications using sum, difference, and harmonic generation. ZnO and GaN nanowire systems have recently shown promise for nonlinear optical conversion [163]–[165]. Coupling of second-harmonic generation (SHG) into whispering gallery modes has been reported, and near-field scanning optical microscopy using SHG from a single potassium niobate nanowire has been achieved [166], [167]. Recently, we demonstrated catalyst-free, low-temperature growth of single crystalline wurtzite (WZ) GaAs nanoneedles with atomically sharp tips on Si [53]. Unlike GaAs in its typical zincblende (ZB) phase, WZ-GaAs is bifringent and possesses 6mm point group symmetry, which imposes much less restrictive nonlinear susceptibility selection rules. The ability to grow nanoneedles at low temperature without metal catalysts on Si thereby makes them highly attractive as nonlinear media for optoelectronic compatibility with complementary metal-oxide-semiconductor (CMOS) technology. In this letter, we characterize strong second-harmonic generation from this material.

The GaAs nanoneedles used in this experiment were grown by low-pressure metal-organic chemical vapor deposition (MOCVD) at low temperatures between 380-410 ºC.

They assemble without metal catalysts on (111) Si into pyramidal structures with hexagonal cross-sections and 6-9º sidewall tapers. Because they do not require metal catalysts, nanoneedles have an important advantage over nanowires for III-V integration onto Si for CMOS. Figure 8.1 presents false-color top-view and 30º tilt-view scanning electron microscope (SEM) images of a single nanoneedle. The six facets of its predominantly hexagonal cross-section are visible. Transmission electron microscopy has meanwhile shown nanoneedles to grow in single crystal wurtzite phase with tips as narrow as 2-4 nm [53]. These nanostructures grow vertically along the crystalline c-axis. Since the size of nanoneedles scales with growth time, ~9 μm long nanoneedles with ~1.5 μm base diameters were grown for the second-harmonic experiments under consideration. The nanoneedles were subsequently mechanically wiped onto a double-side polished sapphire substrate to facilitate polarization dependence measurements.

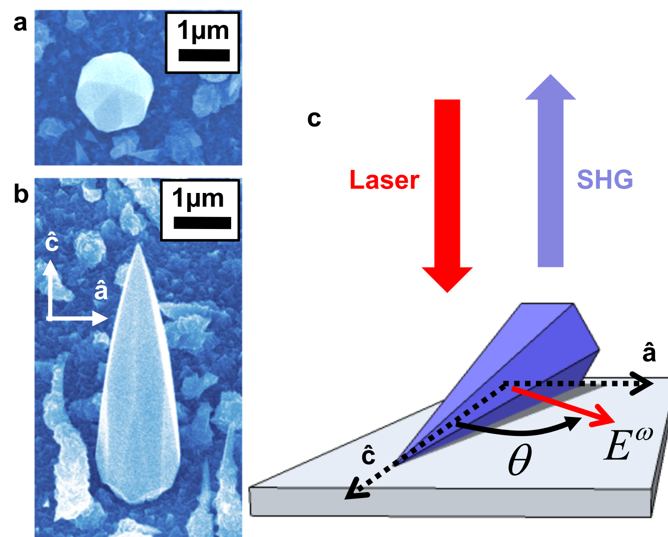

Figure 8.1. GaAs nanoneedles for second harmonic generation. Scanning electron microscope images of a wurtzite GaAs nanoneedle **a,** from surface normal planar view and **b,** 30°-tilt view. The crystal c-axis lies along the longitudinal growth direction of the nanoneedle. The a-axis is in the transverse direction. **c,** Schematic detailing measurement conditions. The nanoneedle rests horizontally on a double-side polished sapphire substrate. θ is the angle between the laser's polarization and the nanoneedle c-axis.

8.1.1 Observations of frequency doubling

The experimental apparatus used for characterizing second-harmonic generation from nanoneedles is shown in Fig. 8.2. High-peak power 120 fs pulses from a Ti-sapphire laser at ~806 nm with a 76 MHz repetition rate excite second-harmonic light from nanoneedles at 300 K. A 100x 0.70NA objective focuses the laser beam to a ~1 μm spot and collects back-generated second-harmonic emission in reflection mode. The laser light strikes a nanoneedle with nearly normal incidence on one of its six facets. As shown in Fig. 8.1c,

the nanoneedle lies flat on a double-side polished sapphire substrate. In this configuration, the c- and a-axes both lie in a plane normal to the direction of laser incidence. This facilitates the polarization dependence measurements to be discussed later. For spectral measurements, a 492 nm short-pass filter allows only SHG to reach a spectrometer and LN_2-cooled Si CCD detector. A polarizer placed before the entrance slit of the spectrometer controls which second-harmonic polarization is measured, while a half-wave plate in conjunction with a polarizer at the laser output controls the polarization of the incident laser. Figure 8.3 shows the SHG spectrum from a single nanoneedle for both fundamental and second-harmonic light polarized parallel to the nanoneedle's c-axis. As expected, the SHG is centered at ~403 nm or twice the fundamental frequency. The bandwidth of the second-harmonic generation is due to the bandwidth of the excitation pulses. The tails of the second-harmonic spectrum fall off more rapidly than those of the incident laser's spectrum because of the nonlinear power dependence of SHG. Indeed, the power dependence of the integrated second-harmonic intensity fits a slope of 2 when plotted on a log-log scale as shown in Fig. 8.4. The quadratic power dependence confirms the second-order nature of the light emission.

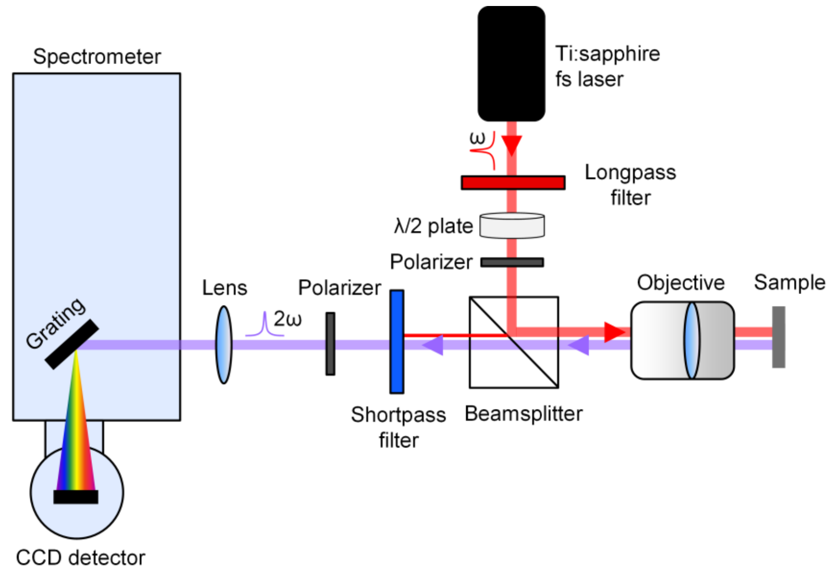

Figure 8.2 Experimental setup for characterizing second-harmonic generation.

Various mechanisms of second-harmonic generation from GaAs have been reported in literature. SHG from bulk GaAs has been shown for the material in its zincblende phase, though the cubic symmetry of ZB-GaAs makes SHG difficult to observe in that case [168], [169]. Surface SHG due to symmetry breaking at the crystal interfaces has also been characterized [170], and various methods to enhance both surface as well as bulk SHG have been reported [171]–[175]. However, high efficiency SHG and collection in GaAs remains challenging.

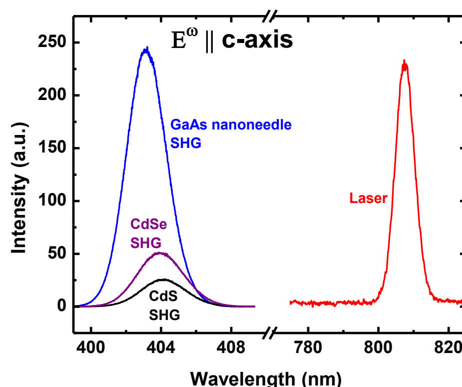

Figure 8.3 Laser and SHG spectra. Both fundamental and second-harmonic fields are polarized along the nanoneedle's c-axis. The bandwidth of the SHG spectra represents the bandwidth of the 120 fs pulses at 806 nm used for excitation. Nonlinear optical coefficients are estimated for WZ-GaAs by comparing the intensity of SHG from a single nanoneedle to SHG from reference CdSe and CdS wafers.

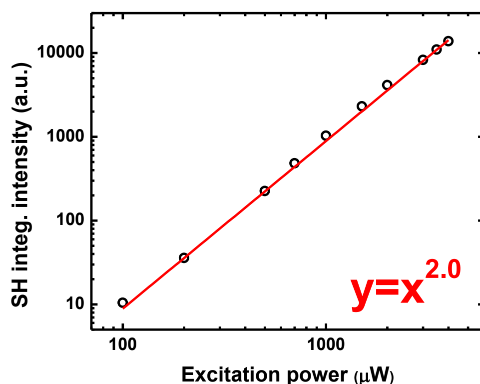

Figure 8.4. Power dependence second-harmonic generation. The data plotted on a log-log scale fits a slope of 2 and thereby follows a quadratic power dependence, confirming the second-order nature of the emitted light.

8.1.2 Polarization dependence

In order to investigate the origin of second-harmonic generation from a nanoneedle, a series of polarization dependence measurements have been performed. A confocal microscope using a photomultiplier tube as the detector has been employed for this measurement. As the nanoneedle is single crystalline and wurtzite [53], bulk SHG from the nanoneedle should follow the selection rules dictated by the 6mm point group second-

order susceptibility tensor. For a second-harmonic polarization field polarized along the c-axis of the nanoneedle, the following fundamental electric field polarization dependence is thereby expected:

$$I_{SHG,c} \propto [\cos(\theta)^4 (\chi^{(2)}_{ccc})^2 + \sin(\theta)^4 (\chi^{(2)}_{caa})^2] I^2_{fundamental} \qquad (8.1)$$

I is light intensity, while $\chi^{(2)}$ is a second-order nonlinear tensor element. The first subscript of $\chi^{(2)}$ denotes the second-harmonic polarization direction while the latter two denote the polarization directions of the interacting fundamental electric fields. The angle θ is defined as the angle between the laser's field polarization and the c-axis of the nanoneedle as indicated in Fig. 8.1c. The $\chi^{(2)}_{ccc}$ and $\chi^{(2)}_{caa}$ terms contribute to SHG polarized along the crystalline c-axis. Only $\chi^{(2)}_{ccc}$ contributes at 0° and 180° while only $\chi^{(2)}_{caa}$ contributes at 90° and 270°. A periodicity of 180° in the polarization dependence thereby results. The maxima and minima of the polarization dependence and their ratio then depend on the relative strength of the two contributing tensor elements and their ratio, respectively. Experimental results for SHG polarized along the nanoneedle in Fig. 8.5a show that $\chi^{(2)}_{ccc}$ must be significantly larger than $\chi^{(2)}_{caa}$. The theoretical curve (solid blue line) fits the measured data (blue circles) precisely, where the ratio of the tensor element values has been treated as the fitting parameter. The ratio of the maxima to the minima of this polarization dependence is typically about 20 to 1.

For the second-harmonic polarization field polarized along the nanoneedle's a-axis, the fundamental field polarization dependence should follow:

$$I_{SHG,a} \propto \sin(\theta)^2 \cos(\theta)^2 (\chi^{(2)}_{aca})^2 I^2_{fundamental} \qquad (8.2)$$

The only contribution to a second-harmonic field along the a-axis is the $\chi^{(2)}_{aca}$ tensor element. In this case, a periodicity of 90° is expected, with maxima at 45°, 135°, 225°, and 315°. Indeed, Fig. 8.5b shows that the measured SHG polarized across the nanoneedle follows the theoretical polarization dependence expected for SHG from a bulk wurtzite material. After averaging the polarization dependence of several nanoneedles, we extract ratios of $\chi^{(2)}_{ccc} : \chi^{(2)}_{aca} : \chi^{(2)}_{caa} \sim 4.4 : 2 : 1$, which are similar to ratios reported in other wurtzite crystals such as CdSe [176]. These results strongly indicate that the SHG seen in the GaAs nanoneedles largely originates from the bulk. While surface SHG may have some contribution, the overwhelming agreement of the second-harmonic polarization dependence with the bulk selection rules for wurtzite crystals shows that bulk generation is by far the dominant effect. Furthermore, the measured polarization dependence is strong testimony that the nanoneedle is single crystalline wurtzite throughout the nanostructure without any type of zincblende twinning. Otherwise, surface

and zincblende contributions would smear the clearly wurtzite nature of SHG from a single nanoneedle.

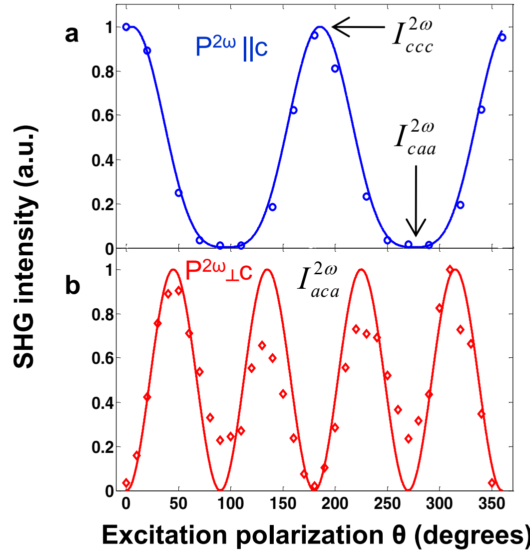

Figure 8.5. Polarization dependence of second-harmonic generation. Blue circles and red diamonds show experimental excitation polarization dependence data for SHG polarized ∥c-axis and ⊥c-axis, respectively. Solid lines show the respective theoretical fits. Relative intensity scales are arbitrary. **a,** Fundamental field polarization dependence of second-harmonic generation polarized along a single nanoneedle's c-axis. $\chi^{(2)}_{ccc}$ and $\chi^{(2)}_{caa}$ contribute to this second-harmonic polarization. Maxima occur at 0°, 180°, and 360°, revealing that $\chi^{(2)}_{ccc}$ is the stronger tensor element. The ratio between the maximum and minimum second-harmonic intensity is typically about 20:1. **b,** Fundamental field polarization dependence of second-harmonic generation polarized along a single nanoneedle's a-axis. For second-harmonic light polarized transverse to the nanoneedle, the only nonzero tensor element is $\chi^{(2)}_{aca}$. Thus, maxima are expected at 45°, 135°, 225°, and 315° as shown by the experimental data. From these measurements, the ratios of the tensor elements are estimated to be $\chi^{(2)}_{ccc} : \chi^{(2)}_{aca} : \chi^{(2)}_{caa} \sim 4.4 : 2 : 1$.

8.1.3 Second-harmonic Fresnel coefficients

We estimate the nonlinear coefficients of wurtzite GaAs nanoneedles by comparing their SHG signals with those from other wurtzite crystals, i.e. CdS and CdSe, while using their reported nonlinear coefficients as references [176], [177]. Identical experimental conditions were used so that the ratios of the intensities directly correlate to the ratios of

the materials' nonlinear coefficients (Fig. 8.3). Repeating this measurement several times and averaging the results yield $\chi^{(2)}_{ccc}$ ~115 pm/V, $\chi^{(2)}_{aca}$ ~53 pm/V, and $\chi^{(2)}_{caa}$ ~26 pm/V, where $\chi^{(2)}_{ccc}$ is in the realm of values reported for ZB-GaAs [177]. Thus, WZ-GaAs maintains the strong nonlinear properties of ZB-GaAs while introducing birefringence. Because the measurements involve back-generated SHG collected in reflection mode, proper comparison requires normalization for the different reflectivities of the different materials. The calculations include factors essentially acting as second-harmonic Fresnel coefficients [178]. Deriving them requires solving the usual wave equation, but with a source term representing a second-harmonic nonlinear polarization density as shown in equation (8.3). Solving the equation for s- and p-polarized electric fields then yields equations (8.4) and (8.5), respectively. The co-factors in these equations are effectively the second-harmonic Fresnel coefficients. Figure 8.6 diagrams this process of second-harmonic generation at the air-dielectric boundary, labeling relevant parameters.

$$-\nabla^2 E + \frac{\varepsilon}{c^2}\frac{\partial^2 E}{\partial t^2} = -\frac{4\pi}{c^2}\frac{\partial^2 P^{(2)}}{\partial t^2} \tag{8.3}$$

$$E^{2\omega}_{r,s} = \frac{\tilde{n}_2(2\omega)\cos(\theta^{2\omega}_t) - \tilde{n}_2(\omega)\cos(\theta^{\omega}_t)}{\tilde{n}_2(2\omega)\cos(\theta^{2\omega}_t) + \tilde{n}_1(2\omega)\cos(\theta^{2\omega}_r)} \frac{4\pi}{\tilde{n}_2{}^2(\omega) - \tilde{n}_2{}^2(2\omega)} P^{(2)}_s(2\omega) \tag{8.4}$$

$$E^{2\omega}_{r,p} = \frac{\tilde{n}_2(\omega)\cos(\theta^{2\omega}_t) - \tilde{n}_2(2\omega)\cos(\theta^{\omega}_t)}{\tilde{n}_1(2\omega)\cos(\theta^{2\omega}_t) + \tilde{n}_2(2\omega)\cos(\theta^{2\omega}_r)} \frac{4\pi}{\tilde{n}_2{}^2(\omega) - \tilde{n}_2{}^2(2\omega)} P^{(2)}_p(2\omega) \tag{8.5}$$

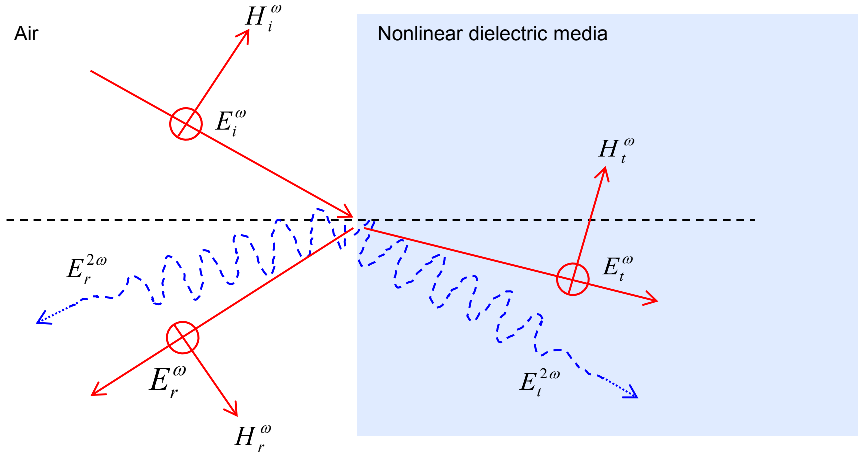

Figure 8.6 Backward-generated SHG. A schematic illustrates the backward generation of second-harmonic light from an air-dielectric boundary. Such SHG must satisfy what amounts to second harmonic Fresnel coefficients.

Because GaAs strongly absorbs at 400 nm, normalization for SHG reflected from the nanoneedle-sapphire boundary should be minimal and is neglected. Since the laser spot size should be smaller than the diameter of the nanoneedle's base, normalization for area is also neglected. Hence, the estimates are likely conservative and present a lower bound on the nonlinear optical coefficients of WZ-GaAs.

In conclusion, we have demonstrated second-harmonic generation of violet light using wurtzite GaAs nanoneedles in this section. The polarization dependence of the nonlinear process agrees with the selection rules for wurtzite crystals, further confirming that nanoneedles are indeed single crystalline wurtzite as reported in Ref. [53]. Furthermore, this agreement signifies that the SHG arises from the bulk of the nanoneedle itself and not only from asymmetry at the surface. While GaAs in the wurtzite phase introduces birefringence, we estimate that the nanoneedles still maintain the high nonlinear optical coefficients characteristic of ZB-GaAs. Able to grow on Si without metal catalysts at low temperatures, nanoneedles thus become attractive candidates to serve as nonlinear optical media for CMOS-compatible optoelectronic integration on Si. Because nanoneedles are much smaller than the expected SHG coherence length, they essentially function as SHG dipole emitters. More research thereby remains for investigating methods to increase SHG conversion efficiency for practical functionality in photonic circuits.

8.2 Resonance enhancement of nonlinear processes

As touched upon in Chapter 3, interesting nanophotonic phenomena occur when light-matter interaction approaches and surpasses subwavelength limits. In this section, we present a variety of experimental results that highlight how such interaction can impact nonlinear optical effects. While incomplete, this set of data hopefully motivates future research in the fascinating field of nonlinear nano-optoelectronics.

Second-harmonic generation

In this dissertation, nanopillar structures were shown to support helically-propagating modes, which can effectively be understood as a hybridization of classic Fabry-Perot and whispering gallery modes (WGMs). Chapter 4 demonstrated how these modes can interact with photoluminescence to catalyze laser oscillation. Here we present how such resonances can foster nonlinear light-matter interaction as well.

Spatially mapping out second-harmonic emission from GaAs nanoneedles suggests that localized enhancement of SHG occurs. In Fig. 8.7, we clearly see spatially localized maxima in SHG from single nanoneedles. The SHG patterns are highly reminiscent of PL emission imaged for helically-propagating modes as shown in Fig. 4.7. We thereby suggest that helically-propagating resonances in nanoneedles may be the origin of this localized enhancement in SHG.

Since SHG at ~400 nm is highly absorbed by GaAs, it is likely that helical modes enhance the excitation fs laser rather than the SHG itself. Localized enhancement the first-harmonic excitation light then locally enhances SHG, especially since SHG intensity scales with the 4th power of the first harmonic's field strength. We note here that these effects are most prominently seen for small nanoneedles less than 600 nm in diameter. For larger nanoneedles such as those studied in Section 8.1, resonance enhancement is not apparent, likely because the larger structures support a vast continuum of optical modes for incident illumination to couple into. For smaller nanoneedles, the number of optical modes is reduced, so the role played by nanophotonic resonances like helically-propagating modes is magnified.

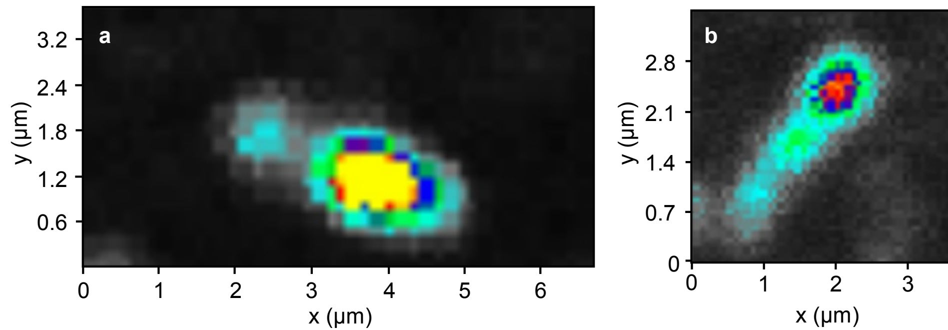

Figure 8.7 Resonance-enhanced second-harmonic generation. Imaging SHG from single nanoneedles reveals local enhancement effects that are highly reminiscent of helically-propagating modes imaged in Section 3.2. It is likely that helically-propagating resonances enhance SHG in smaller nanoneedle structures by enhancing the first harmonic pump light. Enhancement from an **a,** n=2 and a **b,** n=3 mode are shown.

Two-photon photoluminescence

This dissertation has discussed the interplay between metal-optics and nanoneedle-based materials for nano-optoelectronic device applications. It is also worthwhile to explore if the intersection of nanoneedles and plasmonics can offer interesting opportunities. After all, nanoneedle tips can be atomically sharp, and plasmonic effects are often most prominent at sharp points. Thus, we performed angled evaporation of gold (Au) onto nanoneedle samples such that Au coated only one side of nanoneedles. Effectively then, Au bowties form on the sides of nanoneedles, and their tips are co-located with the tips of nanoneedles [70]. Illuminating these samples with fs laser light yields interesting results that are shown in Fig. 8.8. A broad two-photon photoluminescence (TPPL) spectrum is observed. Per Fig. 8.8b, the TPPL intensity has a quadratic dependence on excitation power, confirming that the origin of the spectrum comes from a second-order nonlinear optical process. SHG is also observed, though it is uncertain if the SHG arises from the Au surfaces or from the GaAs nanoneedles. It is also unclear if the observed TPPL comes from plasmonic enhancement at the Au-plated tips of nanoneedles or if it simply comes from surface roughness of Au. This data thus motivates further study on using plasmon-

enhanced nanoneedle structures for enhanced nonlinearity. Given the natural geometry of nanoneedles, they may even be well-suite for nanofocusing and optical transformer applications [68].

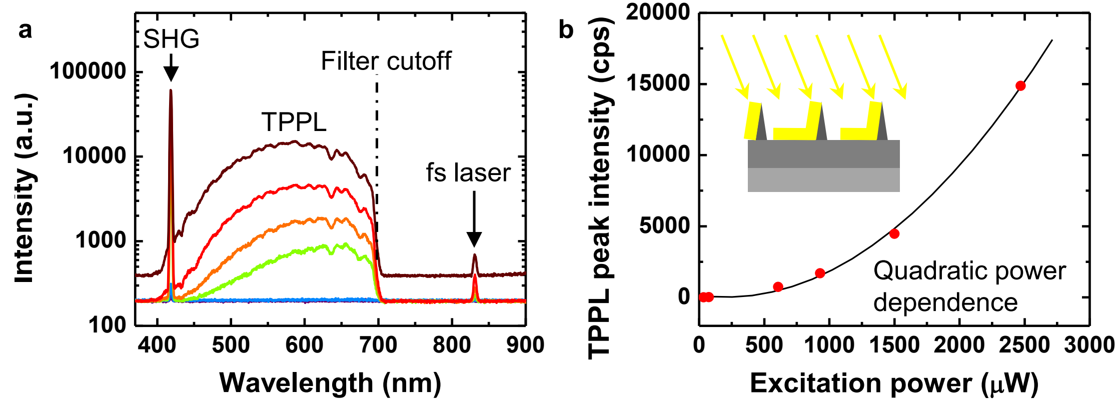

Figure 8.8 Two-photon photoluminescence from Au-coated nanoneedles. a, PL spectra show a broad two-photon photoluminescence signature. **b,** The TPPL has a quadratic power dependence as expected for second-order nonlinear effect.

Surface-enhanced Raman scattering

Following up on the TPPL results presented above, we now briefly touch on a particularly exciting nanofocusing application – surface-enhanced Raman scattering (SERS). SERS has been a topic of much excitement, confusion, and debate over the years. While both electromagnetic as well as chemical enhancement are known to be important, many fundamental questions about the precise origin of SERS remain unanswered [179]–[183]. What everyone does agree on is the propensity of the SERS effect for enabling single molecule detection [182]. Figure 8.9 shows SERS spectra for Rhodamine 6G (R6G) dye molecules dispersed on a roughened gold film. The enhanced Raman spectra for R6G can be clearly seen superimposed on the R6G's fluorescence signal. Without local field enhancements on the metal film, these Raman traces would be difficult if not impossible to detect above the fluorescence background. We thereby see the potency of the SERS effect, which may well be an interesting area of exploration for nanoneedle-based photonics in the future.

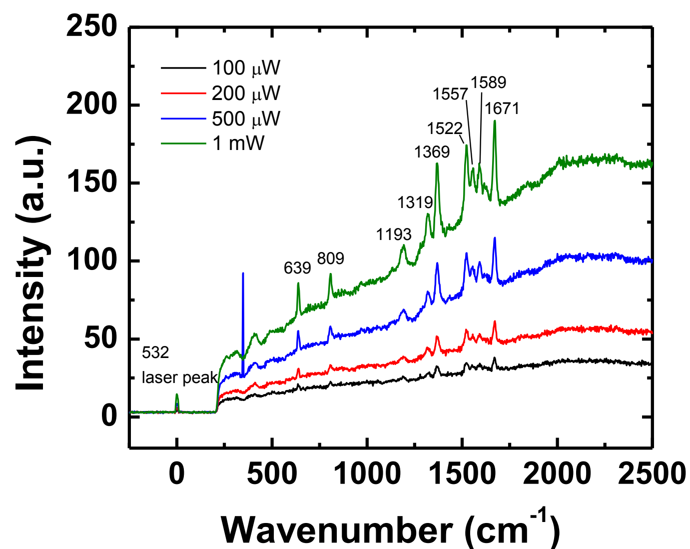

Figure 8.9 Surface-enhanced Raman scattering from Rhodamine 6G molecules on a roughened gold film. Clear SERS signals are recorded from R6G molecules on roughened gold film. The SERS spectrum matches others reported in literature.

Chapter 9

Conclusion

This dissertation proposed that electrons offer a conduit for complex control of photons. While we continue to struggle with harnessing light, our society has demonstrated considerable mastery over electrons. Because electrons harness light quite well, it is then sensible that controlling this electron-photon interaction provides us the best opportunity to masterfully manipulate photons. Silicon technology enables modern electronics, and thus, silicon technology offers the most powerful platform for photonic control. However, this requires bringing photonic functionality onto silicon, which has proven tremendously difficult. This thesis thus suggested that nanomaterial synthesis provides a favorable pathway towards imbuing silicon with full optical functionality.

This dissertation proved the viability of this pathway by showcasing how III-V nanoneedles and nanopillars alone can enable all the primary functions of optoelectronic devices: emission, detection, and solar power generation. In particular, we showed that nanolasers can be grown directly on silicon, while the same structures can also be leveraged for implementing integrated avalanche photodiodes. Though preliminary, results also demonstrated the potential for photovoltaics. Finally, we demonstrated how integrating III-V nanomaterials onto silicon can also imbue silicon with interesting nonlinear optical properties. The most important result of all is not any single photonic function on silicon, but rather the ability to integrate all of these functions onto silicon simultaneously.

Of course, much room exists for further research and development. First, practicality requires electrical injection of nanolasers on silicon. Initial results already show that this goal is close to being achieved. Additionally, the ultimate vision is integration of photonics with electronics and not just silicon alone. While preliminary results demonstrated laser integration with MOSFETs, compatibility with CMOS circuits remains unproven. Finally, the biggest challenge facing bottom-up nanomaterial integration is the difficulty of robustly and precisely controlling nucleation. When site-controlled growth is achieved in the future, then nanoneedles and nanopillars can truly enable massively scalable and well-behaved optoelectronic integration. Active electronic and photonic devices can then co-populate silicon to form complex nano-optoelectronic circuits as envisioned in Fig. 9.1.

Figure 9.1 Nano-optoelectronic integration with silicon electronics. A vision for the future

In closing, it is worthwhile to briefly present an outlook for the work that has been presented. Since this thesis focuses so much on the interfaces between things, let us think about some relevant interfaces that remained unexplored in this dissertation. In many respects, light functions as the interface between humans and their surroundings. Humans have been dubbed the ultimate pattern recognition machines, and sight is perhaps the dominant means by which humans recognize patterns. Additionally, light can have tremendous impact on human psychology. Beyond humans, light also provides the natural energy source needed for life-sustaining processes such as photosynthesis. Light therefore also functions as a catalyst for life. It appears then that photons provide a conduit for probing and manipulating biological systems much like electrons do for light. Thus, when human command over photons becomes sufficiently potent, it is well within reason that discovery and utility at the intersection between light and biology will reach its own inflection point.

References

[1] P. C. Lauterbur, “Image formation by induced local interactions: examples employing nuclear magnetic resonance,” *Nature*, vol. 242, no. 5394, pp. 190–191, 1973.
[2] P. Mansfield and A. A. Maudsley, “Medical imaging by NMR,” *Br J Radiol*, vol. 50, no. 591, pp. 188–194, Mar. 1977.
[3] T. A. Edison, “The Success of the Electric Light,” *The North American Review*, vol. 131, no. 287, pp. 295–300, 1880.
[4] J. M. Rabaey, A. P. Chandrakasan, and B. Nikolic, *Digital integrated circuits*, vol. 996. Prentice-Hall, 1996.
[5] G. E. Moore, “Cramming more components onto integrated circuits,” *Proceedings of the IEEE*, vol. 86, no. 1, pp. 82–85, 1998.
[6] A. Einstein, *A Heuristic Viewpoint Concerning the Production and Transformation of Light*. 1929.
[7] E. F. Schubert, T. Gessmann, and J. K. Kim, *Light emitting diodes*. Wiley Online Library, 2005.
[8] M. S. Bigelow, N. N. Lepeshkin, and R. W. Boyd, “Superluminal and Slow Light Propagation in a Room-Temperature Solid,” *Science*, vol. 301, no. 5630, pp. 200–202, Jul. 2003.
[9] P.-C. Ku, F. Sedgwick, C. J. Chang-Hasnain, P. Palinginis, T. Li, H. Wang, S.-W. Chang, and S.-L. Chuang, “Slow light in semiconductor quantum wells,” *Opt. Lett.*, vol. 29, no. 19, pp. 2291–2293, Oct. 2004.
[10] R. M. Stevenson, R. J. Young, P. Atkinson, K. Cooper, D. A. Ritchie, and A. J. Shields, “A semiconductor source of triggered entangled photon pairs,” *Nature*, vol. 439, no. 7073, pp. 179–182, Jan. 2006.
[11] C. L. Salter, R. M. Stevenson, I. Farrer, C. A. Nicoll, D. A. Ritchie, and A. J. Shields, “An entangled-light-emitting diode,” *Nature*, vol. 465, no. 7298, pp. 594–597, Jun. 2010.
[12] ITRS, “[Online]. Available: http://public.itrs.net/.” .
[13] D. A. B. Miller, “Device Requirements for Optical Interconnects to Silicon Chips,” *Proc. IEEE*, 2009.
[14] A. V. Krishnamoorthy, K. W. Goossen, W. Jan, X. Zheng, R. Ho, G. Li, R. Rozier, F. Liu, D. Patil, J. Lexau, and others, “Progress in low-power switched optical interconnects,” *Selected Topics in Quantum Electronics, IEEE Journal of*, no. 99, pp. 1–20, 2011.
[15] S. Nakamura, T. Mukai, and M. Senoh, “Candela #x2010;class high #x2010;brightness InGaN/AlGaN double #x2010;heterostructure blue #x2010;light #x2010;emitting diodes,” *Applied Physics Letters*, vol. 64, no. 13, pp. 1687 –1689, Mar. 1994.
[16] S.-I. Park, Y. Xiong, R.-H. Kim, P. Elvikis, M. Meitl, D.-H. Kim, J. Wu, J. Yoon, C.-J. Yu, Z. Liu, Y. Huang, K. Hwang, P. Ferreira, X. Li, K. Choquette, and J. A. Rogers, “Printed Assemblies of Inorganic Light-Emitting Diodes for Deformable

and Semitransparent Displays," *Science*, vol. 325, no. 5943, pp. 977–981, Aug. 2009.
[17] K. Mathieson, J. Loudin, G. Goetz, P. Huie, L. Wang, T. I. Kamins, L. Galambos, R. Smith, J. S. Harris, A. Sher, and D. Palanker, "Photovoltaic retinal prosthesis with high pixel density," *Nature Photonics*, vol. 6, no. 6, pp. 391–397, 2012.
[18] M. E. Groenert, C. W. Leitz, A. J. Pitera, V. Yang, H. Lee, R. J. Ram, and E. A. Fitzgerald, "Monolithic integration of room-temperature cw GaAs/AlGaAs lasers on Si substrates via relaxed graded GeSi buffer layers," *J. Appl. Phys.*, vol. 93, no. 1, p. 362, 2003.
[19] D. K. Biegelsen, F. A. Ponce, A. J. Smith, and J. C. Tramontana, "Initial stages of epitaxial growth of GaAs on (100) silicon," *Journal of Applied Physics*, vol. 61, no. 5, pp. 1856–1859, Mar. 1987.
[20] R. S. Wagner and W. C. Ellis, "VAPOR-LIQUID-SOLID MECHANISM OF SINGLE CRYSTAL GROWTH," *Applied Physics Letters*, vol. 4, no. 5, pp. 89–90, Mar. 1964.
[21] Z. Mi, P. Bhattacharya, J. Yang, and K. P. Pipe, "Room-temperature self-organised In0.5Ga0.5As quantum dot laser on silicon," *Electronics Letters*, vol. 41, no. 13, pp. 742 – 744, Jun. 2005.
[22] H. Takeuchi, A. Wung, Xin Sun, R. T. Howe, and Tsu-Jae King, "Thermal budget limits of quarter-micrometer foundry CMOS for post-processing MEMS devices," *Electron Devices, IEEE Transactions on*, vol. 52, no. 9, pp. 2081–2086, 2005.
[23] M. Shimbo, K. Furukawa, K. Fukuda, and K. Tanzawa, "Silicon-to-silicon direct bonding method," *Journal of Applied Physics*, vol. 60, no. 8, pp. 2987–2989, Oct. 1986.
[24] J. Haisma, G. A. C. M. Spierings, U. K. P. Biermann, and J. A. Pals, "Silicon-on-Insulator Wafer Bonding-Wafer Thinning Technological Evaluations," *Japanese Journal of Applied Physics*, vol. 28, no. Part 1, No. 8, pp. 1426–1443, 1989.
[25] Z. L. Liau and D. E. Mull, "Wafer fusion: A novel technique for optoelectronic device fabrication and monolithic integration," *Applied Physics Letters*, vol. 56, no. 8, pp. 737–739, Feb. 1990.
[26] A. Black, A. R. Hawkins, N. M. Margalit, D. I. Babic, J. Holmes, A.L., Y.-L. Chang, P. Abraham, J. E. Bowers, and E. L. Hu, "Wafer fusion: materials issues and device results," *IEEE Journal of Selected Topics in Quantum Electronics*, vol. 3, no. 3, pp. 943 –951, Jun. 1997.
[27] U. Gösele and Q.-Y. Tong, "Semiconductor Wafer Bonding," *Annual Review of Materials Science*, vol. 28, no. 1, pp. 215–241, 1998.
[28] M. A. Schmidt, "Wafer-to-wafer bonding for microstructure formation," *Proceedings of the IEEE*, vol. 86, no. 8, pp. 1575 –1585, Aug. 1998.
[29] K. W. Goossen, J. A. Walker, L. A. D'Asaro, S. P. Hui, B. Tseng, R. Leibenguth, D. Kossives, D. D. Bacon, D. Dahringer, L. M. F. Chirovsky, A. L. Lentine, and D. A. B. Miller, "GaAs MQW modulators integrated with silicon CMOS," *IEEE Photonics Technology Letters*, vol. 7, no. 4, pp. 360 –362, Apr. 1995.
[30] G. S. Matijasevic, C. Y. Wang, and C. C. Lee, "Void free bonding of large silicon dice using gold-tin alloys," *IEEE Transactions on Components, Hybrids, and Manufacturing Technology*, vol. 13, no. 4, pp. 1128 –1134, Dec. 1990.

[31] C. H. Tsau, S. M. Spearing, and M. A. Schmidt, "Fabrication of wafer-level thermocompression bonds," *Journal of Microelectromechanical Systems*, vol. 11, no. 6, pp. 641 – 647, Dec. 2002.
[32] A. Fan, A. Rahman, and R. Reif, "Copper Wafer Bonding," *Electrochem. Solid-State Lett.*, vol. 2, no. 10, pp. 534–536, Oct. 1999.
[33] J. I. Pankove, *Optical processes in semiconductors*. Dover Publications, 2010.
[34] L. Pavesi, L. D. Negro, C. Mazzoleni, G. Franzo, and F. Priolo, "Optical gain in silicon nanocrystals," *Nature*, vol. 408, no. 6811, pp. 440–444, 2000.
[35] S. G. Cloutier, P. A. Kossyrev, and J. Xu, "Optical gain and stimulated emission in periodic nanopatterned crystalline silicon," *Nat Mater*, vol. 4, no. 12, pp. 887–891, Dec. 2005.
[36] S. S. Walavalkar, C. E. Hofmann, A. P. Homyk, M. D. Henry, H. A. Atwater, and A. Scherer, "Tunable Visible and Near-IR Emission from Sub-10 nm Etched Single-Crystal Si Nanopillars," *Nano Lett.*, vol. 10, no. 11, pp. 4423–4428, Nov. 2010.
[37] M. A. Green, J. Zhao, A. Wang, P. J. Reece, and M. Gal, "Efficient silicon light-emitting diodes," *Nature*, vol. 412, no. 6849, pp. 805–808, 2001.
[38] J. Liu, X. Sun, R. Camacho-Aguilera, L. C. Kimerling, and J. Michel, "Ge-on-Si laser operating at room temperature," *Opt. Lett.*, vol. 35, no. 5, pp. 679–681, Mar. 2010.
[39] R. E. Camacho-Aguilera, Y. Cai, N. Patel, J. T. Bessette, M. Romagnoli, L. C. Kimerling, and J. Michel, "An electrically pumped germanium laser," *Opt. Express*, vol. 20, no. 10, pp. 11316–11320, May 2012.
[40] Y.-H. Kuo, Y. K. Lee, Y. Ge, S. Ren, J. E. Roth, T. I. Kamins, D. A. B. Miller, and J. S. Harris, "Strong quantum-confined Stark effect in germanium quantum-well structures on silicon," *Nature*, vol. 437, no. 7063, pp. 1334–1336, Oct. 2005.
[41] J. Michel, J. Liu, and L. C. Kimerling, "High-performance Ge-on-Si photodetectors," *Nat Photon*, vol. 4, no. 8, pp. 527–534, 2010.
[42] J. R. Jain, A. Hryciw, T. M. Baer, D. A. B. Miller, M. L. Brongersma, and R. T. Howe, "A micromachining-based technology for enhancing germanium light emission via tensile strain," *Nature Photonics*, vol. 6, no. 6, pp. 398–405, 2012.
[43] T. Martensson, C. P. T. Svensson, B. A. Wacaser, M. W. Larsson, W. Seifert, K. Deppert, A. Gustafsson, L. R. Wallenberg, and L. Samuelson, "Epitaxial III−V Nanowires on Silicon," *Nano Letters*, vol. 4, no. 10, pp. 1987–1990, Oct. 2004.
[44] M. Moewe, "Growth and Characterization of III-V Nanowires and Nanoneedles," University of California, Berkeley, 2009.
[45] L. C. Chuang, M. Moewe, C. Chase, N. P. Kobayashi, C. Chang-Hasnain, and S. Crankshaw, "Critical diameter for III-V nanowires grown on lattice-mismatched substrates," *Appl. Phys. Lett.*, vol. 90, no. 4, p. 043115, 2007.
[46] K. Tomioka, J. Motohisa, S. Hara, K. Hiruma, and T. Fukui, "GaAs/AlGaAs Core Multishell Nanowire-Based Light-Emitting Diodes on Si," *Nano Letters*, vol. 10, no. 5, pp. 1639–1644, May 2010.
[47] D. Hisamoto, W.-C. Lee, J. Kedzierski, H. Takeuchi, K. Asano, C. Kuo, E. Anderson, T.-J. King, J. Bokor, and C. Hu, "FinFET-a self-aligned double-gate MOSFET scalable to 20 nm," *IEEE Transactions on Electron Devices*, vol. 47, no. 12, pp. 2320 – 2325, Dec. 2000.

[48] T. Bryllert, L.-E. Wernersson, L. E. Froberg, and L. Samuelson, “Vertical high-mobility wrap-gated InAs nanowire transistor,” *IEEE Electron Device Letters*, vol. 27, no. 5, pp. 323 – 325, May 2006.
[49] R. J. W. Hill, D. A. J. Moran, X. Li, H. Zhou, D. Macintyre, S. Thoms, A. Asenov, P. Zurcher, K. Rajagopalan, J. Abrokwah, R. Droopad, M. Passlack, and I. G. Thayne, “Enhancement-Mode GaAs MOSFETs With an In0.3 Ga0.7As Channel, a Mobility of Over 5000 cm2/V #183;s, and Transconductance of Over 475 #956;S/ #956;m,” *IEEE Electron Device Letters*, vol. 28, no. 12, pp. 1080 –1082, Dec. 2007.
[50] R. Chau, S. Datta, M. Doczy, B. Doyle, B. Jin, J. Kavalieros, A. Majumdar, M. Metz, and M. Radosavljevic, “Benchmarking nanotechnology for high-performance and low-power logic transistor applications,” *IEEE Transactions on Nanotechnology*, vol. 4, no. 2, pp. 153 – 158, Mar. 2005.
[51] J. A. del Alamo, “Nanometre-scale electronics with III-V compound semiconductors,” *Nature*, vol. 479, no. 7373, pp. 317–323, Nov. 2011.
[52] L. C. Chuang, “III-V Nanowires and Nanoneedles on Lattice Mismatched Substrates for Optoelectronic Device Applications,” University of California, Berkeley, 2011.
[53] M. Moewe, L. C. Chuang, S. Crankshaw, C. Chase, and C. Chang-Hasnain, “Atomically sharp catalyst-free wurtzite GaAs/AlGaAs nanoneedles grown on silicon,” *Appl. Phys. Lett.*, vol. 93, no. 2, pp. 023116–3, Jul. 2008.
[54] L. C. Chuang, M. Moewe, K. W. Ng, T.-T. D. Tran, S. Crankshaw, R. Chen, W. S. Ko, and C. Chang-Hasnain, “GaAs nanoneedles grown on sapphire,” *Appl. Phys. Lett.*, vol. 98, no. 12, p. 123101, 2011.
[55] K. W. Ng, W. Ko, R. Chen, T.-T. D. Tran, F. Lu, L. C. Chuang, F. G. Sedgwick, and C. Chang-Hasnain, “Nanolasers Grown on Polycrystalline Silicon,” in *IEEE Photonics Society 23rd Annual Meeting*, Denver, CO, 2010.
[56] S. Crankshaw, “Spectroscopic Characterization of III-V Semiconductor Nanomaterials,” University of California, Berkeley, 2010.
[57] S. L. Chuang and others, “Physics of optoelectronic devices,” 1995.
[58] K. Domen, K. Horino, A. Kuramata, and T. Tanahashi, “Analysis of polarization anisotropy along the c axis in the photoluminescence of wurtzite GaN,” *Appl. Phys. Lett.*, vol. 71, no. 14, pp. 1996–1998, Oct. 1997.
[59] A. Maslov and C. Ning, “Radius-dependent polarization anisotropy in semiconductor nanowires,” *Phys. Rev. B*, vol. 72, no. 16, Oct. 2005.
[60] J. C. Johnson, K. P. Knutsen, H. Yan, M. Law, Y. Zhang, P. Yang, and R. J. Saykally, “Ultrafast carrier dynamics in single ZnO nanowire and nanoribbon lasers,” *Nano Letters*, vol. 4, no. 2, pp. 197–204, 2004.
[61] S. Crankshaw, S. Reitzenstein, L. C. Chuang, M. Moewe, S. Münch, C. Böckler, A. Forchel, and C. Chang-Hasnain, “Recombination dynamics in wurtzite InP nanowires,” *Phys. Rev. B*, vol. 77, no. 23, Jun. 2008.
[62] S. Reitzenstein, S. Münch, C. Hofmann, A. Forchel, S. Crankshaw, L. C. Chuang, M. Moewe, and C. Chang-Hasnain, “Time resolved microphotoluminescence studies of single InP nanowires grown by low pressure metal organic chemical vapor deposition,” *Applied Physics Letters*, vol. 91, no. 9, p. 091103, 2007.

[63] M. Mattila, T. Hakkarainen, H. Lipsanen, H. Jiang, and E. I. Kauppinen, "Enhanced luminescence from catalyst-free grown InP nanowires," *Applied Physics Letters*, vol. 90, no. 3, p. 033101, 2007.
[64] L. M. Smith, H. E. Jackson, J. M. Yarrison-Rice, and C. Jagadish, "Insights into single semiconductor nanowire heterostructures using time-resolved photoluminescence," *Semiconductor Science and Technology*, vol. 25, no. 2, p. 024010, Feb. 2010.
[65] W. Becker, A. Bergmann, M. A. Hink, K. König, K. Benndorf, and C. Biskup, "Fluorescence lifetime imaging by time-correlated single-photon counting," *Microscopy research and technique*, vol. 63, no. 1, pp. 58–66, 2003.
[66] D. V. O'connor and D. Phillips, *Time-correlated single photon counting*, vol. 102. Academic Press London, 1984.
[67] K. Pemasiri, M. Montazeri, R. Gass, L. M. Smith, H. E. Jackson, J. Yarrison-Rice, S. Paiman, Q. Gao, H. H. Tan, C. Jagadish, X. Zhang, and J. Zou, "Carrier Dynamics and Quantum Confinement in type II ZB-WZ InP Nanowire Homostructures," *Nano Lett.*, vol. 9, no. 2, pp. 648–654, Feb. 2009.
[68] H. Choo, M.-K. Kim, M. Staffaroni, T. J. Seok, J. Bokor, S. Cabrini, P. J. Schuck, M. C. Wu, and E. Yablonovitch, "Nanofocusing in a metal-insulator-metal gap plasmon waveguide with a three-dimensional linear taper," *Nature Photonics*, vol. 6, no. 12, pp. 838–844, 2012.
[69] K. B. Crozier, A. Sundaramurthy, G. S. Kino, and C. F. Quate, "Optical antennas: Resonators for local field enhancement," *J. Appl. Phys.*, vol. 94, no. 7, p. 4632, 2003.
[70] P. J. Schuck, D. P. Fromm, A. Sundaramurthy, G. S. Kino, and W. E. Moerner, "Improving the Mismatch between Light and Nanoscale Objects with Gold Bowtie Nanoantennas," *Physical Review Letters*, vol. 94, no. 1, Jan. 2005.
[71] R. W. Wood, "XLII. On a remarkable case of uneven distribution of light in a diffraction grating spectrum," *Philosophical Magazine Series 6*, vol. 4, no. 21, pp. 396–402, 1902.
[72] R. F. Oulton, V. J. Sorger, T. Zentgraf, R.-M. Ma, C. Gladden, L. Dai, G. Bartal, and X. Zhang, "Plasmon lasers at deep subwavelength scale," *Nature*, vol. 461, no. 7264, pp. 629–632, Aug. 2009.
[73] R.-M. Ma, R. F. Oulton, V. J. Sorger, and X. Zhang, "Room temperature plasmon laser by total internal reflection," *1004.4227*, Apr. 2010.
[74] M. A. Noginov, G. Zhu, A. M. Belgrave, R. Bakker, V. M. Shalaev, E. E. Narimanov, S. Stout, E. Herz, T. Suteewong, and U. Wiesner, "Demonstration of a spaser-based nanolaser," *Nature*, vol. advance online publication, online 2009.
[75] N. I. Zheludev, S. L. Prosvirnin, N. Papasimakis, and V. A. Fedotov, "Lasing spaser," *Nature Photon*, vol. 2, no. 6, pp. 351–354, month> </month> <month>6</month>/<year></year> <year>2008</year 2008.
[76] M. I. Stockman, "Spasers explained," *Nature Photonics*, vol. 2, no. 6, pp. 327–329, 2008.
[77] K. Yu, A. Lakhani, and M. C. Wu, "Subwavelength metal-optic semiconductor nanopatch lasers," *Opt. Express*, vol. 18, no. 9, pp. 8790–8799, Apr. 2010.

[78] M. P. Nezhad, A. Simic, O. Bondarenko, B. Slutsky, A. Mizrahi, L. Feng, V. Lomakin, and Y. Fainman, “Room-temperature subwavelength metallo-dielectric lasers,” *Nature Photonics*, vol. 4, no. 6, pp. 395–399, Apr. 2010.
[79] L. Tang, S. E. Kocabas, S. Latif, A. K. Okyay, D.-S. Ly-Gagnon, K. C. Saraswat, and D. A. B. Miller, “Nanometre-scale germanium photodetector enhanced by a near-infrared dipole antenna,” *Nature Photon*, vol. 2, no. 4, pp. 226–229, month> </month> <month>4</month>/<year></year> <year>2008</year 2008.
[80] H. A. Atwater and A. Polman, “Plasmonics for improved photovoltaic devices,” *Nat Mater*, vol. 9, no. 3, pp. 205–213, Mar. 2010.
[81] M. Staffaroni, J. Conway, S. Vedantam, J. Tang, and E. Yablonovitch, “Circuit Analysis in Metal-Optics,” *arXiv:1006.3126*, Jun. 2010.
[82] T. Nobis and M. Grundmann, “Low-order optical whispering-gallery modes in hexagonal nanocavities,” *Phys. Rev. A*, vol. 72, no. 6, p. 063806, Dec. 2005.
[83] T. Nobis, E. Kaidashev, A. Rahm, M. Lorenz, and M. Grundmann, “Whispering Gallery Modes in Nanosized Dielectric Resonators with Hexagonal Cross Section,” *Physical Review Letters*, vol. 93, no. 10, Sep. 2004.
[84] J. M. Senior and M. Y. Jamro, *Optical fiber communications: principles and practice*. Prentice Hall, 2008.
[85] G. Mie, “Beiträge zur Optik trüber Medien, speziell kolloidaler Metallösungen,” *Annalen der Physik*, vol. 330, no. 3, pp. 377–445, 1908.
[86] T. H. Maiman, “Stimulated optical radiation in ruby,” *Nature*, vol. 187, no. 4736, pp. 493–494, 1960.
[87] G. Chen, H. Chen, M. Haurylau, N. A. Nelson, D. H. Albonesi, P. M. Fauchet, and E. G. Friedman, “Predictions of CMOS compatible on-chip optical interconnect,” *Integration, the VLSI Journal*, vol. 40, no. 4, pp. 434–446, Jul. 2007.
[88] H. Rong, A. Liu, R. Jones, O. Cohen, D. Hak, R. Nicolaescu, A. Fang, and M. Paniccia, “An all-silicon Raman laser,” *Nature*, vol. 433, no. 7023, pp. 292–294, 2005.
[89] H. Rong, R. Jones, A. Liu, O. Cohen, D. Hak, A. Fang, and M. Paniccia, “A continuous-wave Raman silicon laser,” *Nature*, vol. 433, no. 7027, pp. 725–728, Feb. 2005.
[90] O. Boyraz and B. Jalali, “Demonstration of a silicon Raman laser,” *Opt. Express*, vol. 12, no. 21, pp. 5269–5273, Oct. 2004.
[91] A. W. Fang, H. Park, O. Cohen, R. Jones, M. J. Paniccia, and J. E. Bowers, “Electrically pumped hybrid AlGaInAs-silicon evanescent laser,” *Opt. Express*, vol. 14, no. 20, pp. 9203–9210, 2006.
[92] J. Van Campenhout, P. Rojo Romeo, P. Regreny, C. Seassal, D. Van Thourhout, S. Verstuyft, L. Di Cioccio, J.-M. Fedeli, C. Lagahe, and R. Baets, “Electrically pumped InP-based microdisk lasers integrated with a nanophotonic silicon-on-insulator waveguide circuit,” *Opt. Express*, vol. 15, no. 11, pp. 6744–6749, May 2007.
[93] Y. H. Lo, R. Bhat, D. M. Hwang, C. Chua, and C.-H. Lin, “Semiconductor lasers on Si substrates using the technology of bonding by atomic rearrangement,” *Appl. Phys. Lett.*, vol. 62, no. 10, p. 1038, 1993.

[94] H. Z. Chen, A. Ghaffari, H. Wang, H. Morkoç, and A. Yariv, "Low-threshold (~600 A/cm2 at room temperature) GaAs/AlGaAs lasers on Si (100)," *Appl. Phys. Lett.*, vol. 51, no. 17, p. 1320, 1987.
[95] Y. Ujiie and T. Nishinaga, "Epitaxial Lateral Overgrowth of GaAs on a Si Substrate," *Jpn. J. Appl. Phys.*, vol. 28, no. Part 2, No. 3, pp. L337–L339, Mar. 1989.
[96] F. Olsson, M. Xie, S. Lourdudoss, I. Prieto, and P. A. Postigo, "Epitaxial lateral overgrowth of InP on Si from nano-openings: Theoretical and experimental indication for defect filtering throughout the grown layer," *J. Appl. Phys.*, vol. 104, no. 9, p. 093112, 2008.
[97] M. Moewe, L. C. Chuang, S. Crankshaw, K. W. Ng, and C. Chang-Hasnain, "Core-shell InGaAs/GaAs quantum well nanoneedles grown on silicon with silicon-transparent emission," *Opt. Express*, vol. 17, no. 10, pp. 7831–7836, May 2009.
[98] R. Chen, S. Crankshaw, T. Tran, L. C. Chuang, M. Moewe, and C. Chang-Hasnain, "Second-harmonic generation from a single wurtzite GaAs nanoneedle," *Appl. Phys. Lett.*, vol. 96, no. 5, pp. 051110–3, Feb. 2010.
[99] L. C. Chuang, R. Chen, F. G. Sedgwick, W. S. Ko, K. W. Ng, T. T. . Tran, and C. Chang-Hasnain, "InGaAs QW Nanopillar Light Emitting Diodes Monolithically Grown on a Si Substrate," in *Conference on Lasers and Electro-Optics*, 2010.
[100] L. A. Coldren and S. W. Corzine, *Diode lasers and photonic integrated circuits*. Wiley New York, 1995.
[101] T. Baba, "Photonic crystals and microdisk cavities based on GaInAsP-InP system," *IEEE Journal of Selected Topics in Quantum Electronics*, vol. 3, no. 3, pp. 808–830, 1997.
[102] G. Bjork and Y. Yamamoto, "Analysis of semiconductor microcavity lasers using rate equations," *Quantum Electronics, IEEE Journal of*, vol. 27, no. 11, pp. 2386–2396, 1991.
[103] S. L. McCall, A. F. J. Levi, R. E. Slusher, S. J. Pearton, and R. A. Logan, "Whispering-gallery mode microdisk lasers," *Applied physics letters*, vol. 60, no. 3, pp. 289–291, 1992.
[104] J. Wiersig, "Hexagonal dielectric resonators and microcrystal lasers," *Phys. Rev. A*, vol. 67, no. 2, Feb. 2003.
[105] R. Chen, L. C. Chuang, Thai Tran, M. Moewe, and C. Chang-Hasnain, "Spatially resolved, polarized photoluminescence from wurtzite InGaAs/GaAs nanoneedles," in *Lasers and Electro-Optics (CLEO) and Quantum Electronics and Laser Science Conference (QELS), 2010 Conference on*, 2010, pp. 1–2.
[106] M. T. Hill, Y.-S. Oei, B. Smalbrugge, Y. Zhu, T. de Vries, P. J. van Veldhoven, F. W. M. van Otten, T. J. Eijkemans, J. P. Turkiewicz, H. de Waardt, E. J. Geluk, S.-H. Kwon, Y.-H. Lee, R. Notzel, and M. K. Smit, "Lasing in metallic-coated nanocavities," *Nat Photon*, vol. 1, no. 10, pp. 589–594, Oct. 2007.
[107] M. T. Hill, M. Marell, E. S. P. Leong, B. Smalbrugge, Y. Zhu, M. Sun, P. J. van Veldhoven, E. J. Geluk, F. Karouta, Y.-S. Oei, R. Nötzel, C.-Z. Ning, and M. K. Smit, "Lasing in metal-insulator-metal sub-wavelength plasmonic waveguides," *Opt. Express*, vol. 17, no. 13, pp. 11107–11112, Jun. 2009.
[108] T. Kuykendall, P. Ulrich, S. Aloni, and P. Yang, "Complete composition tunability of InGaN nanowires using a combinatorial approach," *Nat Mater*, vol. 6,

no. 12, pp. 951–956, month> </month> <month>12</month>/<year></year> <year>2007</year 2007.

[109] F. Qian, Y. Li, S. Gradecak, H.-G. Park, Y. Dong, Y. Ding, Z. L. Wang, and C. M. Lieber, “Multi-quantum-well nanowire heterostructures for wavelength-controlled lasers,” *Nat Mater*, vol. 7, no. 9, pp. 701–706, 2008.

[110] A. Pan, W. Zhou, E. S. . Leong, R. Liu, A. H. Chin, B. Zou, and C. Z. Ning, “Continuous Alloy-Composition Spatial Grading and Superbroad Wavelength-Tunable Nanowire Lasers on a Single Chip,” *Nano letters*, vol. 9, no. 2, pp. 784–788, 2009.

[111] M. Kawachi, “Silica waveguides on silicon and their application to integrated-optic components,” *Optical and Quantum Electronics*, vol. 22, no. 5, pp. 391–416, 1990.

[112] S. Suzuki, K. Shuto, and Y. Hibino, “Integrated-optic ring resonators with two stacked layers of silica waveguide on Si,” *Photonics Technology Letters, IEEE*, vol. 4, no. 11, pp. 1256–1258, 1992.

[113] W. Bogaerts, R. Baets, P. Dumon, V. Wiaux, S. Beckx, D. Taillaert, B. Luyssaert, J. Van Campenhout, P. Bienstman, and D. Van Thourhout, “Nanophotonic waveguides in silicon-on-insulator fabricated with CMOS technology,” *Lightwave Technology, Journal of*, vol. 23, no. 1, pp. 401–412, 2005.

[114] D. J. Erskine, A. J. Taylor, and C. L. Tang, “Femtosecond studies of intraband relaxation in GaAs, AlGaAs, and GaAs/AlGaAs multiple quantum well structures,” *Appl. Phys. Lett.*, vol. 45, no. 1, p. 54, 1984.

[115] H. Yokoyama and S. D. Brorson, “Rate equation analysis of microcavity lasers,” *J. Appl. Phys.*, vol. 66, no. 10, p. 4801, 1989.

[116] T. Baba, P. Fujita, A. Sakai, M. Kihara, and R. Watanabe, “Lasing characteristics of GaInAsP-InP strained quantum-well microdisk injection lasers with diameter of 2-10 μm,” *Photonics Technology Letters, IEEE*, vol. 9, no. 7, pp. 878–880, 1997.

[117] I. Protsenko, P. Domokos, V. Lef�vre-Seguin, J. Hare, J. M. Raimond, and L. Davidovich, “Quantum theory of a thresholdless laser,” *Phys. Rev. A*, vol. 59, no. 2, p. 1667, Feb. 1999.

[118] T. Baba and D. Sano, “Low-threshold lasing and purcell effect in microdisk lasers at room temperature,” *IEEE Journal of Selected Topics in Quantum Electronics*, vol. 9, no. 5, pp. 1340–1346, Sep. 2003.

[119] S. Ando, N. Kobayashi, and H. Ando, “Novel Hexagonal-Facet GaAs/AlGaAs Laser Grown by Selective Area Metalorganic Chemical Vapor Deposition,” *Jpn. J. Appl. Phys.*, vol. 32, pp. L1293–L1296, 1993.

[120] Seung June Choi, K. Djordjev, Sang Jun Choi, and P. D. Dapkus, “Microdisk lasers vertically coupled to output waveguides,” *IEEE Photonics Technology Letters*, vol. 15, no. 10, pp. 1330–1332, Oct. 2003.

[121] D. Taillaert, W. Bogaerts, P. Bienstman, T. F. Krauss, P. Van Daele, I. Moerman, S. Verstuyft, K. De Mesel, and R. Baets, “An out-of-plane grating coupler for efficient butt-coupling between compact planar waveguides and single-mode fibers,” *Quantum Electronics, IEEE Journal of*, vol. 38, no. 7, pp. 949–955, 2002.

[122] L. Mahler, A. Tredicucci, F. Beltram, C. Walther, J. Faist, B. Witzigmann, H. E. Beere, and D. A. Ritchie, “Vertically emitting microdisk lasers,” *Nat Photon*, vol. 3, no. 1, pp. 46–49, Jan. 2009.
[123] S. Koseki, B. Zhang, K. De Greve, and Y. Yamamoto, “Monolithic integration of quantum dot containing microdisk microcavities coupled to air-suspended waveguides,” *Appl. Phys. Lett.*, vol. 94, no. 5, p. 051110, 2009.
[124] F. Lu, T. T. D. Tran, W. S. Ko, K. W. Ng, R. Chen, and C. Chang-Hasnain, “Nanolasers grown on silicon-based MOSFETs,” *Optics Express*, vol. 20, no. 11, pp. 12171–12176, 2012.
[125] L. C. Chuang, F. G. Sedgwick, R. Chen, W. S. Ko, M. Moewe, K. W. Ng, T.-T. D. Tran, and C. Chang-Hasnain, “GaAs-Based Nanoneedle Light Emitting Diode and Avalanche Photodiode Monolithically Integrated on a Silicon Substrate,” *Nano Letters*, vol. 11, no. 2, pp. 385–390, Feb. 2011.
[126] Y. P. Varshni, “Temperature dependence of the energy gap in semiconductors,” *Physica*, vol. 34, no. 1, pp. 149–154, 1967.
[127] K. P. O’Donnell and X. Chen, “Temperature dependence of semiconductor band gaps,” *Applied Physics Letters*, vol. 58, no. 25, pp. 2924–2926, Jun. 1991.
[128] M. Bertolotti, V. Bogdanov, A. Ferrari, A. Jascow, N. Nazorova, A. Pikhtin, and L. Schirone, “Temperature dependence of the refractive index in semiconductors,” *J. Opt. Soc. Am. B*, vol. 7, no. 6, pp. 918–922, Jun. 1990.
[129] J. A. McCaulley, V. M. Donnelly, M. Vernon, and I. Taha, “Temperature dependence of the near-infrared refractive index of silicon, gallium arsenide, and indium phosphide,” *Phys. Rev. B*, vol. 49, no. 11, pp. 7408–7417, Mar. 1994.
[130] D. T. F. Marple, “Refractive Index of GaAs,” *Journal of Applied Physics*, vol. 35, no. 4, pp. 1241–1242, Apr. 1964.
[131] P. S. Zory, *Quantum well lasers*. Academic Pr, 1993.
[132] W. T. Tsang, “A graded-index waveguide separate-confinement laser with very low threshold and a narrow Gaussian beam,” *Appl. Phys. Lett.*, vol. 39, no. 2, pp. 134–137, Jul. 1981.
[133] W. T. Tsang, “Low-current-threshold and high-lasing uniformity GaAs–Al x Ga 1-x As double-heterostructure lasers grown by molecular beam epitaxy,” *Applied Physics Letters*, vol. 34, no. 7, pp. 473–475, 1979.
[134] W. T. Tsang, “Extremely low threshold (AlGa) As graded-index waveguide separate-confinement heterostructure lasers grown by molecular beam epitaxy,” *Applied Physics Letters*, vol. 40, no. 3, pp. 217–219, 1982.
[135] W. T. Tsang, “Extremely low threshold (AlGa) As modified multiquantum well heterostructure lasers grown by molecular-beam epitaxy,” *Applied Physics Letters*, vol. 39, no. 10, pp. 786–788, 1981.
[136] S. Assefa, F. Xia, and Y. A. Vlasov, “Reinventing germanium avalanche photodetector for nanophotonic on-chip optical interconnects,” *Nature*, vol. 464, no. 7285, pp. 80–84, Mar. 2010.
[137] Y. Kang, H.-D. Liu, M. Morse, M. J. Paniccia, M. Zadka, S. Litski, G. Sarid, A. Pauchard, Y.-H. Kuo, H.-W. Chen, W. S. Zaoui, J. E. Bowers, A. Beling, D. C. McIntosh, X. Zheng, and J. C. Campbell, “Monolithic germanium//silicon

avalanche photodiodes with 340 GHz gain-bandwidth product," *Nat Photon*, vol. 3, no. 1, pp. 59–63, Jan. 2009.
[138] X. Zheng, F. Liu, D. Patil, H. Thacker, Y. Luo, T. Pinguet, A. Mekis, J. Yao, G. Li, J. Shi, and others, "A sub-picojoule-per-bit CMOS photonic receiver for densely integrated systems," *Optics Express*, vol. 18, no. 1, pp. 204–211, 2010.
[139] S. M. Sze and K. K. Ng, *Physics of semiconductor devices*. Wiley-interscience, 2006.
[140] F. Capasso, "Chapter 1 Physics of Avalanche Photodiodes," in *Lightwave Communications Technology Photodetectors*, vol. Volume 22, Part D, Elsevier, 1985, pp. 1–172.
[141] J. C. Campbell, A. G. Dentai, W. S. Holden, and B. L. Kasper, "High-performance avalanche photodiode with separate absorptiongrading?` and multiplication regions," *Electronics Letters*, vol. 19, no. 20, pp. 818–820, 1983.
[142] D. Renker, "Geiger-mode avalanche photodiodes, history, properties and problems," *Nuclear Instruments and Methods in Physics Research Section A: Accelerators, Spectrometers, Detectors and Associated Equipment*, vol. 567, no. 1, pp. 48–56, 2006.
[143] S. M. Sze and G. Gibbons, "Effect of junction curvature on breakdown voltage in semiconductors," *Solid-State Electronics*, vol. 9, no. 9, pp. 831–845, Sep. 1966.
[144] G. T. Boyd, T. Rasing, J. R. R. Leite, and Y. R. Shen, "Local-field enhancement on rough surfaces of metals, semimetals, and semiconductors with the use of optical second-harmonic generation," *Physical Review B*, vol. 30, no. 2, p. 519, 1984.
[145] M. Ghioni, A. Lacaita, G. Ripamonti, and S. Cova, "All-silicon avalanche photodiode sensitive at 1.3 mu;m with picosecond time resolution," *IEEE Journal of Quantum Electronics*, vol. 28, no. 12, pp. 2678 –2681, Dec. 1992.
[146] S. Cova, M. Ghioni, A. Lotito, I. Rech, and F. Zappa, "Evolution and prospects for single-photon avalanche diodes and quenching circuits," *Journal of Modern Optics*, vol. 51, no. 9–10, pp. 1267–1288, 2004.
[147] A. Lacaita, S. Cova, M. Ghioni, and F. Zappa, "Single-photon avalanche diode with ultrafast pulse response free from slow tails," *IEEE Electron Device Letters*, vol. 14, no. 7, pp. 360 –362, Jul. 1993.
[148] N. Susa, H. Nakagome, O. Mikami, H. Ando, and H. Kanbe, "New InGaAs/InP avalanche photodiode structure for the 1-1.6 #181;m wavelength region," *IEEE Journal of Quantum Electronics*, vol. 16, no. 8, pp. 864 – 870, Aug. 1980.
[149] R. Chen, T.-T. D. Tran, K. W. Ng, W. S. Ko, L. C. Chuang, F. G. Sedgwick, and C. Chang-Hasnain, "Nanolasers grown on silicon," *Nat Photon*, vol. 5, no. 3, pp. 170–175, Mar. 2011.
[150] J. T. Kostamovaara, A. Maentyniemi, P. J. M. Palojaervi, T. Peltola, T. Ruotsalainen, and E. Raeisaenen-Ruotsalainen, "Integrated chip set for a pulsed time-of-flight laser radar," pp. 33–47, May 2001.
[151] R. M. Schwarte, "Breakthrough in multichannel laser-radar technology providing thousands of high-sensitive lidar receivers on a chip," pp. 126–136, Nov. 2004.
[152] M. D. Kelzenberg, S. W. Boettcher, J. A. Petykiewicz, D. B. Turner-Evans, M. C. Putnam, E. L. Warren, J. M. Spurgeon, R. M. Briggs, N. S. Lewis, and H. A.

Atwater, “Enhanced absorption and carrier collection in Si wire arrays for photovoltaic applications,” *Nat Mater*, vol. 9, no. 3, pp. 239–244, Mar. 2010.
[153] B. Tian, X. Zheng, T. J. Kempa, Y. Fang, N. Yu, G. Yu, J. Huang, and C. M. Lieber, “Coaxial silicon nanowires as solar cells and nanoelectronic power sources,” *Nature*, vol. 449, no. 7164, pp. 885–889, Oct. 2007.
[154] Z. Fan, H. Razavi, J. Do, A. Moriwaki, O. Ergen, Y.-L. Chueh, P. W. Leu, J. C. Ho, T. Takahashi, L. A. Reichertz, S. Neale, K. Yu, M. Wu, J. W. Ager, and A. Javey, “Three-dimensional nanopillar-array photovoltaics on low-cost and flexible substrates,” *Nat Mater*, vol. 8, no. 8, pp. 648–653, 2009.
[155] T. J. Kempa, B. Tian, D. R. Kim, J. Hu, X. Zheng, and C. M. Lieber, “Single and Tandem Axial p-i-n Nanowire Photovoltaic Devices,” *Nano Lett.*, vol. 8, no. 10, pp. 3456–3460, Oct. 2008.
[156] W. U. Huynh, J. J. Dittmer, and A. P. Alivisatos, “Hybrid Nanorod-Polymer Solar Cells,” *Science*, vol. 295, no. 5564, pp. 2425–2427, Mar. 2002.
[157] M. A. Green, K. Emery, Y. Hishikawa, W. Warta, and E. D. Dunlop, “Solar cell efficiency tables (version 39),” *Progress in Photovoltaics: Research and Applications*, vol. 20, no. 1, pp. 12–20, 2012.
[158] W. Ma, C. Yang, X. Gong, K. Lee, and A. J. Heeger, “Thermally Stable, Efficient Polymer Solar Cells with Nanoscale Control of the Interpenetrating Network Morphology,” *Advanced Functional Materials*, vol. 15, no. 10, pp. 1617–1622, 2005.
[159] J. Wei, Y. Jia, Q. Shu, Z. Gu, K. Wang, D. Zhuang, G. Zhang, Z. Wang, J. Luo, A. Cao, and D. Wu, “Double-Walled Carbon Nanotube Solar Cells,” *Nano Lett.*, vol. 7, no. 8, pp. 2317–2321, Aug. 2007.
[160] C. Colombo, M. Heiβ, M. Grätzel, and A. Fontcuberta i Morral, “Gallium arsenide p-i-n radial structures for photovoltaic applications,” *Appl. Phys. Lett.*, vol. 94, no. 17, p. 173108, 2009.
[161] J. A. Czaban, D. A. Thompson, and R. R. LaPierre, “GaAs Core−Shell Nanowires for Photovoltaic Applications,” *Nano Letters*, vol. 9, no. 1, pp. 148–154, Jan. 2009.
[162] M. A. Green, “Limiting photovoltaic monochromatic light conversion efficiency,” *Progress in Photovoltaics: Research and Applications*, vol. 9, no. 4, pp. 257–261, 2001.
[163] J. P. Long, B. S. Simpkins, D. J. Rowenhorst, and P. E. Pehrsson, “Far-field Imaging of Optical Second-Harmonic Generation in Single GaN Nanowires,” *Nano Letters*, vol. 7, no. 3, pp. 831–836, Mar. 2007.
[164] J. C. Johnson, H. Yan, R. D. Schaller, P. B. Petersen, P. Yang, and R. J. Saykally, “Near-Field Imaging of Nonlinear Optical Mixing in Single Zinc Oxide Nanowires,” *Nano Letters*, vol. 2, no. 4, pp. 279–283, Apr. 2002.
[165] C. F. Zhang, Z. W. Dong, G. J. You, R. Y. Zhu, S. X. Qian, H. Deng, H. Cheng, and J. C. Wang, “Femtosecond pulse excited two-photon photoluminescence and second harmonic generation in ZnO nanowires,” *Appl. Phys. Lett.*, vol. 89, no. 4, pp. 042117–3, Jul. 2006.

[166] Y. Nakayama, P. J. Pauzauskie, A. Radenovic, R. M. Onorato, R. J. Saykally, J. Liphardt, and P. Yang, “Tunable nanowire nonlinear optical probe,” *Nature*, vol. 447, no. 7148, pp. 1098–1101, Jun. 2007.

[167] Y. Zhang, H. Zhou, S. W. Liu, Z. R. Tian, and M. Xiao, “Second-Harmonic Whispering-Gallery Modes in ZnO Nanotetrapod,” *Nano Letters*, vol. 9, no. 5, pp. 2109–2112, May 2009.

[168] D. Bethune, A. J. Schmidt, and Y. R. Shen, “Dispersion of nonlinear optical susceptibilities of InAs, InSb, and GaAs in the visible region,” *Phys. Rev. B*, vol. 11, no. 10, p. 3867, May 1975.

[169] S. Bergfeld and W. Daum, “Second-Harmonic Generation in GaAs: Experiment versus Theoretical Predictions of chi xyz(2),” *Phys. Rev. Lett.*, vol. 90, no. 3, p. 036801, Jan. 2003.

[170] T. Stehlin, M. Feller, P. Guyot-Sionnest, and Y. R. Shen, “Optical second-harmonic generation as a surface probe for noncentrosymmetric media,” *Optics Letters*, vol. 13, no. 5, p. 389, 1988.

[171] A. Saher Helmy, D. C. Hutchings, T. C. Kleckner, J. H. Marsh, A. C. Bryce, J. M. Arnold, C. R. Stanley, J. S. Aitchison, C. T. A. Brown, K. Moutzouris, and M. Ebrahimzadeh, “Quasi phase matching in GaAs--AlAs superlattice waveguides through bandgap tuning by use of quantum-well intermixing,” *Opt. Lett.*, vol. 25, no. 18, pp. 1370–1372, 2000.

[172] L. A. Eyres, P. J. Tourreau, T. J. Pinguet, C. B. Ebert, J. S. Harris, M. M. Fejer, L. Becouarn, B. Gerard, and E. Lallier, “All-epitaxial fabrication of thick, orientation-patterned GaAs films for nonlinear optical frequency conversion,” *Appl. Phys. Lett.*, vol. 79, no. 7, pp. 904–906, 2001.

[173] M. M. Fejer, G. A. Magel, D. H. Jundt, and R. L. Byer, “Quasi-phase-matched second harmonic generation: tuning and tolerances,” *Quantum Electronics, IEEE Journal of*, vol. 28, no. 11, pp. 2631–2654, 1992.

[174] W. Fan, S. Zhang, N. C. Panoiu, A. Abdenour, S. Krishna, R. M. . Osgood, K. J. Malloy, and S. R. J. Brueck, “Second harmonic generation from a nanopatterned isotropic nonlinear material,” *Nano Letters*, vol. 6, no. 5, pp. 1027–1030, 2006.

[175] C. K. Chen, A. R. B. de Castro, and Y. R. Shen, “Surface-Enhanced Second-Harmonic Generation,” *Phys. Rev. Lett.*, vol. 46, no. 2, p. 145, Jan. 1981.

[176] A. Penzkofer, M. Schäffner, and X. Bao, “Two-photon absorption and resonant non-phase-matched second-harmonic generation in CdSe,” *Optical and Quantum Electronics*, vol. 22, no. 4, pp. 351–367, Jul. 1990.

[177] I. Shoji, T. Kondo, A. Kitamoto, M. Shirane, and R. Ito, “Absolute scale of second-order nonlinear-optical coefficients,” *J. Opt. Soc. Am. B*, vol. 14, no. 9, pp. 2268–2294, 1997.

[178] N. Bloembergen and P. S. Pershan, “Light Waves at the Boundary of Nonlinear Media,” *Phys. Rev.*, vol. 128, no. 2, p. 606, Oct. 1962.

[179] M. Fleischmann, P. J. Hendra, and A. J. McQuillan, “Raman spectra of pyridine adsorbed at a silver electrode,” *Chemical Physics Letters*, vol. 26, no. 2, pp. 163–166, May 1974.

[180] M. G. Albrecht and J. A. Creighton, "Anomalously intense Raman spectra of pyridine at a silver electrode," *J. Am. Chem. Soc.*, vol. 99, no. 15, pp. 5215–5217, Jun. 1977.
[181] D. L. Jeanmaire and R. P. Van Duyne, "Surface raman spectroelectrochemistry: Part I. Heterocyclic, aromatic, and aliphatic amines adsorbed on the anodized silver electrode," *Journal of Electroanalytical Chemistry and Interfacial Electrochemistry*, vol. 84, no. 1, pp. 1–20, Nov. 1977.
[182] S. Nie, "Probing Single Molecules and Single Nanoparticles by Surface-Enhanced Raman Scattering," *Science*, vol. 275, no. 5303, pp. 1102–1106, Feb. 1997.
[183] M. Moskovits, "Surface-enhanced Raman spectroscopy: a brief retrospective," *J. Raman Spectrosc.*, vol. 36, no. 6–7, pp. 485–496, year></year> <year>2005</year 2005.